

Winter 2010

Calibration, optimization, and deployment of PTR-MS instruments during the AIRMAP project

Karl B. Haase

University of New Hampshire, Durham

Follow this and additional works at: <https://scholars.unh.edu/dissertation>

Recommended Citation

Haase, Karl B., "Calibration, optimization, and deployment of PTR-MS instruments during the AIRMAP project" (2010). *Doctoral Dissertations*. 548.

<https://scholars.unh.edu/dissertation/548>

This Dissertation is brought to you for free and open access by the Student Scholarship at University of New Hampshire Scholars' Repository. It has been accepted for inclusion in Doctoral Dissertations by an authorized administrator of University of New Hampshire Scholars' Repository. For more information, please contact nicole.hentz@unh.edu.

CALIBRATION, OPTIMIZATION, AND DEPLOYMENT OF PTR-MS
INSTRUMENTS DURING THE AIRMAP PROJECT

by

Karl B. Haase

Bachelor of Science in Chemistry, New Mexico Institute of Mining and Technology, 2005

DISSERTATION

Submitted to The University of New Hampshire

In Partial Fulfillment of

The Requirements for the Degree of

Doctor of Philosophy

in

Chemistry

December, 2010

UMI Number: 3442543

All rights reserved

INFORMATION TO ALL USERS

The quality of this reproduction is dependent upon the quality of the copy submitted.

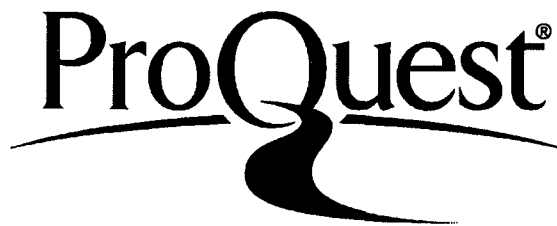
In the unlikely event that the author did not send a complete manuscript and there are missing pages, these will be noted. Also, if material had to be removed, a note will indicate the deletion.



UMI 3442543

Copyright 2011 by ProQuest LLC.

All rights reserved. This edition of the work is protected against unauthorized copying under Title 17, United States Code.



ProQuest LLC
789 East Eisenhower Parkway
P.O. Box 1346
Ann Arbor, MI 48106-1346

ALL RIGHTS RESERVED

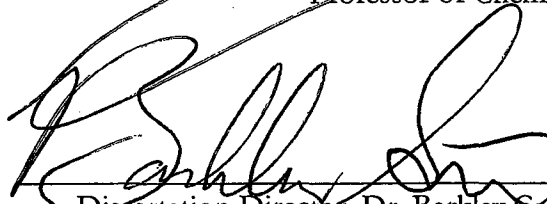
© 2010

Karl B. Haase

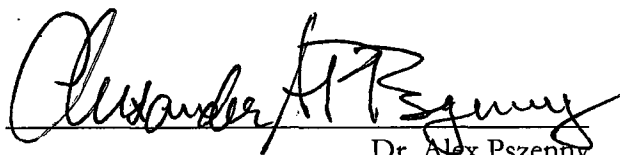
This dissertation has been examined and approved.



Dissertation Director, Dr. Howard R. Mayne
Professor of Chemistry



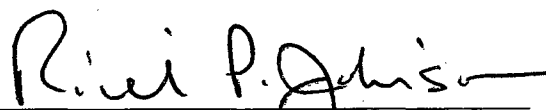
Dissertation Director, Dr. Barkley C. Sive
Research Associate Professor of Earth, Oceans, and Space



Dr. Alex Pszeny
Research Associate Professor of Earth, Oceans, and Space



Dr. Arthur Greenberg
Professor of Chemistry



Dr. Richard P. Johnson
Professor of Chemistry

9/3/2010

Date

ACKNOWLEDGEMENTS

I would like to extend the most sincere thanks to Dr. Barkley Sive and Dr. Howard Mayne for their guidance and advice throughout my time at UNH. I have learned a great deal under their tutelage. I also wish to thank the members of my committee for their patience, instruction, and time spent helping me as I have moved through graduate school. I would like to thank Dr. Robert Talbot for allowing me to work with the AIRMAP project and the PTR-MS instruments. I am grateful for the generous financial support of the UNH chemistry department, the NSF, and the NOAA funded AIRMAP project.

I would like to thank Kevan Carpenter, Cheryl Parker, Peter Kelly, Pieter Beckman, Laura Cottrell, Karen Garrison, Todd Hegan, Eric Fitz, Sean Wadsworth, Don Troop, Dr. Carolyn Jordan, and Dr. Huiting Mao for their work in the AIRMAP project that has made my research possible. I would like to thank Dr. Alex Pszenny and Dr. Bill Keene (University of Virginia) for access their gas phase acetic acid data. The assistance and camaraderie in the lab and field from the other members of the VOC research group has been essential. I would like thank Dr. Rachel Russo, Dr. Jesse Ambrose, Dr. Yong Zhou, Dr. Marguerite White, Dr. Elizabeth Mentis, Leanna Butland, Bob Swarthout, L. Carsten Nielson, Andrew Young, Andrew Hart, and many, many others. Thank you, Cindi Rohwer, and Thank you, Peg Torch, for telling me what is happening and when.

Thanks to Mom and Dad for their multifaceted support since the beginning.

And thanks to Aimee, for being there, for being patient, and for putting up with me.

TABLE OF CONTENTS

ACKNOWLEDGEMENTS	IV
LIST OF TABLES.....	VIII
LIST OF FIGURES	X
ABSTRACT	XV
INTRODUCTION	1
CHAPTER 2 A STUDY OF ENHANCED DRIFT TUBE WATER PRESSURE ON PTR-MS PERFORMANCE: ION SOURCE OPTIMIZATION, SENSITIVITY, AND CLUSTER FORMATION.....	5
2.1 Introduction:.....	5
2.2 Background:.....	6
2.3 Experimental:	8
2.4 Results:	11
2.4.1 Ion Source Performance and Hydrated Cluster Distributions.....	11
2.4.2 Skimmer pumping capacity and drift tube water pressure.....	13
2.4.3 Sensitivity and Fragmentation Study	17
2.5 Conclusions	24
2.6 Figures and Tables.....	26
CHAPTER 3 MODELING CLUSTER DISTRIBUTIONS IN THE PTR-MS DRIFT TUBE AND IMPLICATIONS FOR THE KINETICS OF CLUSTER REACTIONS	45
3.1 Introduction.....	45
3.2 Background:.....	46

3.3 Development of a Kinetics Model.....	49
3.4 Model Testing.....	55
3.4.1 Comparison of the Kinetics and Equilibrium Models	56
3.5 Comparison of PTR-MS and Model Cluster Distributions.....	57
3.6 Comparison of Predicted and Measured Instrument Response.....	60
3.6.1 Benzene and Toluene	61
3.6.2 Isoprene and Acetone	62
3.7 Conclusions	63
3.8 Figures and Tables.....	65
CHAPTER 4 CALIBRATION, VALIDATION, AND MEASUREMENTS OF ACETIC ACID USING PTR-MS ON APPLIEDORE ISLAND DURING ICARTT.....	82
4.1 Introduction.....	82
4.2 Experimental:	85
4.3 Results:	90
4.3.1 Standard Sensitivity Calibrations with PTR-MS-1 (SS).....	90
4.3.2 Calibration of a High Sensitivity PTR-MS [PTR-MS-2 (HS)]	93
4.3.3 PTR-MS-1 (HS) Calibration and E/N dependence	94
4.3.4 Clusters and Fragmentation: E/N Ratios and Humidity	95
4.4 Measurements of Acetic Acid on Appledore Island during ICARTT 2004.....	97
4.4.1 Overview	97
4.4.2 Comparison with MC/IC Measurements.....	99
4.4.3 Analysis of Acetic Acid Measurements on Appledore Island during the ICARTT Campaign.....	101

4.5 Improving PTR–MS Measurements of Acetic Acid: Current Progress and Future Directions.....	108
4.6 Conclusions	111
4.7 Acknowledgements	112
4.8 Figures and Tables.....	113
 CHAPTER 5 : STORM IMPACTS ON MONOTERPENE MIXING RATIOS	
OBSERVED AT A RURAL SITE IN NEW HAMPSHIRE	139
5.1 Introduction.....	139
5.2 Experimental	140
5.2.1 Measurements at Thompson Farm	140
5.2.2 Determination of Storm Events	142
5.3 Analysis.....	144
5.3.1 Environmental Conditions Associated with Events.....	149
5.4 Discussion.....	155
5.5 Conclusions	156
5.6 Figures and Tables.....	158
REFERENCES.....	172

LIST OF TABLES

Table 2-1. Mixing ratios of the compounds used to test the sensitivity of the instrument over a range of drift tube conditions.	26
Table 2-2. The valve setting, equivalent tube length, water flow, calculated skimmer pumping speed, and calculated skimmer tube conductance values.	27
Table 2-3. The change in response factor when H_3O^+ is the dominant ion and when $\text{H}_3\text{O}^+(\text{H}_2\text{O})$ is the dominant species.	28
Table 3-1. The values from Lau et al. ³¹ for the thermodynamics and forward kinetics of the $\text{H}_3\text{O}^+(\text{H}_2\text{O})_{n-1} + \text{H}_2\text{O} + \text{M} \leftrightarrow \text{H}_3\text{O}^+(\text{H}_2\text{O})_n + \text{M}$ system.	65
Table 3-2. Test conditions to compare the kinetics and equilibrium models and measurement made using the PTR-MS.	67
Table 4-1. A summary of acetic acid calibrations reported in the literature, and in this study.	113
Table 4-2. Cluster and fragment distribution data obtained over a range of E/N values with PTR-MS-1 (HS).	114
Table 4-3. The average and standard deviation of the signal for protonated clusters in the primary ion signal in the different PTR-MS configurations used in this study.	115
Table 5-1. Locations and approximate times of the unique storm events in Strafford and Rockingham Counties in southern New Hampshire obtained from the NWS Event Database.	158
Table 5-2. Storm events at Thompson Farm, identified by using radar.	159

Table 5-3. Summary of storm event days, events identified by radar, and measured events
(Type A, B, or C) examined in the study. 160

Table 5-4. Summary of estimated storm induced monoterpene emissions at Thompson
Farm. 161

LIST OF FIGURES

Figure 2-1. Diagram of the PTR-MS Instrument	29
Figure 2-2. H_3O^+ signal as a function of valve position and ion source water flow settings.	30
Figure 2-3. The ratio of H_3O^+ to $\text{H}_3\text{O}^+(\text{H}_2\text{O})$ as a function of meter valve position and ion source water flow, with overlaid results from 40 cm and 32 cm skimmer tubes.	31
Figure 2-4. The total primary ion signal (the sum of all protonated water clusters) as a function of meter valve position and ion source water flow.	32
Figure 2-5. Pressure controller settings at various water flow and drift tube skimmer conditions, with overlaid results from 40 cm and 32 cm skimmer tubes.	33
Figure 2-6. U3 voltage settings required to minimize O_2^+ to less than 1% of the $\Sigma\text{H}_3\text{O}^+(\text{H}_2\text{O})_n$.	34
Figure 2-7. The composition and intensity of different $\text{H}_3\text{O}^+(\text{H}_2\text{O})_n$ clusters in the drift tube as the partial pressure of water increases.	35
Figure 2-8. The proton affinity of the first three $\text{H}_3\text{O}^+(\text{H}_2\text{O})_n$ clusters and the compounds for which the sensitivity was measured.	36
Figure 2-9. Graphs of H_3O^+ and protonated water clusters, total ion signal (m19+m37+m55) and the ratio of intensities, and ion source byproducts.	37
Figure 2-10. Response factors for acetone, isoprene, benzene, toluene, and camphene.	38
Figure 2-11. The cluster normalized response factor of benzene.	39
Figure 2-12. The cluster normalized response factor of toluene.	40
Figure 2-13. The cluster normalized response factor of Isoprene.	41
Figure 2-14. The cluster normalized response of Acetone.	42

Figure 2-15. The cluster normalized response of camphene.	43
Figure 2-16. The ratio of m81/m137 as a function of skimmer flow and ion source water flow.	44
Figure 3-1. Comparison of the equilibrium model and PTR-MS measurements.	67
Figure 3-2. The reaction pathways simulated by the kinetics model.	68
Figure 3-3. The relative transmission efficiency as a function of an ions mass-to-charge ratio within a PTR-MS instrument	69
Figure 3-4. The average time it takes for an ensemble of protonated water clusters to traverse a 10 cm drift tube.	70
Figure 3-5. Kinetics model results for different drift tube humidities.	71
Figure 3-6. Kinetics and equilibrium models of cluster distributions at different water pressures in the drift tube.	72
Figure 3-7. The results of model sensitivity study to illustrate the effect of the uncertainty of the kinetic constants.	73
Figure 3-8. A comparison between humidity dependent cluster distributions measured in the PTR-MS and cluster distributions predicted by the kinetics and equilibrium models.	74
Figure 3-9 (a-b). The effect of reducing the estimated T_{eff} in the kinetics model.	75
Figure 3-10 (a-e). Examples of various outcomes of kinetics model sensitivity testing.	76
Figure 3-11. Improved match between the kinetics model and measurements caused by increasing the rate of $H_3O^+(H_2O)_2$ formation from the reaction of $H_3O^+(H_2O)$ and H_2O by a factor of 200.	77
Figure 3-12. The three rate constants for cluster formation as a function of water pressure, along with k_{g2} increased by the factor of 200 to fit to the measured cluster distributions.	78

Figure 3-13. Kinetics model results, equilibrium model results, and measurements at different drift tube E/N ratios.	79
Figure 3-14. Modified kinetics model results superimposed on equilibrium model results and measurements.	80
Figure 3-15. The relative response of benzene, toluene, isoprene, and acetone as the fraction of clusters in the total primary ion signal increases.	81
Figure 4-1. The flow of gases through the permeation oven used to calibrate the PTR-MS for measuring acetic acid.	116
Figure 4-2. Estimated mixing ratios of acetic acid generated from a $103 \text{ ng}\cdot\text{min}^{-1}$ permeation tube, and a $100 \text{ cm}^3\cdot\text{min}^{-1}$ permeation flow.	117
Figure 4-3. A typical calibration curve for acetic acid, measured with PTR-MS-1 (SS), and a calibration curve for acetic acid measured using PTR-MS-2 (HS).	118
Figure 4-4. Rise times (in minutes) measured with PTR-MS-1 (SS).	119
Figure 4-5. PTR-MS-1 (HS) calibration factors for acetic acid over a range of E/N ratios.	120
Figure 4-6. Increase in the ratio of acetic acid fragments relative to protonated acetic acid, as $\text{H}_3\text{O}^+(\text{H}_2\text{O})$ (m/z 37) becomes more dominant in the primary ion signal.	121
Figure 4-7. Several protonation and fragmentation pathways of acetic acid.	122
Figure 4-8. Acetic Acid measurements made by PTR-MS 2 (HS) during ICARTT.	123
Figure 4-9. PTR-MS and MC/IC data for periods where both techniques were operational.	124
Figure 4-10. A scatter plot of the PTR-MS and MC/IC measurements of acetic acid on Appledore Island during the ICARTT campaign.	125

Figure 4–11. Time series data of acetic acid, and CO, ozone on Appledore Island, and wind speed, wind direction, and temperature measured on Isle of Shoals at the IOSN3 Station.	126
Figure 4–12. Acetic acid mixing ratios binned by wind direction.	127
Figure 4–13. Acetic acid mixing ratios binned by windspeed.	128
Figure 4–14. Scatter plots of acetic acid and wind speed, binned by source direction.	129
Figure 4–15. Acetic acid, wind direction wind speed, and temperature at Appledore Island binned by the time of day	130
Figure 4–16. Acetic Acid mixing ratios for each day of the campaign, plotted by hour.	131
Figure 4–17. The difference between the daytime average mixing ratio and the late night average mixing ratio of acetic acid.	132
Figure 4–18. An orthogonal least squares linear regression to determine enhancement ratio of acetic acid to CO at Appledore Island during ICARTT 2004.	133
Figure 4–19. Measured acetic acid mixing ratio, compared with those predicted by the linear regression of the CO and acetic acid data set in Figure 4–18.	134
Figure 4–20. An orthogonal least squares linear regression on the enhancement of acetic acid to the enhancement of ozone measured on Appledore Island during ICARTT.	135
Figure 4–21. Measured signal at m/z 61 and measured background during the ICARTT campaign.	136
Figure 4–22. Measured ambient signal at m/z 61 and background signal from our current configuration.	137
Figure 4–23. A detail view of the measurement (blue), and air sampled through the catalytic converter (black) sampled (black), and background measurements determined from the background signal (green).	138

Figure 5-1. Cities and towns in the area surrounding Thompson Farm	162
Figure 5-2. An example of a Type A event, from August 22, 2009 (UTC). Blue lines indicate the period of precipitation, while red lines indicate peak precipitation.	163
Figure 5-3. An example Type B event, where the mixing ratios of monoterpenes peak for a brief period of time, from May 11, 2007.	164
Figure 5-4. An example of a Type C event, where the storm passage coincides with a drop in monoterpene mixing ratios from July 23, 2005.	165
Figure 5-5. An example of a Type D event, where the storm passage had little impact on mixing ratios, from June 24, 2008.	166
Figure 5-6. The average mixing ratio of monoterpenes as storm systems pass over Thompson Farm.	167
Figure 5-7. The average, median, minimum, and maximum change in monoterpene mixing ratios for each type of storm event.	168
Figure 5-8. Average wind speed for each type of storm event.	169
Figure 5-9. Average temperature for each storm type.	170
Figure 5-10. Average peak precipitation rate over Thompson Farm for each event type.	171

ABSTRACT

CALIBRATION, OPTIMIZATION, AND DEPLOYMENT OF PTR-MS INSTRUMENTS DURING THE AIRMAP PROJECT

by

Karl B. Haase

The University of New Hampshire, December, 2010

Proton Transfer Reaction Mass Spectrometry (PTR-MS) is an increasingly popular technique for monitoring volatile organic compounds with high sensitivity and time resolution. This dissertation encompasses three different projects, sharing the common theme of expanding the knowledge and utility of the technique.

The first project focuses on elucidating the ion chemistry that occurs within the PTR-MS drift tube reaction chamber. The PTR-MS uses a differentially pumped skimmer to prevent excess water from the ion source from entering the drift tube reaction chamber. By placing a metering valve in between the skimmer region and the pump, it was possible to control the amount of water entering the drift tube. The valve made it possible to parameterize the impact of the pumping speed of the skimmer on ion source performance, cluster formation, and sensitivity. These results are compared with a kinetics model that simulates the protonated cluster distributions in the drift tube.

The second part of this dissertation describes the process for calibrating and deploying the instrument to measure acetic acid. Generating calibrations and measurements of ambient levels acetic acid are challenging because it adsorbs on instrument surfaces and transfer lines. To overcome the challenge of calibrating, a special permeation oven was used

to generate a stable flow of acetic acid in the range of 7.0 to 26.5 ppbv, yielding calibration factors of 7.0 ± 0.3 ncps·ppbv⁻¹ to 10.9 ± 0.7 ncps·ppbv⁻¹ at 132 Td. At 88 Td, the calibration factor was found to be 30.8 ± 2.6 ncps·ppbv⁻¹. Measurements made on Appledore Island during ICARTT show that the PTR-MS measurements correlate well with those from the MC/IC technique, with a correlation coefficient of 0.78.

The final project uses the high time resolution of PTR-MS measurements to quantify the impact of storm systems on monoterpene mixing ratios in rural New Hampshire. Analysis of five years of monoterpene measurements at Thompson Farm (in Durham, NH) show storm events with intense precipitation correlate with brief periods of enhanced monoterpene mixing ratios. These events are classified based on duration and intensity, finding that storms can temporarily increase emissions by as much as $4260 \text{ g}\cdot\text{km}^{-2}\cdot\text{hr}^{-1}$.

INTRODUCTION

Proton Transfer Reaction Mass Spectrometry, or PTR-MS, is a positive chemical ionization mass spectrometry technique that has become a favored method for real time monitoring of trace volatile organic compounds (VOCs) in the atmosphere.¹⁻⁴ The PTR-MS technique was originally developed by Dr. Werner Lindinger's group at the Institute for Ion Physics at the University of Innsbruck in Austria.⁵ The underpinnings of the technique have roots that reach into ion chemistry experiments done in the 1960s and 1970s: Flow tube techniques ultimately became the basis of the PTR-MS drift tube reaction chamber.⁶ At the same time, plasma physics experiments led to the development of the hollow cathode discharge that is the source of the intense primary ion current.⁷⁻⁹ The technique's growth has been unquestionably accelerated through its commercialization by Ionicon Analytic, which has made PTR-MS instrumentation accessible to many who would not necessarily have the resources to build a mass spectrometer themselves, thereby creating a common base where measurement techniques and observations can be shared. In addition to those instruments produced by Ionicon, similar instruments have been commercially developed by Kore Technology,¹⁰ and numerous groups have developed their own instruments, coupling different ion sources and detectors to drift tube reactors, deriving a wide range of detection and analysis routes from the proton transfer reaction.¹¹⁻¹⁹ The high time resolution of PTR-MS instruments has shown them to be invaluable tools for measuring VOCs, and they have quickly proven valuable in many aspects of atmospheric chemistry including airborne

measurements, aerosol chamber studies, eddy covariance flux measurements, ship based and mobile labs, and long term *in situ* observations.²⁰⁻²⁶

The goal of this dissertation is to expand the knowledge about the PTR-MS technique and its applications in three directions:

1. Enhance the understanding of the ion molecule chemistry within the PTR-MS drift tube.
2. Demonstrate calibrations and measurements of ambient acetic acid using PTR-MS.
3. Determine the influence of storm events on biogenic emissions by employing the high time resolution PTR-MS measurements of ambient monoterpene mixing ratios at Thompson Farm, an AIRMAP field site in Durham, NH.

Chapter 2 examines the formation of $\text{H}_3\text{O}^+(\text{H}_2\text{O})_n$ clusters from water vapor entering the PTR-MS drift tube from the ion source, along with the resulting change in instrumental response to different compounds. Understanding the ion molecule reactions that occur in the drift tube is critical for reducing fragmentation, optimizing sensitivity, and increasing the certainty that the signal at a specific mass-to-charge ratio is characteristic of a given compound. The formation of hydrated clusters reduces sensitivity and convolutes the mass spectrum, making data analysis more difficult and increasing uncertainty in measurements. Fragmentation of ionized molecules is also dependent on the protonating cluster and on the electric field strength within the drift tube.²⁷⁻³⁰

In chapter 3, those results are compared to the output of a kinetics model developed explicitly to simulate the ion molecule chemistry in the drift tube. This model is a departure from an equilibrium based technique that had been used in several other studies.^{3, 31, 32} It supplies a dynamic view of changing cluster distributions along the length of the PTR-MS

drift tube. The difference between the kinetics model output and measured protonated cluster distribution suggests that current understanding of the rate constants governing the formation and destruction of protonated clusters within the drift tube is incomplete.

Chapter 4 focuses on measurement and calibration of ambient acetic acid using the PTR-MS. Acetic acid is ubiquitously present in the ambient atmosphere, with mixing ratios reaching into the low tens of ppbv, and is the most abundant gas phase organic acid in the troposphere.^{33, 34} However, the magnitude of the sources and sinks of acetic acid in the environment are not well understood, as they are widely dispersed and measurements are relatively challenging to make.^{34, 35} In this work, calibrations of two PTR-MS instruments for acetic acid mixing ratios in the low ppbv are reported. Measurements of acetic acid collected during the ICARTT campaign at Appledore Island are validated against MC/IC measurements showing good correlation. The high frequency data produced by the PTR-MS is used to examine the diurnal trends and controls on the acetic acid mixing ratios observed at Appledore Island.

In chapter 5, the impact of intense rain storms on monoterpene mixing ratios is examined. Monoterpenes are an important class of biogenic compounds that influence ambient air quality and are an important source of secondary organic aerosol. They are emitted from vegetation as a product of photosynthesis and as a response to a variety of environmental factors. Most parameterizations of monoterpene emissions are based on clear weather models, and do not take into account episodic factors that can drastically change production.³⁶⁻³⁹ In this chapter, the ongoing PTR-MS based monoterpene dataset from Thompson Farm is examined in the context of a set of known severe storm events. The analysis shows that storms coincide with large, episodic increases in monoterpene mixing ratios, implying enhanced emissions. Considering the regularity of storm events over most

forested areas, this could be an important factor to consider when modeling global monoterpene emissions and the resulting formation of organic aerosols.^{40, 41} This point is especially important when considered in context of predicted increasing severe storm frequency due to global scale meteorological change.^{42, 43}

CHAPTER 2

A STUDY OF ENHANCED DRIFT TUBE WATER PRESSURE ON PTR-MS PERFORMANCE: ION SOURCE OPTIMIZATION, SENSITIVITY, AND CLUSTER FORMATION

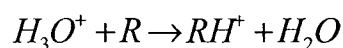
2.1 Introduction:

Proton Transfer Reaction-Mass Spectrometry (PTR-MS) is a real time, positive chemical ionization technique for monitoring gas phase organic compounds. The PTR-MS uses H_3O^+ to ionize the target compounds through proton transfer reactions. In the commercial PTR-MS made by Ionicon Analytic, a hollow cathode discharge ion source is used to convert ultra pure water vapor into H_3O^+ , which is then used to protonate target analyte molecules in a drift tube reaction chamber. The hollow cathode ion source is separated from the drift tube by a differentially pumped region to minimize the amount of water entering the drift tube from the ion source. The flow rate of gases exiting this region is determined by a length of tubing between the skimmer region and the turbo pump at the interface between the drift tube reaction chamber and the mass spectrometer. There has been limited discussion in the literature about how the gas flow through this skimmer impacts the performance of the ion source. In this chapter the impact of the gas flow through this region on production of H_3O^+ , O_2^+ , and NO^+ by the ion source and resulting water cluster formation in the drift tube is examined. The sensitivity of the PTR-MS towards

several compounds was determined under a range of ion source water and skimmer region flow rates in order to quantify the impact of flow rate through the skimmer region on instrument performance. In order to accomplish these goals, the tube between the ion source skimmer region and the turbo pump was replaced with a meter valve, which allowed the flow rate of gases through the skimmer to be precisely controlled without powering down the PTR-MS.

2.2 Background:

The general operation of the PTR-MS instrument has been discussed extensively elsewhere,³⁻⁵ and will only be briefly reviewed here. Within the PTR-MS, H_3O^+ ions are generated by flowing water vapor through a hollow cathode discharge ion source. A small stream of sample gas is introduced at the top of a drift tube where the ions can react collisionally ($k \approx 1 \times 10^{-9} \text{ molec} \cdot \text{cm}^{-3} \cdot \text{s}^{-1}$) with any molecule (R) in the sample gas stream that has a proton affinity greater than water ($>692 \text{ kJ} \cdot \text{mol}^{-1}$) in a proton transfer reaction:



The proton transfer reaction is endothermic for the major components of ambient air, including nitrogen, oxygen, argon, CO_2 , and light alkanes; however the reaction is exothermic for most alkenes, oxygenated compounds, and sulfur containing species. The exothermicity of this reaction is generally low (a few tens of $\text{kJ} \cdot \text{mol}^{-1}$) yielding a limited amount of fragmentation compared to electron impact ionization. The selectivity of the proton transfer reaction, combined with the high time resolution of mass spectrometry, makes PTR-MS a useful tool for many real time measurement applications.

A detailed diagram of the PTR-MS is shown in Figure 2-1, depicting the different regions within the instrument, the pumping systems, the ion optics, and power supplies used

control the ion optics. The skimmer region is located between the ion source and the drift tube. This region performs three critical functions to the PTR-MS: i) it allows ions from the ion source to react to form H_3O^+ , ii) it draws excess water away from the drift tube, and iii) prevents air from the drift tube from entering the ion source. H_2O^+ , O^+ , H^+ , H_2^+ , and OH^+ ions are formed inside the hollow cathode through electron ionization and charge transfer processes.⁵ When these ions enter the skimmer region, they react with excess water emitted from the ion source to form H_3O^+ . If extraneous air enters the skimmer region and the ion source, oxygen can be ionized to form O_2^+ through charge transfer from H_2O^+ . Both NO^+ and O_2^+ can also be formed directly by electron ionization inside of the discharge.⁴⁴

The skimmer region is connected to a turbo pump by a length of 0.64 cm (0.25") OD Teflon tubing, the length of which controls the flow rate of gases through the skimmer.⁴⁵ Wisthaler et al.⁴⁶ increased the sensitivity to some compounds using an instrument with a shortened skimmer tube, which decreased the amount of water vapor entering the drift tube from the ion source. The sensitivity to compounds with a proton affinity close to that of water decreases when excess water vapor is present in the drift tube, as it increases the rate of competitive reverse proton transfer reactions from the protonated analyte to the neutral water molecules. Excess water entering the drift tube also causes formation of hydrated proton clusters $[\text{H}_3\text{O}^+(\text{H}_2\text{O})_n]$ resulting in a reduction of sensitivity to compounds like benzene and toluene, as their proton affinity is low enough that proton transfer from clusters is disfavored.⁴⁷

The purpose of this work is to explore the impact of gas flow through the skimmer tube on instrument performance. The Experimental section describes the modification carried out on the PTR-MS and the procedure used to characterize the impact of skimmer flow on PTR-MS performance. In the Results section, the influence of varying the skimmer

flow rate on formation of hydrated clusters in the drift tube is examined. A method to determine the amount of water transferred to the drift tube from the ion source is presented. Finally, response measurements at varying drift tube water vapor pressures for acetone, isoprene, benzene, toluene, and camphene are examined.

2.3 Experimental:

Our group operates several PTR-MS instruments obtained from Ionicon Analytic GmbH (Austria). The PTR-MS instruments consist of several different functional regions separated by pinholes that allow ions to pass through these different regions towards the quadrupole mass spectrometer (Figure 2-1). The ion source (A), skimmer (B), and drift tube (C) all operate at pressures in the range of a few millibar, governed by the constant pressure in the drift tube. The intermediate vacuum region (D) serves to interface the drift tube to the mass spectrometer. The skimmer region (B) is connected to the intermediate vacuum region by a length of PFA Teflon tubing (F). The skimmer region serves several roles: to isolate the drift tube and ion source, and to act as a region where ions from the ion source can react to form H_3O^+ . Our group originally had one standard sensitivity and one high sensitivity PTR-MS instruments. In 2007, the standard sensitivity instrument was upgraded to a high sensitivity model. Based on Wisthaler et al.⁴⁶, the pumping system of the upgraded instrument was modified by shortening the skimmer tube [Figure 2-1 (F)] between the intermediate vacuum region (D) and the ion source (IS) (B). This change required re-routing the wiring to the drift tube and rotating the skimmer and IS 120 degrees relative to the drift tube, so that the skimmer inlet was collinear with the inlet to the intermediate vacuum region. The elbow fitting supporting the turbo pump connected to the intermediate vacuum region was rotated 180 degrees to point the tube interface upwards toward the skimmer.

This allowed for a 10cm long, 0.62 cm OD PFA Teflon tube to be installed, in contrast to the original tube length of 32 cm. The total length of the new flow path was 15 cm, accounting for fittings and other hardware.

Prior to upgrading the standard sensitivity instrument, high primary ion (H_3O^+) count rates were achievable (6.0-10 MHz), but after the upgrade and changes to the vacuum system, ion count rates were typically in the range of 0.5 to 2.0 MHz. High H_3O^+ generation is very important to achieve ultimate analytical sensitivity, so this condition was undesirable. A 40cm long skimmer tube was then installed in place of the 10cm long tube in an attempt to improve IS performance. This test yielded higher H_3O^+ count rates (~ 5.0 MHz). These results indicate that the gas flow through the skimmer tube strongly impacts performance of the PTR-MS.

In order to control the flow of gases through the skimmer region, a high flow metering valve [Swagelok SS-4L-MH, Figure 2-1(G)] was installed between the skimmer (B) and the intermediate vacuum region of the instrument (D). This valve allows the flow from the skimmer to be quantitatively controlled (via a vernier scale on the valve handle). Using this valve, several tests were completed to quantify the relationship between skimmer flow, water flow and instrument performance. Throughout these experiments, the hollow cathode ion source power supply was set to 600 V with a discharge current of 8mA. The 10 cm drift tube was held at a field strength of 132 Td ($1 \text{ Td} = 10^{-17} \text{ V} \cdot \text{cm}^2 \text{ molec}^{-1}$) with corresponding drift tube conditions of 600V, 2.0 mbar, 313.0K. The upper extraction voltage, U_{1+2} , (Figure 2-1), was set at 400V for all measurements, while the lower extraction voltage U_3 was set to keep the ratio of O_2^+ to H_3O^+ less than 1%. During each test sequence, the metering valve was iteratively opened by $\frac{1}{4}$ turn increments between valve settings of 0.75 to 2.75 (fully open position). Each increase in valve position resulted in an increase in gas flow through

the skimmer tube. At each valve setting, the water flow through the ion source was stepwise increased in increments of $1.0 \text{ cm}^3 \cdot \text{min}^{-1}$ (determined at STP). At each combination of valve and water flow, the bypass pressure was set to bring the drift tube to 2.0 mbar, then U3, the lower extraction voltage (Figure 2-1), was optimized so that O_2^+ was $\leq 1\%$ of H_3O^+ , in order to ensure that H_3O^+ was the dominant reagent ion. Before moving on to the next ion source water flow setting, U_{1+2} and U_3 were reduced to $<290\text{V}$ and $<90\text{V}$ respectively to prevent discharges from forming in the skimmer region while the water flow and drift tube pressure were set. Measurements were made for each valve setting where O_2^+ could be sustained below 1% of the total primary ion signal, and stopped when secondary discharges formed within the skimmer region itself. These were judged to occur by large increases in the abundance of $\text{H}_3\text{O}^+(\text{H}_2\text{O})_n$ and O_2^+ ions, and the power supplies for the extraction lens indicating a closed loop condition as a result of the flow of electrons through the secondary discharge. After the test sequence with the metering valve, the IS performance was tested with 20, 32, and 40 cm skimmer tubes installed to provide a reference to compare the results obtained with the metering valve to the way the PTR-MS instruments are typically configured.

The ions formed by the ion source and by reactions occurring in the drift tube were monitored using the PTR-MS quadrupole mass spectrometer. In order to preserve the electron multiplier, H_3O^+ (m/z of 19, referred to hereafter as m19) was measured by monitoring the $\text{H}_3^{18}\text{O}^+$ isotopologue (m21) and scaling it by a factor of 500 to account for the ratio of natural abundance compared to ^{16}O . O_2^+ (m32), $\text{H}_3\text{O}^+(\text{H}_2\text{O})$ (m37), and $\text{H}_3\text{O}^+(\text{H}_2\text{O})_2$ (m55) were recorded for at least 10 cycles at unit mass resolution. Subsequent studies using the metering valve were repeated while measuring m30 (to monitor NO^+ production), as well as m59, m69, m79, m93, m81, and m137 in single ion measurement

(SIM) mode with a 1 second integration time to quantify the sensitivity of the instrument to acetone, isoprene, benzene, toluene, and camphene, respectively. The monoterpene camphene has a major fragment ion at m/z 81,^{30, 48} which was monitored as a metric of how changes to the flow through the skimmer affected fragmentation. Sample gas from a synthetic standard calibration cylinder (Maine Oxy) containing high ppbv levels of the target compounds was used. The standard gas flow was controlled by a mass flow controller (MKS Instruments), diluted to low ppbv levels by mixing into a stream of purified air flowing at 1.1 L·min⁻¹. The compounds measured and the calculated mixing ratios generated by the dilution system are listed in Table 2-1. The purified air was generated by passing ambient air through a heated 0.5% Pd-on-alumina bead catalyst at 600°C. Alternating sets of background and calibration gas measurements were made at each skimmer valve and water flow combination.

2.4 Results:

2.4.1 Ion Source Performance and Hydrated Cluster Distributions

Figure 2-2 shows H₃O⁺ generation at every water and skimmer flow set point. The range of highest (>2.0 MHz) H₃O⁺ count rates increase as the flow through the skimmer increases. At a valve position of 0.75, the H₃O⁺ signal exceeds 4.0 MHz for a single combination when the water flow was at 7.0 cm³·min⁻¹. At a meter valve setting of 2.00 this range extended from 10.0 to 13.0 cm³·min⁻¹, and was attributable to the increased pumping capacity of the skimmer. At large valve positions, when the valve was almost completely open, relatively large changes in the water flow rate through the ion source were required to significantly change the amounts of water and air in the skimmer region. At low skimmer

flows, the opposite is true; small changes in the amount of water coming from the ion source can make the difference between being predominantly water vapor or predominantly air.

Every valve setting had at least one flow combination that resulted in high H_3O^+ (>1.0 MHz) count rates. Larger skimmer flow rates required corresponding increases in water flows to achieve favorable primary ion generation efficiencies.

It in addition to H_3O^+ , is also important to consider the impact of skimmer and water flows on the formation of water clusters in the drift tube. Understanding cluster formation is important because clusters undergo proton transfer reactions that are less exothermic than reactions with hydronium ions.⁴⁹ It is usually desirable for cluster formation to be suppressed as much as possible to simplify data analysis and optimize sensitivity. Figure 2-3 shows the ratio of $\text{H}_3\text{O}^+(\text{H}_2\text{O})$ cluster counts (m37) to H_3O^+ signal and Figure 2-4 shows the total ion signal for the first three water clusters. If no water enters the drift tube from the ion source, cluster formation is governed by water entering the drift tube as ambient humidity comprises part of the sample stream. This experiment reinforces the idea that the water content in ambient air will ultimately control cluster abundance in the drift tube, regardless of the efficiency of the skimmer tube region in removing water introduced in the ion source. At 132 Td, $\text{H}_3\text{O}^+(\text{H}_2\text{O})$ was approximately 2%, and $\text{H}_3\text{O}^+(\text{H}_2\text{O})_2$ was approximately $2 \times 10^{-3}\%$ of the H_3O^+ signal due to ambient humidity.

Cluster formation (detected at m37 and m55) occurred as excess water entered the drift tube because the pumping capacity of the skimmer was saturated by the water vapor flow from the IS. The increase in water clusters and the change in the relative abundance of each cluster was similar to that observed when the field strength of the drift tube was decreased;^{3, 32} this was because of the increase in available water molecules to form clusters with H_3O^+ , rather than a decrease in the drift tube voltage. The increased water vapor

concentration in the skimmer allowed U3 to be set higher while maintaining O_2^+ below 1% of the m19 signal (Figure 2-6). After U3 reached its limit of 200V, the strength of the O_2^+ (m/z 32) signal dropped as water flow increased or skimmer flow decreased.

2.4.2 Skimmer pumping capacity and drift tube water pressure

The increase in $H_3O^+(H_2O)$ signal was indicative of the pumping capacity of the skimmer being saturated. When it is saturated, the pressure difference across the orifice between drift tube and the skimmer was approximately zero. With the known flow rate of water vapor entering the IS, and the known pressure inside the skimmer, the throughput of the skimmer can be determined with the following relationships:⁵⁰

$$\text{Equation 1: } S_{Skim} = \frac{1013.25(mbar)}{P_{dt}} S_{STP}$$

where P_{dt} is the drift tube and skimmer pressure in mbar, S_{STP} is the volumetric flow rate at atmospheric pressure in $cm^3 \cdot min^{-1}$, and S_{Skim} is the volumetric flow rate of water within the skimmer. The effective pumping speed (S_{eff}) is obtained by converting S_{STP} to $L \cdot s^{-1}$ by multiplying by ($1.67 \times 10^{-5} \text{ min } L \cdot s^{-1} \cdot mL^{-1}$). By rearranging the relationship between the base pumping speed (S°) and the effective pumping speed (S_{eff}) to conductance (C , in $L \cdot s^{-1}$) (Equation 2), it is possible to obtain conductance of the skimmer tube (Equation 3):

$$\text{Equation 2: } \frac{1}{S_{eff}} = \frac{1}{S^\circ} + \frac{1}{C}$$

$$\text{Equation 3: } C = \frac{1}{\left(\frac{1}{S_{eff}} - \frac{1}{S^\circ} \right)}$$

where S° is the real pumping speed of the turbo pump ($L \cdot s^{-1}$), and C is the conductance of the skimmer orifice, in $L \cdot s^{-1}$. In this study, saturation of the pumping capacity of the

skimmer at each valve setting was defined as the point where signal for m37 exceeds 10% of the m19 signal. S_{STP} is the ion source water flow rate required to exceed the 10% saturation point. S° is estimated from the given pumping speed of air in the turbo pump (Pfeiffer TMP 071P, rated pumping speed of $3.3 \times 10^1 \text{ L}\cdot\text{s}^{-1}$) was reduced by 22% to $2.4 \times 10^1 \text{ L}\cdot\text{s}^{-1}$ due to the splinter screen that is in place to protect the pump blades.⁵¹ The actual pumping speed is likely somewhat less, as this pump also draws gas from the orifice at the bottom of the drift tube. However, S° is much larger than S_{eff} therefore large variations in its value will have negligible effects on the conductance of the skimmer tube; to obtain a 1% drop in the estimated conductance at the largest metering valve position, the S° would have to be $7.6 \text{ L}\cdot\text{s}^{-1}$.

Valve positions, equivalent skimmer tube lengths, saturation IS water flow rates (S_{STP}), S_{eff} and C values are given in Table 2-2. This shows that the metering valve assembly provides a range of conductance between 5.1×10^{-2} and $1.1 \times 10^{-1} \text{ L}\cdot\text{s}^{-1}$. In comparison, the original 32 cm skimmer tube that came with our standard sensitivity PTR-MS has a conductance of $1.1 \times 10^{-1} \text{ L}\cdot\text{s}^{-1}$, and a 40 cm skimmer tube, which is similar in length on our other PTR-MS instrument, has a conductance of $1.0 \text{ L}\cdot\text{s}^{-1}$. For a 20 cm tube, it was not possible to obtain a stable discharge and generate an m37/m19 ratio greater than 0.10. The largest ratio m37/m19 ratio obtained with the 20 cm tube (4%) was used to determine the conductance instead. This was accomplished by extrapolating through the closest m37/m19 ratios determined with the 32 and 40 cm tubes (5% and 4% respectively), with a resulting conductance of $1.4 \times 10^{-1} \text{ L}\cdot\text{s}^{-1}$. The 20 cm would have required $\sim 16 \text{ mL}\cdot\text{min}^{-1}$ (at standard temperature and pressure) of H_2O to reach an m37/m19 ratio of 10%. Considering that the upgraded instrument was previously operated with a 10 cm long tube, and an ion source

water flow rate of 11 mL min^{-1} , there was likely very little water present in the skimmer region, explaining the low primary ion signal.

Having established the pumping speed of the skimmer, it is also possible to estimate the partial pressure of water released into the drift tube from the ion source. The pressure in the drift tube is controlled by a pressure controller (Bronkhorst), connected to the PTR-MS backing pump [Figure 2-1 (H)]. This evacuates a small region separated from the drift tube by a stainless steel capillary that restricts the gas flow into the drift tube [Figure 2-1 (C)]. Measurements of this pressure are used to determine the amount of water in the drift tube because the pressure is inversely proportional to the gas flow through the capillary. The larger the pressure difference between the capillary inlet and pressure in the drift tube, the larger the flow of air through the capillary. When air from the inlet is the predominant source of gas in the drift tube and air from the drift tube is not drawn through the skimmer, the pressure controller measured an inlet pressure (PC_{eq}) of $373.00 \pm 0.25 \text{ mbar}$ (this condition is indicated by $\text{H}_3\text{O}^+(\text{H}_2\text{O})$ being $\sim 10\%$ of the total primary ion signal). A decrease in the inlet pressure from this point represents an increase in the amount of water added to the drift tube from the ion source, as less air needs to be added to the drift tube to maintain its pressure at 2.0 mbar . The flow of air into the drift tube, and thus the partial pressure should decrease proportionally to the drop in pressure recorded by the pressure controller. Accordingly, the partial pressure of water vapor in the drift tube can be estimated by the ratio between the inlet pressure when only air is in the drift tube (PC_{eq}) to the inlet pressure under other conditions (PC_p) using Equation 4:

$$\text{Equation 4: } P_{\text{H}_2\text{O}} = P_{dt} \left(1 - \frac{PC_p}{PC_{eq}} \right)$$

where P_{H_2O} is the partial pressure of water vapor in the drift tube, P_{dt} is the drift tube pressure, PC_p is the pressure controller reading at a given setting, and PC_{eq} is the pressure controller reading when gas flow between the IS and the drift tube is determined to be zero (373.00 mbar for this instrument). Equation 4 is a very important relationship because it provides a combined metric of water and skimmer flows. When this relationship yields a negative value for P_{H_2O} , it implies that air is being drawn from the drift tube into the skimmer, requiring more air to enter from the inlet, and thus there is a greater inlet pressure.

Using Equation 4, it is possible to express the measurements as a function of water vapor pressure in the drift tube. A plot of the measured distributions of water clusters at different partial pressures of water is shown in Figure 2-7. The estimated partial pressure of water from the ion source varied between 0.00 and 0.33 mbar. This can be thought of as artificially adding moisture to the sample stream entering the drift tube, and giving a RH of 208% for air at 45° C (the temperature of the drift tube and inlet lines) or 625% for air at 25° C.⁵² For comparison, Warneke et al.³² extrapolated humidity calibrations of ambient air to determine that the flow rate of water into the drift tube was about $3.0 \times 10^{-3} \text{ L} \cdot \text{s}^{-1}$. This result was obtained with a drift tube pressure of 2.5 mbar, and the IS water controller set to $8.0 \text{ cm}^3 \cdot \text{min}^{-1}$, resulting in a partial pressure of $3.25 \times 10^{-3} \text{ mbar H}_2\text{O}$ of water vapor in the drift tube. Tani et al.²⁹ employed the same extrapolation technique and found a relative humidity enhancement of 20%. These comparisons are relevant because it would seem that different PTR-MS instruments introduce different amounts of water into the drift tube. They also provide a contrast to the comparatively coarse metric provided here: each increase in water flow rate through the ion source resulted in a relative humidity enhancement of 53% (for air at 25° C) at each valve position during this experiment.

The partial pressure of water vapor in the drift tube is also related to the efficiency of the ion source at generating the total primary ion signal ($\Sigma\text{H}_3\text{O}^+(\text{H}_2\text{O})_n$, $n=0\dots2$) (Figure 2-7, yellow circles). By selecting combinations of ion source water flow and skimmer region gas flow that result in water leaving the ion source, the amount of air entering the ion source was reduced and the efficiency of primary ion signal generation improved. Under conditions where air was drawn from the drift tube into the skimmer region, the efficiency of $\text{H}_3\text{O}^+(\text{H}_2\text{O})_n$ generation was poor and the total primary ion signal was less than 3 MHz. The total primary ion signal increased with the partial pressure of water until the partial pressure reaches ~ 0.2 mbar with a peak of 5.5 MHz. Thereafter, the total primary ion signal decreased to 4.5 MHz.

2.4.3 Sensitivity and Fragmentation Study

After exploring the behavior of the ion source at different skimmer flow set points, a repeat set of measurements was conducted to explore how water entering the drift tube from the ion source would affect response for a suite of compounds. During this test, similar patterns of cluster formation and ion signal intensity were observed during the fragmentation and sensitivity study (Figure 2-9). It was not possible to test the exact range of water and flow settings as in the previous experiments: O_2^+ counts were harder to suppress and discharges formed more easily in the skimmer region. Shortly after the sensitivity study was completed, the hollow cathode ion source required cleaning to remove excess ion burn. The more limited functional range of the IS in this study is thus attributed to degradation of the overall ion source performance.

NO^+ (m30) ions were also measured in this study (Figure 2-9c). NO^+ exhibited a maximum at a water flow rate of $10 \text{ cm}^3\cdot\text{min}^{-1}$ and a conductance of $6.8\times 10^{-2} \text{ L}\cdot\text{s}^{-1}$. Under

these conditions, the partial pressure of water in the drift tube was estimated to be 0.13 to 0.17 mbar, and the presence of water in the drift tube was verified by the cluster distributions in this range. In spite of this, air was diffusing into the ion source. This behavior is not observed at higher skimmer flow rates, implying that the pumping speed of the skimmer suppressed NO^+ formation by pumping the air away from the orifice, preventing NO^+ from being injected into the drift tube.

The results of the sensitivity study are displayed in three different ways in Figure 2-10. First, the signal of each compound (in Hz) was divided by the mixing ratio of the compound measured (Hz ppbv^{-1}) (Table 2-1). This provides the relative sensitivity of each compound to be compared, even though they are at different mixing ratios in the calibration gas. This metric has been periodically used as a response factor reported by other groups.⁵³ Second, the calibration factor, which is commonly used to express PTR-MS response to different compounds, was calculated. The calibration factor is the sensitivity normalized to the signal at m19, and multiplied by a factor of 10^6 , and is denoted as $\text{ncps}\cdot\text{ppbv}^{-1}$ as follows:

Equation 5:
$$\frac{\text{ncps}}{\text{ppbv}} = \frac{\text{Hz}}{\text{ppbv}} \times \frac{10^6}{\text{m19}}$$

This method provides a relative value to compare with other values presented in the literature for different instruments. Under conditions where H_3O^+ is not the primary ionizing species, the metric breaks down as other sources of protons cause values of $\text{ncps}\cdot\text{ppbv}^{-1}$ to grow larger, although the detection limit increasing and ionization efficiency is actually decreasing. This error leads to the third method used here, where the sensitivity is normalized to the total measured primary ion signal, and is expressed in this work as $\text{cncps}\cdot\text{ppbv}^{-1}$ in the following expression:

Equation 6:
$$\frac{cncps}{ppbv} = \frac{Hz}{ppbv} \times \frac{10^6}{(m19 + m37 + m55)}$$

This expression is a useful metric for considering the impact of water vapor on the sensitivity of PTR-MS type instruments in situations where there are large numbers of cluster ions.^{11, 15, 29, 54} It provides a uniform measure of response to compounds, under any given set of drift tube conditions. For example, the value of Equation 6 will decrease as the availability of protonating species in the drift tube decreases; for compounds with proton affinities close to that of water, like benzene, toluene, hydrogen cyanide, and formaldehyde the value of $cncps \cdot ppbv^{-1}$ will decrease as the relative dominance of protonated clusters in the drift tube increases.^{32, 45, 55} For this discussion $Hz \cdot ppbv^{-1}$ will be referred to as the sensitivity, $ncps \cdot ppbv^{-1}$ will be called the calibration factor, and $cncps \cdot ppbv^{-1}$ will be termed the cluster normalized response.

Overall, several trends in signal, calibration factor, and cluster normalized response were very consistent across the range of possible skimmer flow and water flow settings. The maximum signal and calibration factors for all compounds occurred in the region where H_3O^+ and $H_3O^+(H_2O)$ are both very high and H_3O^+ was the dominant ion. As $H_3O^+(H_2O)_2$ became the dominant form of the primary ion signal, the signal for all compounds in the calibration mixture dropped. This shows that for most compounds, the best instrumental performance (maximum signal) was obtained when H_3O^+ was maximized. Maximizing H_3O^+ may occur with elevated amounts of $H_3O^+(H_2O)$, which is typically viewed in a negative light because it is construed as meaning that H_3O^+ is lost to cluster formation that might otherwise be ionizing target compounds. However, if the relative increase in H_3O^+ is greater than the relative increase in $H_3O^+(H_2O)$, then there is still be a net gain in H_3O^+ available to react, and thus a net increase in signal.

The cluster normalized response of the compounds measured is plotted against the fraction of the total primary ion signal that is composed of clusters in Figure 2-11 through Figure 2-15. This way of displaying the data shows how cluster normalized response decreases as clusters become more prevalent in the drift tube. It has the shortcoming that the impact of higher clusters gets compressed at the far right of the graph, and thus only serves as a loose proxy. These plots are color coded by valve position to show that some compounds have cluster normalized responses that also change with gas flow through the ion source skimmer region.

The trends in cluster normalized response follow the proton affinity of the target compounds (the proton affinities of the first three $\text{H}_3\text{O}^+(\text{H}_2\text{O})_n$ clusters and the compounds target compounds used in this study are shown in Figure 2-8). The variation in the measurements correlated with proton affinity of the compound in question, with very little variation in the cluster normalized response of benzene at similar cluster fractions (Figure 2-11), while there was a large amount of variation in the cluster normalized response for camphene (Figure 2-15). Matching colored lines have been drawn along the trends in cluster normalized response for each valve position, and an arrow is included showing that increased skimmer flow caused the cluster normalized response to decrease at high cluster fractions (and higher water levels) for this compound. The result bears some resemblance recent studies on the affect of the ion source discharge current on the fragmentation of alcohols.⁵⁶ However, in this experiment, the ion source discharge current was constant at 8 mA. This result indicates that the flow of gases in the skimmer region impacted instrument response in other ways than simply preventing water vapor from entering the drift tube.

The response of the PTR-MS to different compounds in the calibration mixture was strongly dependent on their proton affinity. Compounds having a low proton affinity

showed a linear decrease in response, those with a higher proton affinity exhibited consistent response until $\text{H}_3\text{O}^+(\text{H}_2\text{O})$ or $\text{H}_3\text{O}^+(\text{H}_2\text{O})_2$ became the dominant cluster in the primary ion signal (Figure 2-8). The calibration factors decreased more for compounds with low proton affinity values than for compounds with higher proton affinities. Figure 2-11 shows the decrease in cluster normalized response to benzene as $\text{H}_3\text{O}^+(\text{H}_2\text{O})_n$ clusters became the dominant members of the primary ion signal. Benzene has the lowest proton affinity ($750 \text{ kJ}\cdot\text{mol}^{-1}$) of the group of test compounds, and its cluster normalized response decreased monotonically with increasing abundance of protonated clusters. A feature that was apparent in all other compounds was a decrease in the cluster normalized response after the fraction of protonated clusters increased over 0.8 of the total primary ion signal. In this regime, $\text{H}_3\text{O}^+(\text{H}_2\text{O})$ (m37) was decreasing and $\text{H}_3\text{O}^+(\text{H}_2\text{O})_2$ (m55) was increasing as water vapor pressure in the drift tube increased above 0.18 mbar. When this shift occurred, the target compound was being protonated at a lower rate (or not at all) by one or more of the protonated clusters present.

The cluster normalized response for toluene is shown in Figure 2-12. Toluene has a proton affinity of $785 \text{ kJ}\cdot\text{mol}^{-1}$, while the first hydrated cluster, $\text{H}_3\text{O}^+(\text{H}_2\text{O})$ (m37), has an estimated proton affinity of $828 \text{ kJ}\cdot\text{mol}^{-1}$, making the proton transfer reactions from clusters endothermic by $44 \text{ kJ}\cdot\text{mol}^{-1}$.⁴⁹ Even with the small amount of energy gained by motion in the electric field ($\approx 10 \text{ kJ}\cdot\text{mol}^{-1}$), as described by the Wannier expression to determine the effective temperature of the ions (T_{eff})⁵⁷ there is not enough available energy to initiate an endothermic proton transfer reaction, making its behavior similar to benzene. However, the cluster normalized response decreases more quickly when $\text{H}_3\text{O}^+(\text{H}_2\text{O})_2$ becomes the dominant cluster in the drift tube.

Similarly, acetone (Figure 2-14) demonstrated a very uniform cluster normalized response to $\text{H}_3\text{O}^+(\text{H}_2\text{O})$ and H_3O^+ , with a mild decrease in cluster normalized response until hydrated clusters exceeded a value of 0.8 of the total primary ion signal. Proton transfer reactions between acetone and hydrated clusters are endothermic, but by a much smaller margin than with toluene ($\approx 7 \text{ kJ}\cdot\text{mol}^{-1}$ for reactions with $\text{H}_3\text{O}^+(\text{H}_2\text{O})$).

Isoprene (Figure 2-13) did not have the same negative trend, instead showing an increase in cluster normalized response peaking at a cluster fraction of 0.2, corresponding to the maximum in the total ion signal. The cluster normalized response slightly decreases from 12.3 cncps at its peak to 10.4 cncps when clusters constitute a fraction of 0.8 of the primary ion signal, where after it rapidly decreases as $\text{H}_3\text{O}^+(\text{H}_2\text{O})_2$ increases. It is expected that the reaction would be facile at low cluster fractions as the proton transfer reaction between $\text{H}_3\text{O}^+(\text{H}_2\text{O})$ and isoprene is exothermic by $9 \text{ kJ}\cdot\text{mol}^{-1}$. However, the reaction is still endothermic with respect to $\text{H}_3\text{O}^+(\text{H}_2\text{O})_2$ (proton affinity of $884 \text{ kJ}/\text{mole}$) by $-49 \text{ kJ}\cdot\text{mol}^{-1}$, explaining the decrease at high cluster fractions.

Camphene showed a similar trend to isoprene, with a maximum sensitivity of $5.4 \text{ cncps}\cdot\text{ppbv}^{-1}$ when clusters comprise 0.2 of the primary ion signal; sensitivity does not diminish after the fraction of protonated clusters in the primary ion signal exceeds 0.8. Table 3 shows the drop in sensitivities for the measured compounds as the cluster composition of the primary ion signal shifts to $\text{H}_3\text{O}^+(\text{H}_2\text{O})_n$ as the dominant primary ion signal.

An interesting application of this data is that it can provide a general prediction of proton affinity. There is no published value for the proton affinity of camphene. However, the proton affinity for monoterpenes is usually around $875 \text{ kJ}\cdot\text{mol}^{-1}$ (Figure 2-8, MT Low), although there is limited data available for these compounds.^{29, 58-60} It is possible to bracket

the proton affinities of monoterpenes by examining similar compounds. On the low end by 1-methylethylbenzene ($792 \text{ kJ}\cdot\text{mol}^{-1}$), which has been used as a proton affinity proxy for p-cymene, and on the high end by the $\text{C}_{10}\text{H}_{16}$ isomer, 3-methylene-1,5,5-trimethylcyclohexene ($905 \text{ kJ}\cdot\text{mol}^{-1}$) (Figure 2-8, MT High).^{29,61} For the low case, the proton transfer reaction with $\text{H}_3\text{O}^+(\text{H}_2\text{O})_2$ ($-884 \text{ kJ}\cdot\text{mol}^{-1}$) would be endothermic by $92 \text{ kJ}\cdot\text{mol}^{-1}$, but for the high case, it would be exothermic by $-21 \text{ kJ}\cdot\text{mol}^{-1}$. Since camphene is detected when high cluster fractions $\text{H}_3\text{O}^+(\text{H}_2\text{O})_3$ are dominant, the data indicates that the proton transfer reaction between camphene is exothermic, so the proton affinity of camphene must be near $884 \text{ kJ}\cdot\text{mol}^{-1}$. Accounting for the excess energy provided by the T_{eff} of $\text{H}_3\text{O}^+(\text{H}_2\text{O})_2$ ions moving in the drift tube (another $\approx 10 \text{ kJ}\cdot\text{mol}^{-1}$), that value decreases to $875 \text{ kJ}\cdot\text{mol}^{-1}$.

This experiment also provides some delineation between fragmentation processes controlled by ion molecule collisions in the drift tube and fragmentation caused by the energy of the proton transfer reaction. Here, the field strength of the drift tube was constant (132 Td), and the increasing amounts of water in the drift tube increased cluster formation. For camphene, the degree of fragmentation decreases linearly as dominance of clusters increases. It reaches a minimum at a flow controller set point of $14 \text{ cm}^3\cdot\text{min}^{-1}$ and a valve setting of $7.0 \times 10^{-2} \text{ L}\cdot\text{s}^{-1}$, leading to a partial pressure of water of 0.35 mbar (Figure 2-16), and corresponding to the largest fraction of protonated clusters in the primary ion signal. This result is indicative that fragmentation of monoterpenes can be controlled by changing the distribution of hydrated clusters formed by the ion source. The change in fragmentation ratio at the points where H_3O^+ and $\text{H}_3\text{O}^+(\text{H}_2\text{O})$ are at their respective maxima are listed at the bottom of Table 2-3.

2.5 Conclusions

The flow rate of gas through the skimmer region of the PTR-MS instrument impacts the performance of the ion source and the amount of water in the drift tube reaction chamber. By selecting combinations of gas flow through the skimmer and water flow into the ion source, the amount of excess water vapor entering the drift tube can be controlled. This allows a coarse selection of the dominant hydrated water cluster in the drift tube, which offers a degree of selectivity for analyte species beyond the proton affinity of water.

Different combinations of ion source water flow and gas flow through the skimmer also impact the total primary ion signal of the ion source. The highest primary ion current was obtained when the combined flow rates led to a partial pressure of water in the drift tube of 0.2 mbar. In the extremes of low ion source water flow and high skimmer flow rates, and high water flow and low skimmer flow, the ion source functions poorly. For conditions where large amounts of air were in the skimmer region, the ion source generated large amounts of O_2^+ , under conditions where there were large amounts of water vapor flowing out of the ion source into the drift tube, secondary discharges formed in the skimmer region, interfering with the generation of a stable primary ion signal.

The response of the PTR-MS to different compounds decreased as clusters became the dominant form of the total primary ion signal. For compounds with a low proton affinity, the response decreased simultaneously as the amount of H_3O^+ decreased. Compounds with a higher proton affinity can be protonated by $H_3O^+(H_2O)$, and thus displayed a more uniform response until $H_3O^+(H_2O)_2$ dominated the primary ion signal. Fragmentation of camphene also decreased as the successively larger clusters became dominant, indicating that protonated clusters might a less destructive ionization source for

some compounds. Response also decreased for compounds with high proton affinities as the flow rate of gases through the skimmer increased.

The ability to tune the flow of gases through the ion source skimmer may be useful for future applications of PTR-MS instruments, where different reagent gases are used or where high sensitivity to compounds with low proton affinity is required. For example, this concept should be expanded to PTR-MS instruments that are modified for other modes of chemical ionization such as O_2^+ , NO^+ , and NH_3^+ . Previous publications using alternate ionization methods report H_3O^+ and other ions as contaminants to their primary ion signal stemming from air entering the ion source from the drift tube.^{44, 62} These might be reduced or eliminated by adjusting the skimmer flow to limit the amount of air entering the ion source.

In the next chapter, the distributions of protonated clusters in the primary ion signal and the cluster normalized response obtained here are compared to the output of a kinetic model that simulates the ion molecule chemistry that takes place within the drift tube.

2.6 Figures and Tables

Table 2-1. Mixing ratios of the compounds used to test the sensitivity of the instrument over a range of drift tube conditions.

Compound	m/z	Final ppbv
Acetone	59	7.0
Isoprene	69	3.3
Benzene	79	5.9
Toluene	93	5.8
Camphene	137	7.9

Table 2-2. The valve setting, equivalent tube length, water flow, calculated skimmer pumping speed, and calculated skimmer tube conductance values.

Valve Setting (A.U.)	Eq. Tube Length (cm)	S_{STP} ($\text{cm}^3 \cdot \text{min}^{-1}$)	S_{eff} ($\text{L} \cdot \text{s}^{-1}$)	C ($\text{L} \cdot \text{s}^{-1}$)
1.00	-	6.0	5.1×10^{-2}	5.1×10^{-2}
1.50	-	8.0	6.8×10^{-2}	6.8×10^{-2}
1.75	-	9.0	7.6×10^{-2}	7.6×10^{-2}
2.00	-	1.0×10^1	8.4×10^{-2}	8.4×10^{-2}
2.25	-	1.1×10^1	9.3×10^{-2}	9.3×10^{-2}
2.50	40	1.2×10^1	1.0×10^{-1}	1.0×10^{-1}
2.75	32	1.3×10^1	1.1×10^{-1}	1.1×10^{-1}
-	20	1.7×10^1	1.4×10^{-1}	1.4×10^{-1}

Table 2-3. The change in response factor when H_3O^+ is the dominant ion ($m_{19} > 90\%$ of the total primary ion signal) and when $\text{H}_3\text{O}^+(\text{H}_2\text{O})$ is the dominant species ($m_{37} > 50\%$ of the total primary ion signal). Generally, compounds with large proton affinities show a mild decrease in response while species with small proton affinities show a large decrease in response. Shaded areas are the total terpene signal measured at $m_{81}+m_{137}$, signal of the major camphene fragment (m_{81}) and the fragmentation ratio of m_{81}/m_{137} . Precision estimates are 1σ of the measurements in each bin.

Compound	m/z	PA (kJ·mol ⁻¹)	H_3O^+ Dominant (cncps·ppbv ⁻¹)	$\text{H}_3\text{O}^+(\text{H}_2\text{O})$ Dominant (cncps·ppbv ⁻¹)	% Drop
Camphene	137	840-915	4.8 ± 0.3	3.6 ± 1.1	25.13
Isoprene	69	826	9.5 ± 1.1	9.4 ± 1.4	1.29
Acetone	59	812	14.6 ± 0.7	10.3 ± 1.9	29.45
Benzene	79	750	9.7 ± 0.7	2.3 ± 0.8	76.55
Toluene	93	785	12 ± 0.4	4.6 ± 0.9	61.65
ΣTerpene	81+137	-	8.8 ± 0.4	5.3 ± 1.2	40.11
Terpene Fragment	81	-	3.9 ± 0.2	1.6 ± 0.4	58.52
Terpene Frag. Ratio	81/137	-	0.81	0.45	44.6

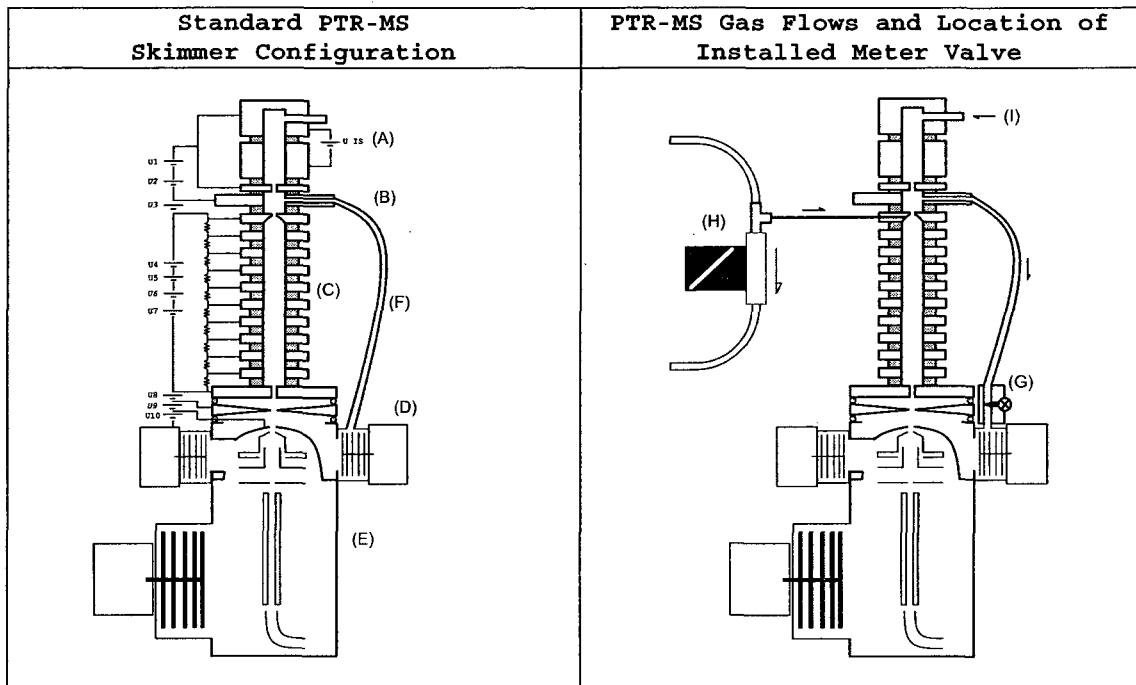


Figure 2-1. (A) Hollow cathode ion source, (B) Skimmer region, (C) Drift tube, (D) Intermediate vacuum region, (E) High vacuum and detection system, (F) Normal tube between skimmer and intermediate vacuum region, (G) metering valve installed between skimmer and intermediate vacuum region. Sample gas is introduced into the drift tube through a capillary at the top of the drift tube. The flow of air through the capillary is regulated by the pressure differential between the inlet and drift tube, controlled by a pressure controller (H). Water vapor is introduced into the ion source using a flow controller (I). The standard configuration diagram also shows the power supplies used to control the ion source and drift tube. Labels in *italic* are adjustable in software. All power supplies denoted as U_x , with the exception of U_9 , can vary from 0-200V. U_1+U_2 are denoted as U_{1+2} . U_{1+2} and U_3 are used to control extraction from the ion source. U_4 , U_5 , U_6 , and U_7 control the drift tube voltage. U_8 is an inactive power supply, jumpered to be inoperative (fixed at 0V). U_9 is the potential on the skimmer, and U_{10} is the voltage between pinhole and ground.

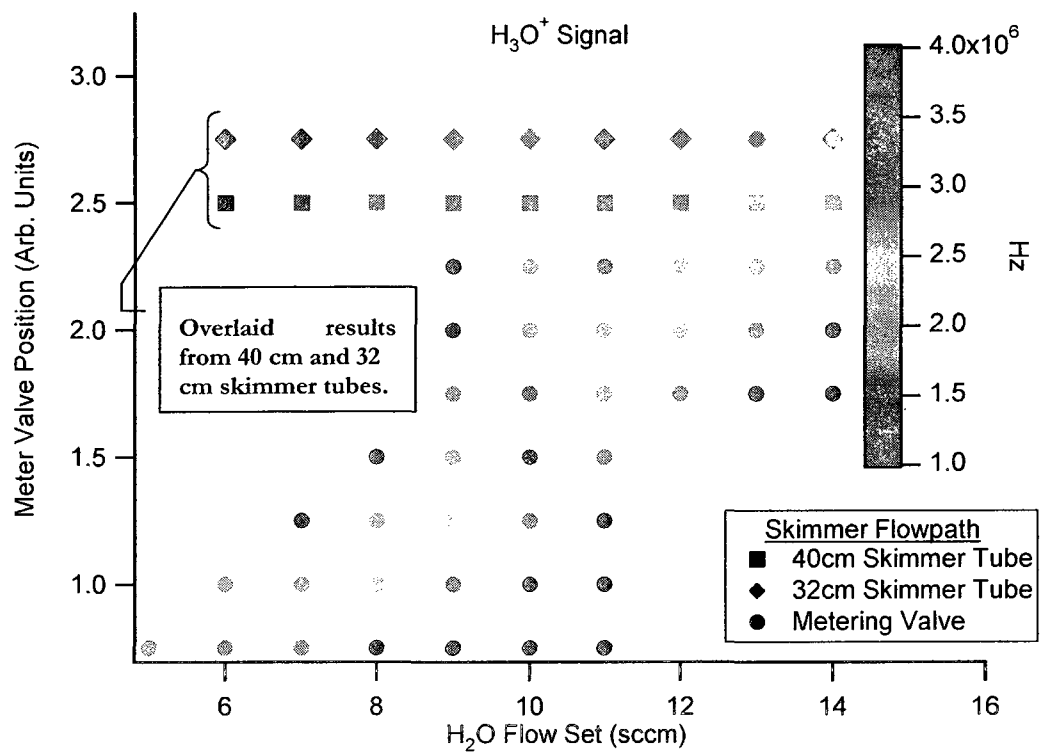


Figure 2-2. H₃O⁺ signal as a function of valve position and ion source water flow settings. Overlaid with the results obtained with the meter valve are measurements made with 32 cm (diamonds) and 40 cm (squares) skimmer tubes. The similarity between these measurements and those obtained with the meter valve demonstrate that the meter valve can obtain results similar to an unmodified PTR-MS instrument.

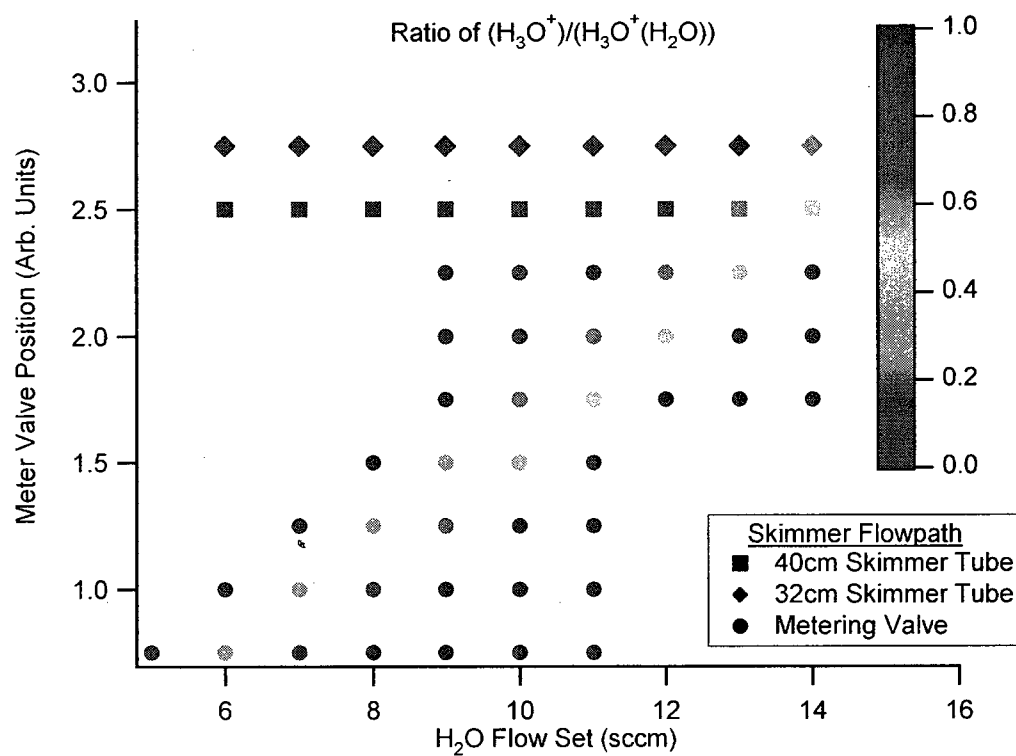


Figure 2-3. The ratio of H_3O^+ to $\text{H}_3\text{O}^+(\text{H}_2\text{O})$ as a function of meter valve position and ion source water flow, with overlaid results from 40 cm and 32 cm skimmer tubes.

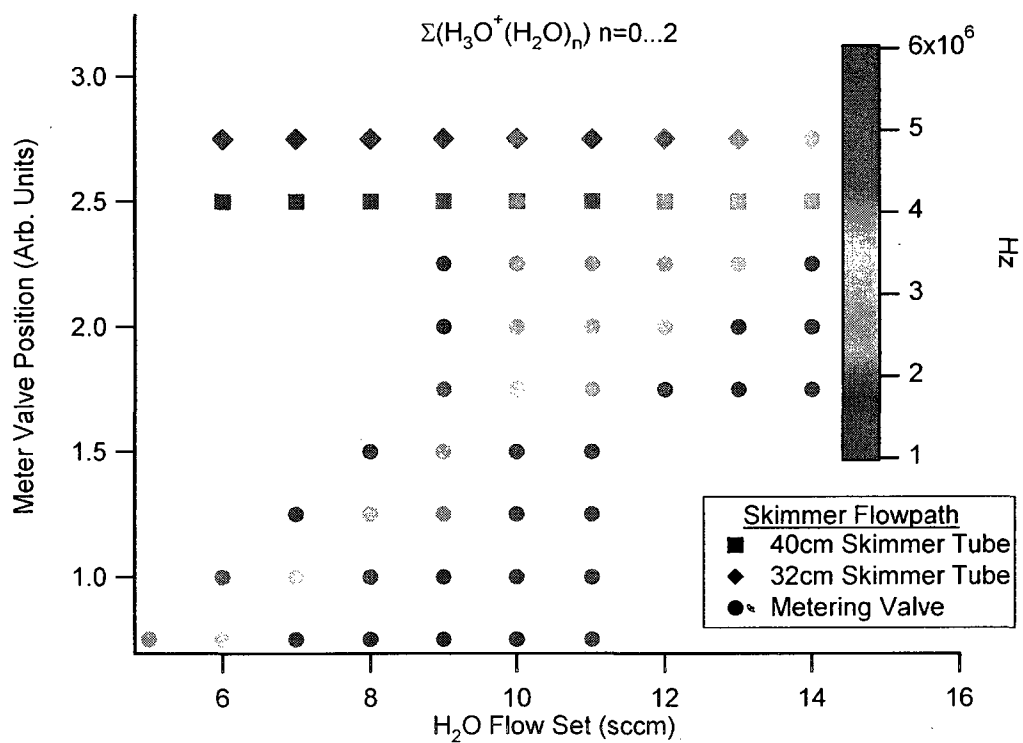


Figure 2-4. The total primary ion signal (the sum of all protonated water clusters) as a function of meter valve position and ion source water flow, with overlaid results from 40 cm and 32 cm skimmer tubes.

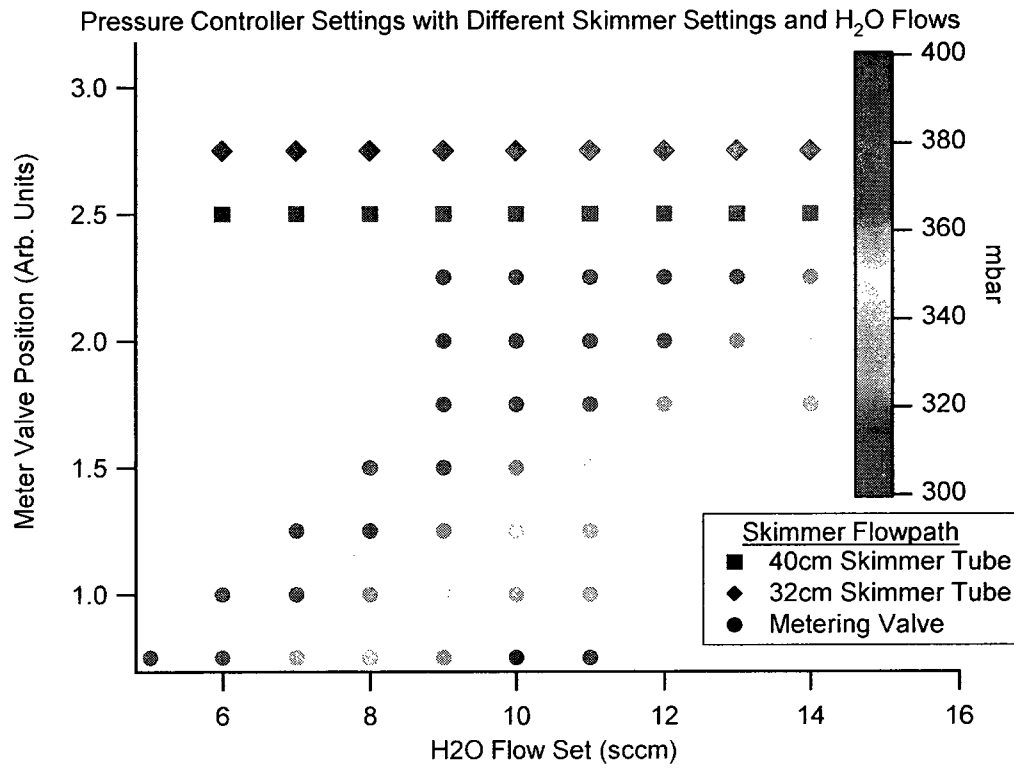


Figure 2-5. Pressure controller settings at various water flow and drift tube skimmer conditions, with overlaid results from 40 cm and 32 cm skimmer tubes.

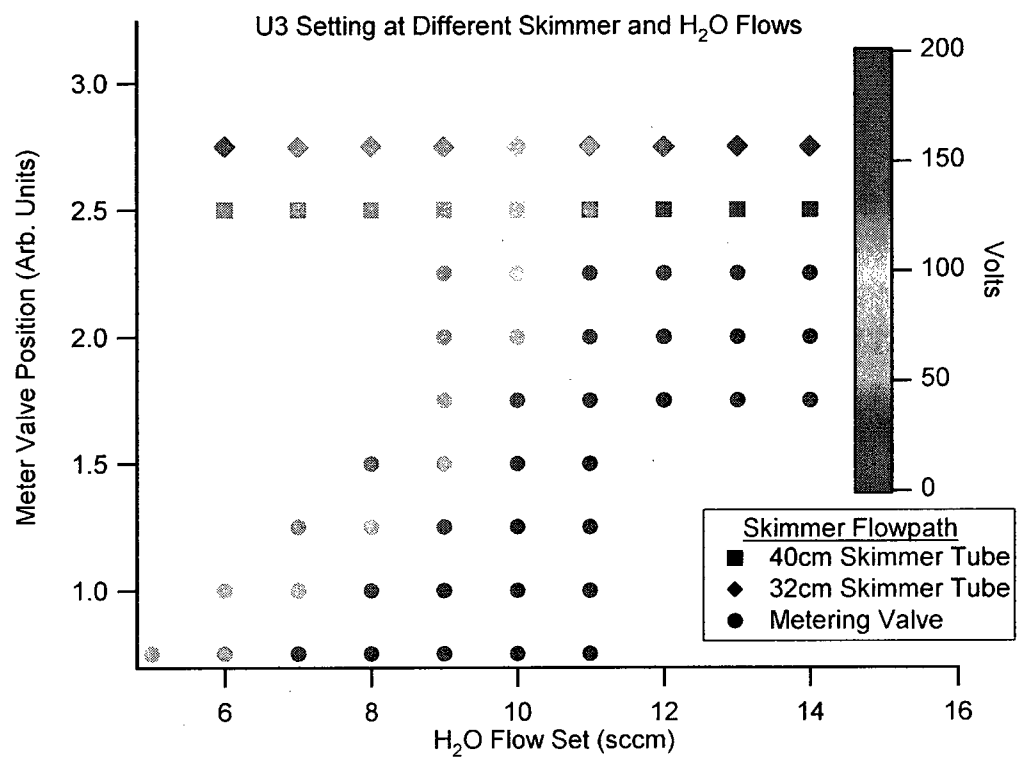


Figure 2-6. U3 voltage settings required to minimize O_2^+ to less than 1% of the $\Sigma H_3O^+(H_2O)_n$ signal at each meter valve position and ion source water flow setting, with 40 cm and 32 cm skimmer tube results overlaid.

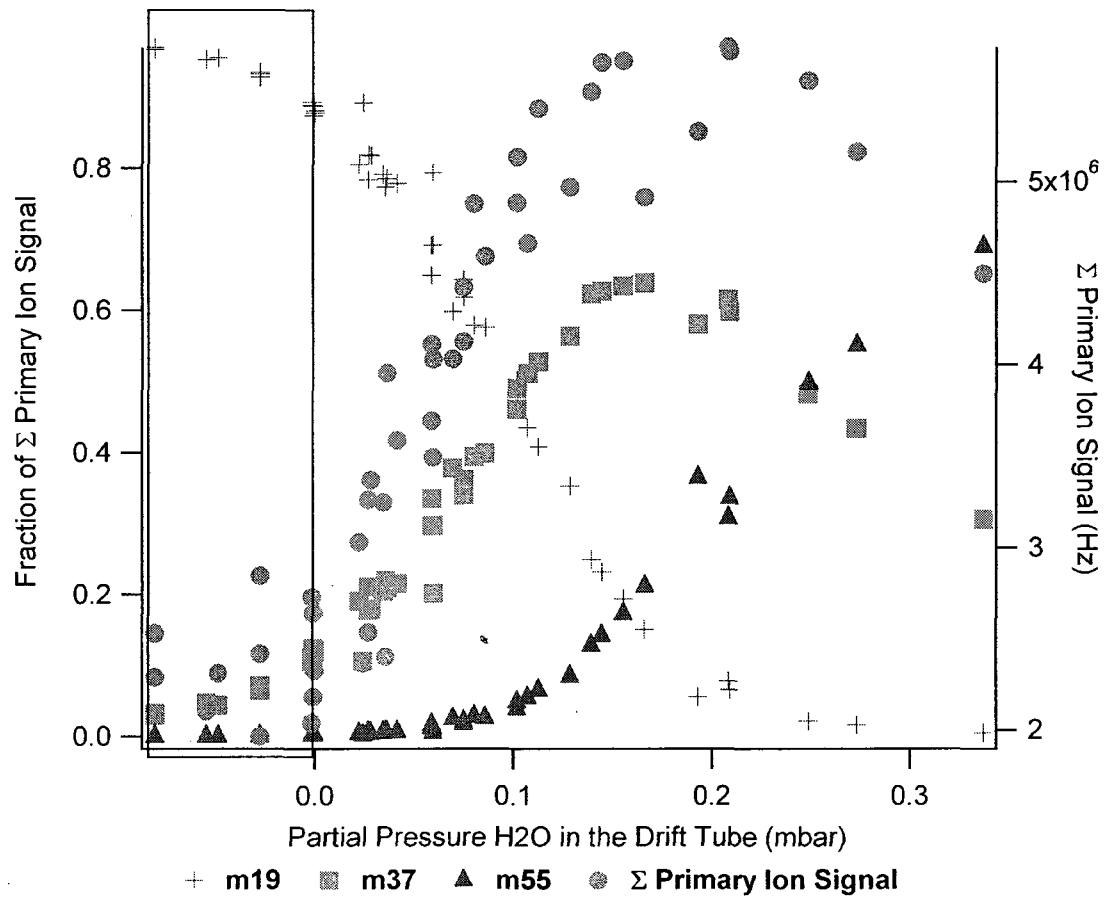


Figure 2-7. The composition (left axis, crosses (H_3O^+), squares ($\text{H}_3\text{O}^+(\text{H}_2\text{O})$), and triangles $\text{H}_3\text{O}^+(\text{H}_2\text{O})_2$) and intensity (right axis) of different $\text{H}_3\text{O}^+(\text{H}_2\text{O})_n$ clusters in the drift tube as the partial pressure of water increases. The region with a negative pressure (≤ 0.0 mbar, enclosed in a shaded box) represents conditions where air is flowing out of the drift tube and into the ion source skimmer region.

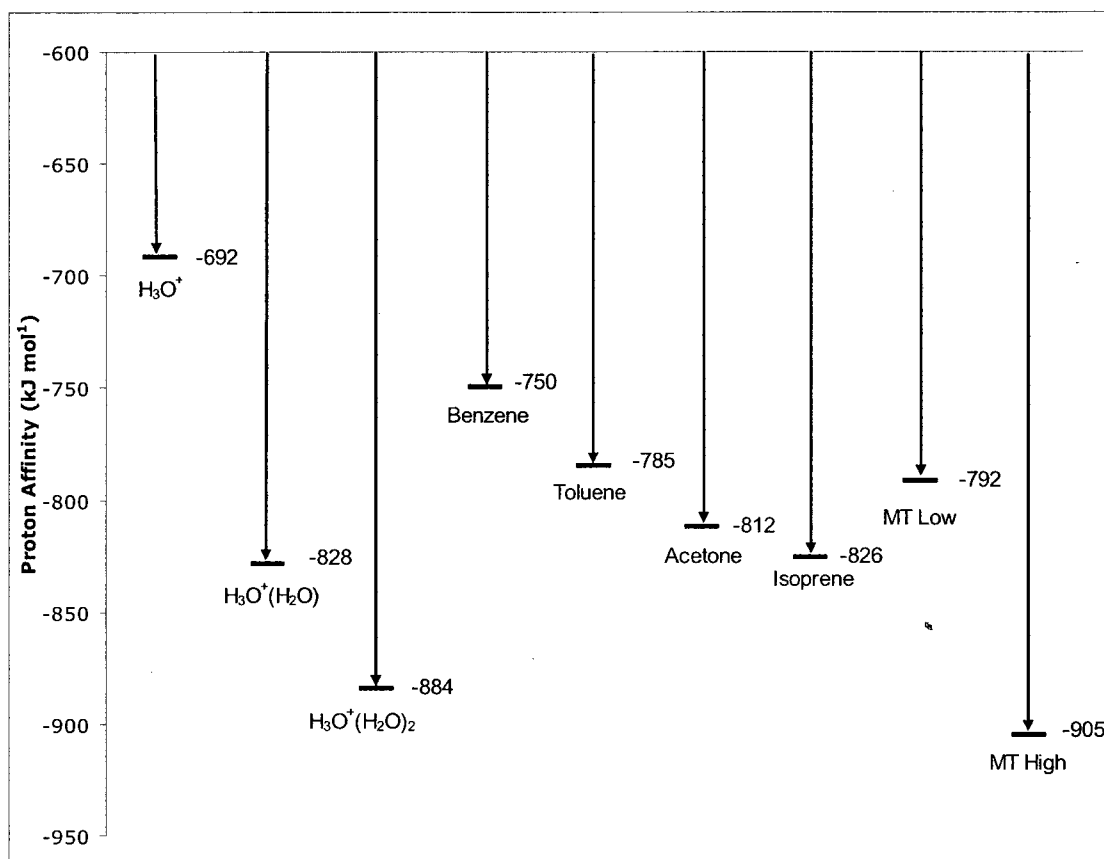
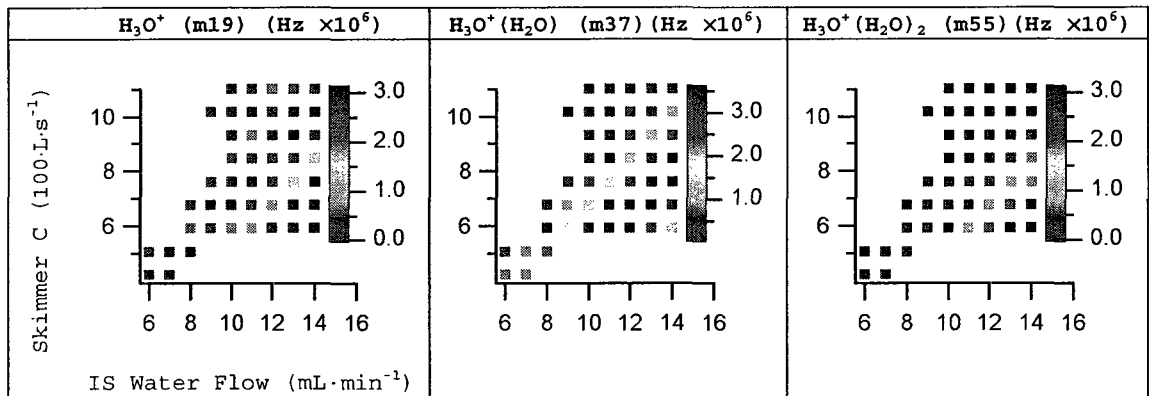
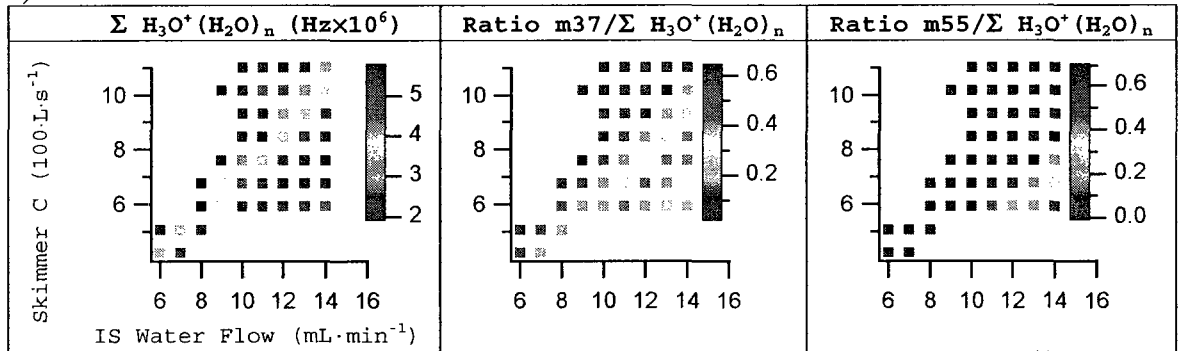


Figure 2-8. The proton affinity of the first three H₃O⁺(H₂O)_n clusters and the compounds for which the sensitivity was measured. The range of proton affinities for monoterpenes (MT) is given between the values of MT Low and MT High.

a)



b)



c)

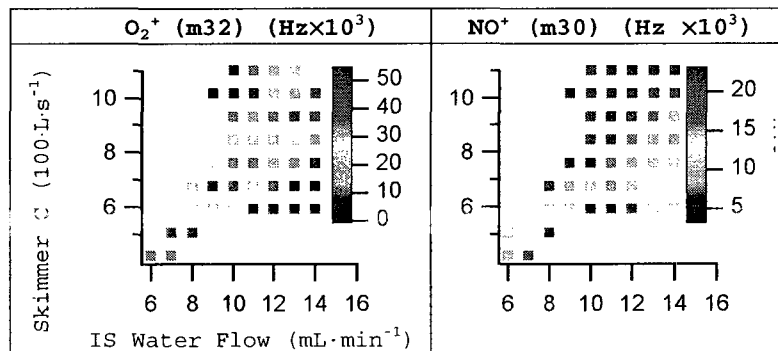


Figure 2-9. a) Graphs of H_3O^+ and protonated water clusters, b) total ion signal (m19+m37+m55) and the ratio of intensities, c) and ion source byproducts. Water flow rate through the ion source ($\text{mL} \cdot \text{min}^{-1}$) is on the abscissa, and conductance of the skimmer ($100 \cdot \text{L} \cdot \text{s}^{-1}$) is plotted on the ordinate.

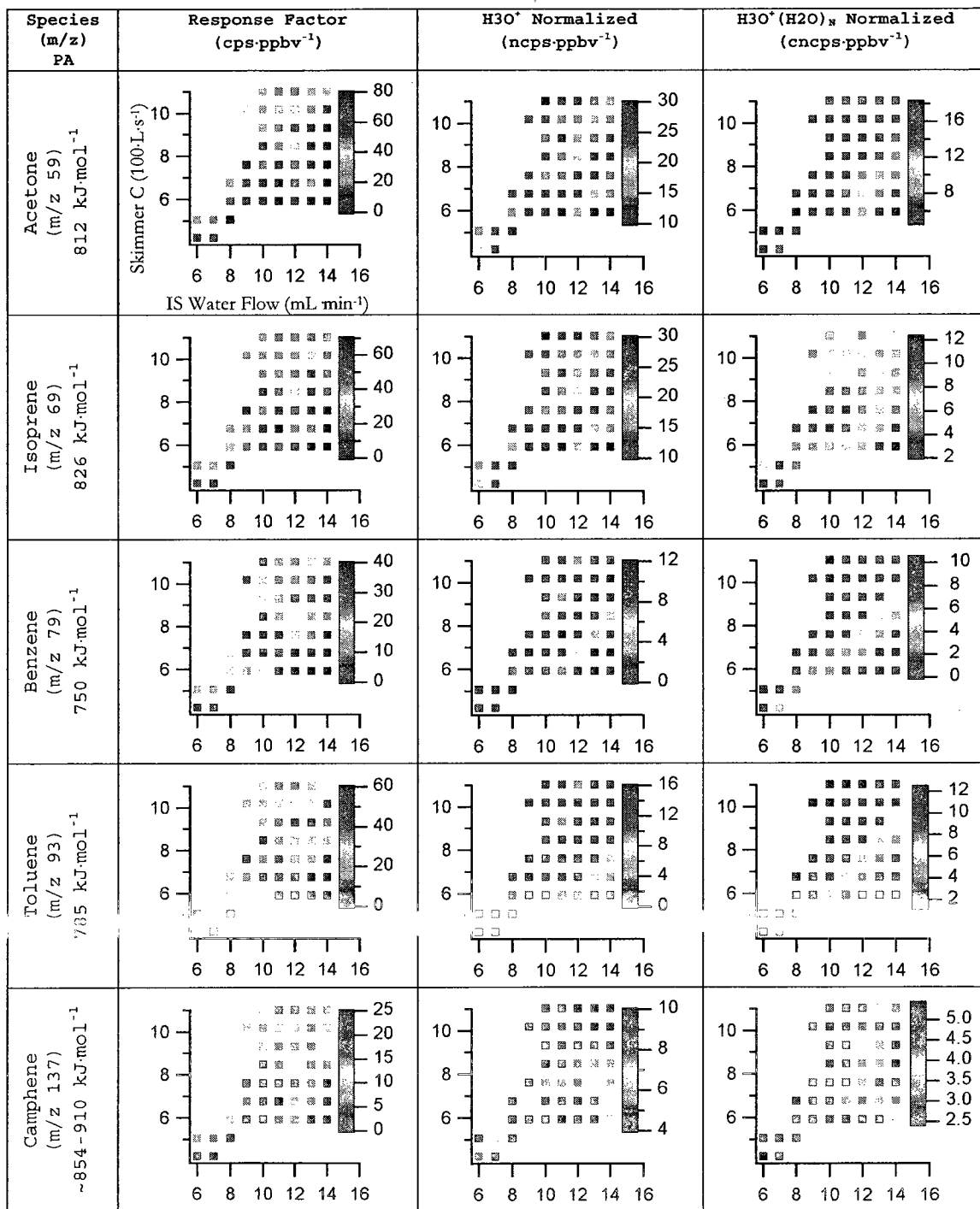


Figure 2-10. Response factors for acetone, isoprene, benzene, toluene, and camphene. Responses are given in cps·ppbv⁻¹ to show the relative response of each compound. ncps·ppbv⁻¹ is the normal calibration factor normalized to H₃O⁺. cncps·ppbv⁻¹ is the signal normalized to the total signal from all clusters. Water flow rate through the ion source (cm³·min⁻¹) is on the abscissa, and conductance of the skimmer is 100·L·s⁻¹

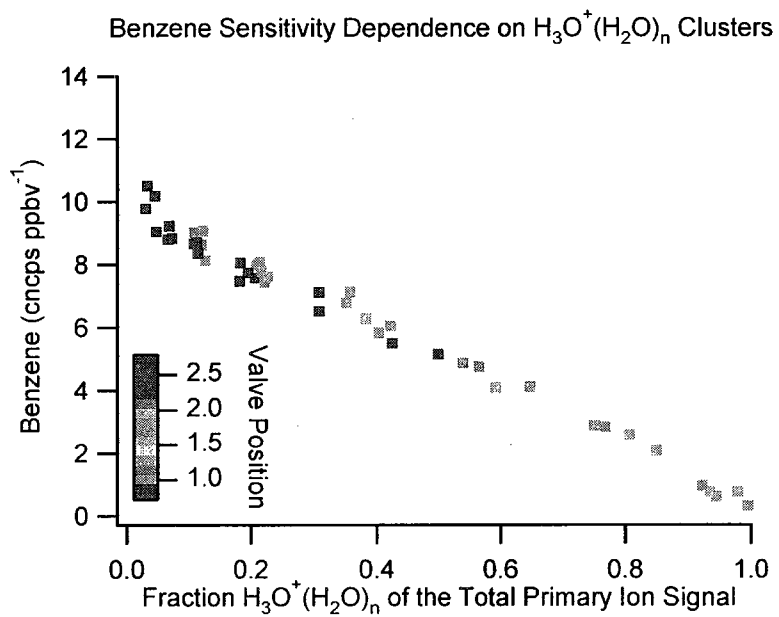


Figure 2-11. The cluster normalized response factor of benzene (m79) decreases as the relative ratio of protonated water clusters (m37 and m55 ($\text{H}_3\text{O}^+(\text{H}_2\text{O})_n$, $n \geq 1$) in the total primary ion signal (m19+m37+m55) increases.

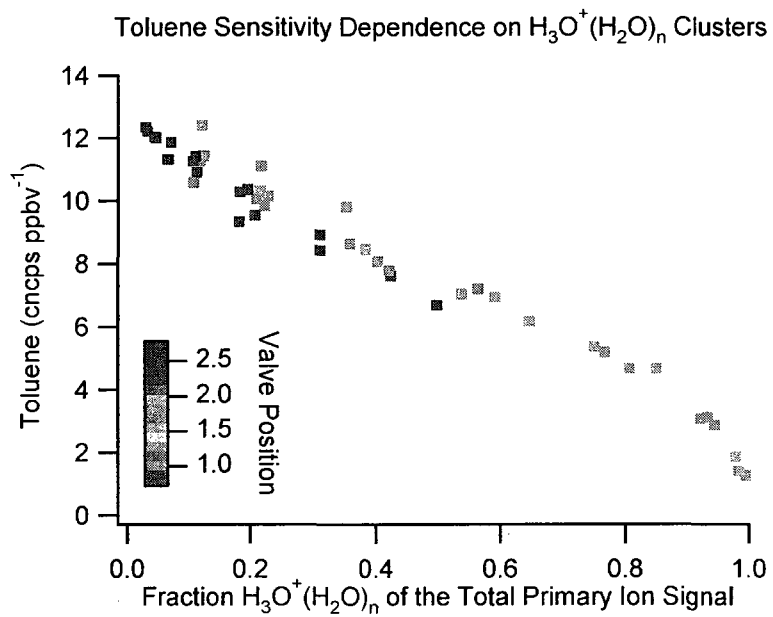


Figure 2-12. The decrease in the cluster normalized response factor of toluene (m93) with respect to the increase in the cluster fraction of the total ion signal. The decrease in sensitivity increases at the higher fraction where m19 is minimal and m55 becomes dominant.

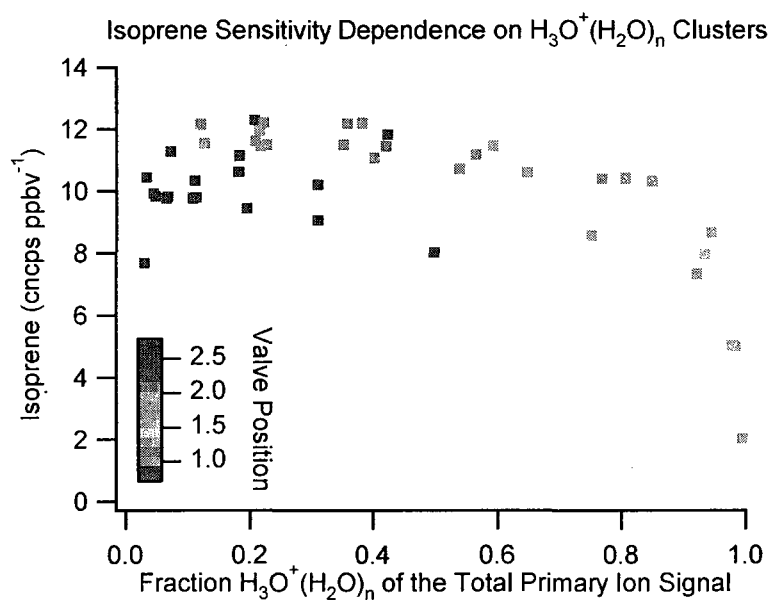


Figure 2-13. Isoprene (m69) does not show a decreasing cluster normalized response as clusters become the dominant fraction of the primary ion signal. Isoprene shows an increase in sensitivity that corresponds to the maximum in the total primary ion signal that coincides with a cluster fraction of ~ 0.2 . The response factor decreases rapidly at high fractions, where the $\text{H}_3\text{O}^+(\text{H}_2\text{O})_2$ cluster becomes dominant.

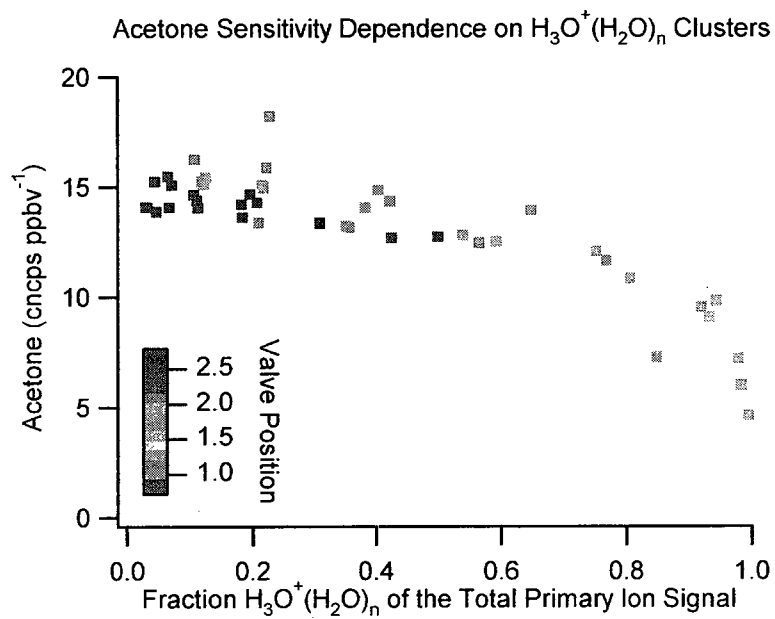


Figure 2-14. The cluster normalized response of acetone as clusters become larger fractions of the total primary ion signal.

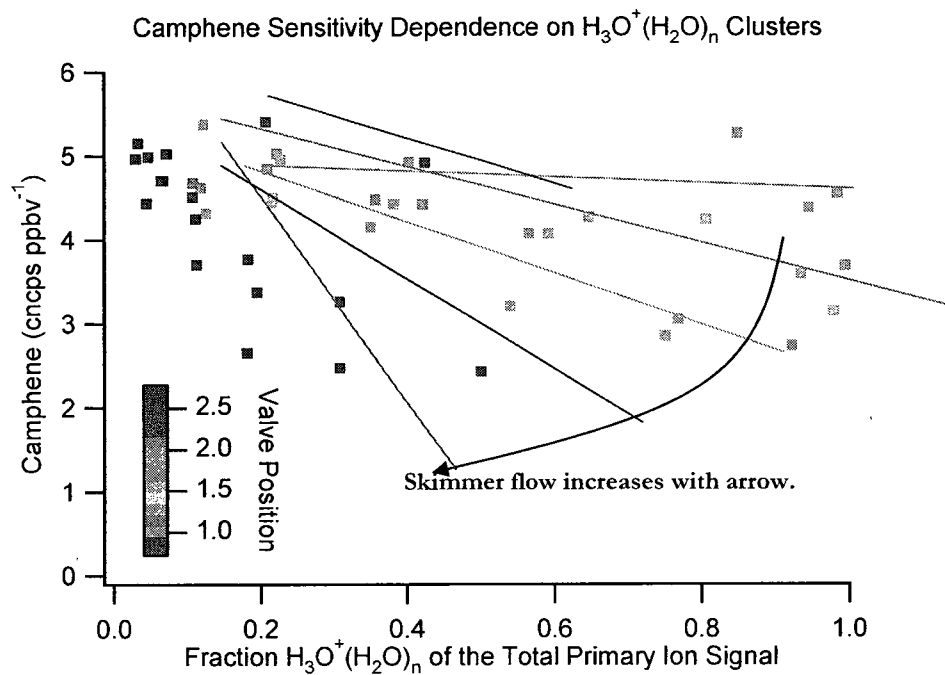


Figure 2-15. The cluster normalized response of camphene. There is a large amount of variation in the response of camphene over the range of tests in comparison to benzene. By color coding the results by meter valve position, it is shown that higher flow rates through the skimmer reduce the response as clusters become the dominant ionizing species.

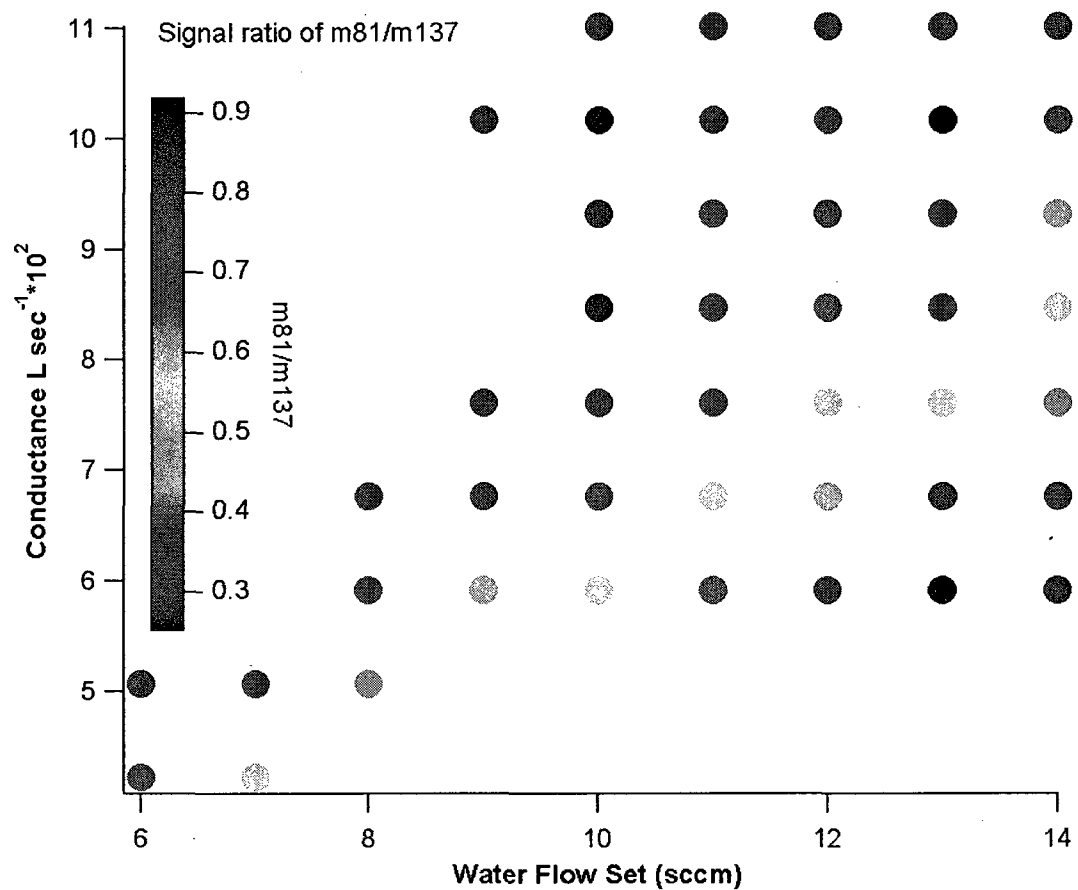


Figure 2-16. The ratio of m81/m137 as a function of skimmer flow and ion source water flow, showing that camphene fragmentation decreases as the size of the protonating clusters increases.

CHAPTER 3

MODELING CLUSTER DISTRIBUTIONS IN THE PTR-MS DRIFT TUBE AND IMPLICATIONS FOR THE KINETICS OF CLUSTER REACTIONS

3.1 Introduction

In the previous chapter, the effect of different combinations of ion source water flow and skimmer flow rates on sensitivity and protonated cluster distributions in the PTR-MS ion source was presented. It was shown that water cluster distributions increase in situations where the ion source water flow is greater than the skimmer evacuation rate, increasing the water vapor pressure in the drift tube as a result. As the hydronium ion (H_3O^+) becomes less dominant in the drift tube due to competitive cluster formation and destruction reactions with water, the PTR-MS becomes less sensitive to compounds that cannot be protonated by $\text{H}_3\text{O}^+(\text{H}_2\text{O})$ or $\text{H}_3\text{O}^+(\text{H}_2\text{O})_2$.

In this chapter, the measured sensitivity and cluster distributions obtained with the PTR-MS instrument are compared with values predicted by thermodynamic and kinetic data. The goal of this chapter is to explore the application of a theoretical approach based on the kinetics of protonated cluster chemistry to simulate the measured distributions of clusters in the PTR-MS drift tube. In the past, a modeling technique based on equilibrium between the different clusters was used to estimate their distributions; however, these estimates have not accurately predicted measurements made using PTR-MS instruments over a range of drift tube conditions. In order to better predict the cluster distributions in the PTR-MS drift tube,

and to understand why the equilibrium model does not accurately predict measured values, a kinetics model of the PTR-MS drift tube chemistry is presented here. This is the first attempt to use a kinetics model to simulate the ion molecule chemistry in the PTR-MS drift tube. Compared to the equilibrium method, a kinetics method has the advantage of allowing the individual formation and destruction processes to be quantified and probed, permitting deeper understanding of the processes controlling cluster formation and destruction.

The kinetics model also has the capability to simulate the nature of the PTR-MS analytical response as the primary ion signal becomes dominated by $\text{H}_3\text{O}^+(\text{H}_2\text{O})_n$ clusters instead of H_3O^+ . To demonstrate this capability and to verify the results of the kinetics model, the response of benzene, toluene, acetone, and isoprene are compared with measurements made with the PTR-MS in the previous chapter.

3.2 Background:

Previously, the distribution of water clusters within the PTR-MS drift tube was estimated using equilibrium data generated using High Pressure Mass Spectrometry (HPMS).³¹ The work of Lau et al.³¹ presents the thermodynamics, equilibrium constants, and forward rates for reaction for $\text{H}_3\text{O}^+(\text{H}_2\text{O})_{0-7}$ cluster formation. This equilibrium approach has been used to explain the humidity sensitivity displayed by compounds with low proton affinities (like benzene), and to illustrate the effect of E/N on cluster distributions.^{3, 32} However, this approach has consistently failed to accurately reproduce the distribution of hydrated clusters within the PTR-MS drift tube, indicating that existing knowledge of these processes is incomplete.^{11, 32} Warneke et al.³² showed that the equilibrium model predicted substantially more clusters than were measured by the mass analyzer. The difference between model and measurement of clusters was ascribed to breakup in the intermediate vacuum

region. Ion mobility measurements within the same system were used to support the point that ions in the drift tube were in a similar distribution compared to the equilibrium model. Intriguingly, substantially more large clusters ($\text{H}_3\text{O}^+(\text{H}_2\text{O})_3$ and $\text{H}_3\text{O}^+(\text{H}_2\text{O})_4$) were measured than were predicted by the equilibrium model.³² This observation seems counter intuitive, as larger clusters have large collision cross sections, lower formation energies (for the reaction $\text{H}_3\text{O}^+(\text{H}_2\text{O})_{n-1} + \text{H}_2\text{O} \rightarrow \text{H}_3\text{O}^+(\text{H}_2\text{O})_n$), and are therefore most susceptible to breakup. Hanson et al.¹¹ also found that their measured cluster distributions and equilibrium model calculations were not in good agreement. Cluster formation was tested in both a drift tube at 10 mbar and in a special reaction chamber. It was found that the drift tube did not provide enough reaction time to achieve equilibrium between water $\text{H}_3\text{O}^+(\text{H}_2\text{O})_n$ clusters, and that larger voltages were required for effective operation of the declustering region. Several explanations for the differences between the measurements and the model were suggested. One possibility suggested was that the actual reaction temperature is less than the effective temperature of ions moving in the electric field of the drift tube (T_{eff}), as the N_2 buffer gas is rotationally and vibrationally cold while H_3O^+ is moving in an electric field. Another suggestion was that resonant charge transfer might be occurring in collisions between water molecules and the protonated clusters.¹¹

Comparing the equilibrium technique (discussed below, section 3.4.1) and the measurements made under constant drift tube field strength and varying drift tube water pressure presented the last chapter again shows that the equilibrium model does not accurately replicate the measurements made with the PTR-MS (Figure 3-1). The equilibrium model predicts higher levels of H_3O^+ at every water vapor pressure. At higher water vapor pressures, it over predicts the formation of $\text{H}_3\text{O}^+(\text{H}_2\text{O})_3$, and under predicts the amount of $\text{H}_3\text{O}^+(\text{H}_2\text{O})_2$. Under conditions where the field strength of the drift tube is held constant,

and the water vapor pressure of the drift tube is elevated, cluster formation is more favored than the equilibrium model predicts.

The consistent disagreement between the equilibrium model and measurements made by PTR-MS instruments necessitates a different approach to understanding the ion molecule reactions within the drift tube. Here, a method using the kinetics of cluster formation and destruction is presented. This technique provides a greater level of detail in modeling, as the ion cluster distributions are not uniform along the length of the drift tube. The electric fields within the ion source and extraction optics in the skimmer region are much higher ($100\text{-}400\text{ V}\cdot\text{cm}^{-1}$) than in the drift tube ($60\text{ V}\cdot\text{cm}^{-1}$ in our instrument), so the cluster distribution will be dominated by H_3O^+ at the entrance of the drift tube. At this point, the distribution of hydrated clusters is not in equilibrium within the context of the lower field strength of the drift tube. Additionally, H_3O^+ and water vapor are injected into the drift tube at the same point with the sample air stream. Thus, there is more H_3O^+ available at the drift tube entrance than an equilibrium model would predict, and as a result, compounds that would not be protonated by $\text{H}_3\text{O}^+(\text{H}_2\text{O})$ clusters can be protonated by the initially high levels of H_3O^+ at the drift tube entrance. Similarly, if the ion molecule cluster chemistry has not reached steady state by the end of the drift tube, there could be differences between measured values and those determined by an equilibrium model. By using a kinetic determination to model the evolution of protonated clusters within the drift tube, the effects of changing of $\text{H}_3\text{O}^+(\text{H}_2\text{O})_n$ cluster distributions after the drift tube entrance can be explored and different aspects of the cluster formation and destruction pathways can be varied in order to search for likely sources of discrepancy.

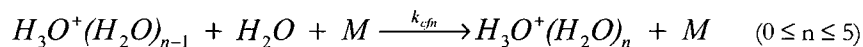
This kinetics based approach is similar to the one that has been used to deconvolute the cluster distributions within select ion flow tube (SIFT) instruments.^{63,64} SIFT instruments

lack the declustering properties provided by the electric field in the PTR-MS drift tube, and instead they use a dry helium buffer gas to prevent the formation of hydrated clusters. This model improves on that method by considering rates of formation and destruction of hydrated clusters, parameterizing the energy of ion-molecule collisions due to the electric field in the drift tube, and estimating ion mobility of hydrated clusters at different E/N levels and drift tube water vapor pressures.

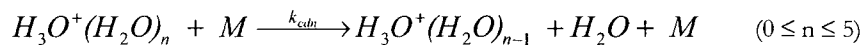
3.3 Development of a Kinetics Model

In order to compare our results with published kinetic and equilibrium data, a kinetics model was constructed to evaluate the chemistry that takes place inside the PTR-MS drift tube. The model has pathways for cluster formation (k_{fm}) and destruction (k_{dm}) (Equation 7 and Equation 8):

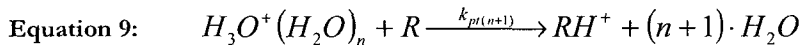
Equation 7:



Equation 8:

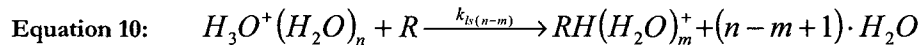


Pathways for proton transfer reactions from H_3O^+ and hydrated proton clusters are also included (rate constant for proton transfer denoted $k_{p(n+r)}$, where n is the number of H_2O molecules in the cluster with

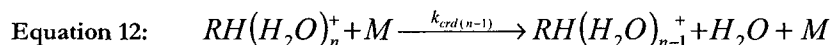
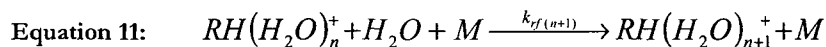


The model also includes ligand switching reactions in which protonated clusters combine with analyte species, sometimes releasing water molecules, resulting in a mixed proton bound cluster containing both the analyte and one or more water molecules (rate constant for

ligand switching is denoted $k_{ls(n-m)}$, where n is the number of H_2O molecules in the cluster with H_3O^+ , and m is the number of water molecules that stay attached to the analyte):



After ionization, it is possible for some protonated compounds to undergo hydration and dehydration reactions. The rate of hydration is denoted $k_{ff(n+1)}$, and the rate of dehydration is ($k_{rd(n-1)}$), where n is the number of water molecules in the parent cluster:



The entire reaction scheme for the kinetics model shown in Figure 3-2.

The work of Lau et al.³¹ was used to calculate the rates of formation and dehydration of protonated clusters. They give experimentally determined thermodynamic parameters (ΔH_n° , ΔS_n°), and forward rate constants for the cluster formation reaction. The equilibrium constant between protonated clusters (K_{eqn} where n is the number of bound water molecules in the product) is calculated from the Gibbs free energy (ΔG_n°):

$$\text{Equation 13: } \Delta G_n^\circ = \Delta H_n^\circ - T \cdot \Delta S_n^\circ$$

$$\text{Equation 14: } K_{eqn} = e^{-\frac{\Delta G_n^\circ}{RT}}$$

where T is the temperature. The equilibrium between water and the various clusters is expressed as:

$$\text{Equation 15: } K_{eqn} = \frac{[H_3O^+(H_2O)_n]}{[H_3O^+(H_2O)_{n-1}][H_2O]}$$

where K_{eqn} is in unites of atm^{-1} . Collision energy between $\text{H}_3\text{O}^+(\text{H}_2\text{O})_{n-1}$ ions and H_2O must be accounted for; this is accomplished by using, the effective temperature (T_{eff}) of the ions moving in the electric field of the drift tube, as described by McFarland et al., in place of T .⁵⁷:

$$\text{Equation 16: } KE_{ion} = \frac{1}{2}mv^2 + \frac{1}{2}M_bv^2 + \frac{3}{2}RT$$

$$\text{Equation 17: } KE_{CM} = \left[\frac{M}{(m+M)} \right] \times \left(KE_{ion} - \frac{3}{2}RT \right) + \frac{3}{2}RT$$

$$\text{Equation 18: } T_{eff} = \frac{2}{3} \times \frac{KE_{CM}}{R}$$

where KE_{ion} is the average kinetic energy of the ions moving in the drift tube in (J mol^{-1}), m is the molar mass of the ion ($\text{kg}\cdot\text{mol}^{-1}$), M_b is the molar mass of the bath gas ($\text{kg}\cdot\text{mol}^{-1}$), R is the ideal gas constant ($8.134 \text{ J}\cdot\text{mol}^{-1}\cdot\text{K}^{-1}$), and T is the temperature of the bath gas (K). The center-of-mass kinetic energy (KE_{CM}), is the average energy ($\text{J}\cdot\text{mole}^{-1}$) exchanged when an ion and a neutral reactant molecule collide. M is the molar mass of the reagent molecule (kg mol^{-1}), and v is the velocity of ions inside the drift tube (m s^{-1}) which is determined from drift velocity (v_d in cm s^{-1}) which is determined from the ion mobility of the ions within the bath gas and the .³

$$\text{Equation 19: } v_d = \mu \times E$$

$$\text{Equation 20: } \mu = \frac{\mu_0 N_0}{N}$$

$$\text{Equation 21: } v_d = \mu_0 N_0 \times \frac{E}{N}$$

The ion drift velocity v_d is equal to the ion mobility (μ) ($\text{cm}^2\cdot\text{V}^{-1}\cdot\text{s}^{-1}$) times the electric field strength (E) ($\text{V}\cdot\text{cm}^{-1}$). The ion mobility is obtained by scaling the reduced ion mobility (μ_0) by the ratio of the number density of molecules at STP (N_0) ($\text{molec}\cdot\text{cm}^{-3}$) to the number density of molecules at the pressure and temperature in the drift tube (N)

(molec·cm³). μ_0 is specific to each ion-bath gas combination, and is also a function of E/N itself. E/N is the ratio of the electric field to the number density of molecules, the unit of which is the townsend (Td, 10⁻¹⁷·V·cm²). Ion mobility values were chosen for an E/N of 130 Td. Blanc's law (Equation 22) is used to estimate the ion mobility in the air and water bath gas in the drift tube using published values obtained under pure nitrogen and water vapor. μ_0 for H₃O⁺, H₃O⁺(H₂O), and H₃O⁺(H₂O)₂ in N₂ has been experimentally determined to be 2.76, 2.28, and 2.13 cm²·V⁻¹·s⁻¹, respectively. A value of 2.00 cm²·V⁻¹·s⁻¹ was used for H₃O⁺(H₂O)₃ following Warneke et al.³², and a mobility of 1.70 cm²·V⁻¹·s⁻¹ was assigned to H₃O⁺(H₂O)₄ using the mobility of NO⁺(CH₃CN)₂ as a convenient proxy.⁶⁵ The mobility of the larger clusters is not relevant to this study, as they are not present in the drift tube in significant quantities, and are included only for completeness. The ion mobility of each compound is corrected for the proportion of water vapor in the drift tube. Since water vapor reacts with all of the clusters in competitive hydration and dehydration reactions, the reduced ion mobility for all clusters in pure water vapor is the same value, 0.70 cm²·V⁻¹·s⁻¹.⁶⁶ As mentioned above, the mobility of ions in neat N₂ and H₂O are combined to estimate their mobility in the drift tube using Blanc's law:⁶⁵

Equation 22:
$$\frac{1}{\mu_{mix}} = \frac{x_{N_2}}{\mu_{N_2}} + \frac{x_{H_2O}}{\mu_{H_2O}}$$

where x_{N_2} is the mole fraction of air in the drift tube and x_{H_2O} is the mole fraction of water in the drift tube. Using Equation 21 to calculate the drift velocity, the length of the drift tube, the average time ions spend inside the drift tube is calculated, allowing the simulation of the evolution of cluster distributions within a drift tube of a given length.

The third order forward rate constants for protonated cluster formation (Equation 12) are given by:³¹

Equation 23: $k_{cfn} = aT_{eff}^{-b}$

Where k_{cfn} is the third order rate of formation ($\text{molec}^{-2} \cdot \text{cm}^6 \cdot \text{s}^{-1}$) of protonated water clusters, n is the number of H_2O molecules bound to H_3O^+ , and a and b are fit parameters. The rate constant for the reverse reaction is then derived from the forward reaction rate coefficient and the equilibrium constant, assuming microscopic reversibility:

Equation 24: $K_{eqn} = \frac{k_{cfn}}{k_{cdn}}$

Equation 25: $k_{cdn} = \frac{k_{cfn}}{K_{eq} \cdot R \cdot T}$

where k_{cdn} is the second order rate constant for dissociation, and R is the number ideal gas constant ($1.36 \times 10^{-22} \text{ cm}^3 \cdot \text{atm} \cdot \text{molec}^{-1} \cdot \text{K}^{-1}$), and T is the temperature of the drift tube in Kelvin. The combination of forward and back reactions results in a system of equations that describes five forward cluster formation reactions and five cluster dissociation reactions. The thermodynamic values used to determine equilibrium and the fit constants used to estimate the forward rate constants are listed in Table 3-1.

Under the conditions in the PTR-MS drift tube, each $\text{H}_3\text{O}^+(\text{H}_2\text{O})_n$ ion has its own T_{eff} as each cluster has its own unique μ_0 . This is in contrast to the single temperature conditions of the HPMS in which the forward rate constants (k_{cfn}) and equilibrium constants (K_{eqn}) were obtained.^{31, 67, 68} As a result the product ions will have a different T_{eff} than the reactant ions in the drift tube electric field. A two temperature approach is used to account for the different effective temperature for each ion: k_{cfn} and k_{cdn} are determined from the T_{eff} of the reagent ions. This means that k_{cdn} is determined by calculating the equilibrium constant (K_{eqn}) and the forward rate constant (k_{cfn}) at the effective temperature of the cluster that is to be dissociated ($\text{H}_3\text{O}^+(\text{H}_2\text{O})_n$), instead of using the effective temperature of the original

parent cluster $(\text{H}_3\text{O}^+(\text{H}_2\text{O})_{n-1})$. For example, $k_{eff}(\text{H}_3\text{O}^+ + \text{H}_2\text{O} + \text{M} \rightarrow \text{H}_3\text{O}^+(\text{H}_2\text{O}) + \text{M})$ is calculated using the effective temperature of H_3O^+ , but k_{eff} occurs at the effective temperature of $\text{H}_3\text{O}^+(\text{H}_2\text{O})$, so k_{eff} (for $\text{H}_3\text{O}^+(\text{H}_2\text{O}) + \text{M} \rightarrow \text{H}_3\text{O}^+ + \text{H}_2\text{O} + \text{M}$) and K_{eq} are recalculated at the effective temperature of $\text{H}_3\text{O}^+(\text{H}_2\text{O})$ to determine k_{eff} .

At present, it is not possible to directly simulate the hydration and dehydration of the reactants due to the limited kinetic data available in the literature. This may not be significant in this case, as the high PTR-MS drift tube field strength is very efficient at preventing formation of complex clusters. Additionally, it has been noted that mixed cluster formation is suppressed in gas measurement systems operating at 450 K, far colder than the system modeled here.⁶⁹ Given this, the absence of appropriate kinetic data, and the intent of this work to examine the chemistry with respect to PTR-MS measurements, all mixed clusters formed in the model are assumed to ultimately form the protonated analyte, (RH^+) . In the case of high pressures of water, this is probably an oversimplification as the smaller ion mobility will lower the T_{eff} of the clusters significantly, and the higher pressure of water will make formation of hydrated clusters more favorable.

To make the modeling results comparable to those measured by the PTR-MS, the predicted ion number densities (S_i) are scaled by the transmission curve provided by Ionicon for our PTR-MS instrument (Figure 3-3).

Equation 26:
$$s_f = E_{trans} \cdot S_i$$

The final number density (s_f) of an ion is equal to the relative transmission efficiency for that ion (E_{trans}) times the number density at the end of the drift tube.

In order to correctly simulate the ion cluster chemistry, the results of the kinetics simulation must be converted into the context of the drift tube, which has a specified distance over which the reactions occur. In order to retrieve ion distributions at the correct

point in the time based simulation, representing ions reaching the end of a drift tube, the average velocity of ions is determined from the ion mobilities and the relative distribution of the different clusters within the drift tube. To estimate the average time it takes for ions to exit the drift tube, the average reduced ion mobility for all ions ($\bar{\mu}_{0_step}$), weighted by the fraction of each ion present ($f_{H_3O^+(H_2O)_n}$) is calculated for each time step of the simulation:

$$\text{Equation 27: } \bar{\mu}_{0_step} = \sum_{n=0}^{n=4} f_{H_3O^+(H_2O)_n} \cdot \mu_{0_H_3O^+(H_2O)_n}$$

The overall average reduced ion mobility for throughout the simulation is then calculated reduced ion mobility values obtained in Equation 28:

$$\text{Equation 28: } \bar{\mu}_0 = \frac{\sum_{t=0}^{t=1000\mu s} \bar{\mu}_{0_step}}{1000\mu s}$$

The average velocity of ions in the drift tube is then calculated using Equation 21. The reaction time (τ) is then determined from the drift velocity (v_d) divided by the length of the drift tube (10 cm):

$$\text{Equation 29: } \tau = \frac{10cm}{v_d}$$

The system of chemical reactions, and algorithms to calculate the rate and equilibrium constants, effective temperature, and travel time in the drift tube was implemented using Igor Pro 5.0.5.7 (Wavemetrics, Inc.). The system was integrated using the fifth-order Runge-Kutta-Fehlberg algorithm included with the package.

3.4 Model Testing

A set of 30 test cases based on the experimental conditions were devised to compare the new kinetics model, the equilibrium model, and the measured results. These initial

conditions are summarized in Table 3-2. Runs 0-22 encompass the range of water pressures measured in the experiment, while runs 23-29 are purely theoretical. Runs 0-10 examine the effect of humidity on cluster distributions by simulating the pressure of water at RH from 0 to 100% at 25°C. Runs 11-23 use the calculated water pressures in the PTR-MS drift tube during the optimization experiment. Runs 24-29 are 0.1 mbar increases in water pressure up to 1 mbar. For all runs, the initial number density of H_3O^+ was $5.13 \times 10^{10} \text{ cm}^{-3}$, and the initial number density of R was 1 part-per-billion of the number density of the bath gas $(4.55\text{-}2.27) \times 10^7 \text{ cm}^{-3}$. Additionally, the temperature of the neutrals inside the drift tube was 45°C, the total pressure was 2 mbar, the field strength was $60 \text{ V}\cdot\text{cm}^{-1}$, and the length was 10 cm, yielding a E/N of 132 Td.

An example of predicted evolution of clusters by the kinetics model (from Equation 15, 17, and 19) is given in Figure 3-5. This shows that the reactions between the various clusters reach steady state on the order of the time an ion is in the drift tube at $60 \text{ V}\cdot\text{cm}^{-1}$. The vertical black lines depict the reaction along with the reaction time in μs to illustrate where ion distributions are extracted from the model to simulate travel along the length of a 10 cm drift tube.

3.4.1 Comparison of the Kinetics and Equilibrium Models

The kinetics model is compared to the equilibrium model (from Equation 15, 17, and 19) in Figure 3-6, showing both models run with the same input data. The equilibrium method for determining cluster distributions predicts that the $\text{H}_3\text{O}^+(\text{H}_2\text{O})_n$ clusters are predominant at larger pressures of water in the drift tube than does the kinetics method. This difference suggests that production of protonated clusters is disfavored in the equilibrium model compared to the kinetic model. The disparity is most apparent for H_3O^+

and $\text{H}_3\text{O}^+(\text{H}_2\text{O})$, and better agreement is obtained for $\text{H}_3\text{O}^+(\text{H}_2\text{O})_2$. The results for the two modeling methods are offset by about 0.05 mbar H_2O at low water pressures. The difference narrows as water becomes more prevalent in the system, indicating that the disparity between the models is smaller for larger clusters.

In order to test the sensitivity of the model to uncertainty in the rate constants, tests runs were carried out by varying the rate constants by a factor of 2 lower than and higher than the calculated value. This value was chosen so as to encompass the observed difference between the rate constants obtained from Equation 23 and the individual rate constants given in Lau et al.³¹ The results of this study are shown in Figure 3-7, showing that the kinetics is more sensitive to increasing the rate coefficients of reaction than to decreasing them.

3.5 Comparison of PTR-MS and Model Cluster Distributions

Comparing model results to the experimental data (Figure 3-8) reveals that instrumental results do not agree very well with either model, for most ions, particularly at water pressures greater than 0.2 mbar. The best agreement is with the kinetic model; the fraction of H_3O^+ (m19) in the drift tube is closely reflected at all pressures, and the fraction $\text{H}_3\text{O}^+(\text{H}_2\text{O})$ (m37) has good agreement until a water pressure of 0.2 mbar, where the model predicts that more $\text{H}_3\text{O}^+(\text{H}_2\text{O})$ is produced, while measurements show the fraction of $\text{H}_3\text{O}^+(\text{H}_2\text{O})$ decreasing and the proportion of $\text{H}_3\text{O}^+(\text{H}_2\text{O})_2$ increasing. The large increase in measured $\text{H}_3\text{O}^+(\text{H}_2\text{O})_2$ suggests that there is a greater affinity for cluster formation inside the PTR-MS drift tube than the equilibrium model predicts. In order to narrow down the possible sources of the disagreement between the model and measurement, several possible

parameters were investigated: collision induced dissociation (CID), changing the reaction temperature (T_{eff}), and changing the rates of interconversion between different clusters.

In order to eliminate the possibility of cluster CID in the intermediate vacuum region causing the observed trends, CID was simulated using data for collision cross sections of proton bound water clusters in both argon and xenon.^{70, 71} However, under the range of possible pressures in that region, this only increased the disparity between the calculations and the measurements; the calculated CID at high collision gas pressures causes large increases in the fraction of H_3O^+ , while at low pressures the impact of CID on the cluster distribution is negligible compared to the measurements shown here.^{70, 71}

It has been suggested that the effective temperature of the protonated clusters in the drift tube might be lower than predicted by the Wannier expression.¹¹ Figure 3-9 (a-b) shows the effect of scaling T_{eff} to (a) 80% and (b) 50% of its estimated value. The possibility that the reaction temperature was lower than T_{eff} was explored by scaling T_{eff} for all species. The resulting moderate reduction of T_{eff} provides a somewhat better fit to measured cluster distributions, as the equilibrium shifted towards cluster formation. However, it was not possible to provide an exact fit using this method alone. Further lowering T_{eff} results in the fraction of H_3O^+ being under predicted while $H_3O^+(H_2O)_n$ clusters are over-predicted. This may partially explain the larger fractions of $H_3O^+(H_2O)$ and $H_3O^+(H_2O)_n$, but other factors would also have to be active within the drift tube environment.

Artificially lowering the ΔH° of the first cluster by an additional $\approx 0-60 \text{ kJ}\cdot\text{mol}^{-1}$ has a similar result to scaling T_{eff} . However, the fraction of $H_3O^+(H_2O)$ cannot be made to closely match the experimental results in this manner, as the rate of association ultimately becomes limiting. The thermodynamic data for the reaction system appears to be well quantified, so while testing various inputs to the equilibrium method is illustrative of potential explanation

of the PTR-MS measurements, it is unlikely that the published thermodynamic data is incorrect.^{31, 67, 68, 71}

A more detailed sensitivity study was conducted to fit the model to the observed experimental data. Each rate constant was systematically increased and decreased to understand the effect on the reaction system FIGURE 3-10 (a-e). For the conditions where the PTR-MS measurements were made, $k_{gf(1..2)}$ and $k_{gd(1..2)}$ are the rate constants that have dominant control on the model output. By changing individual values of k_{gf} and k_{gd} it is possible to change the various cluster distributions. In particular, it was found that increasing the rate constant of formation of $\text{H}_3\text{O}^+(\text{H}_2\text{O})_2$ (k_{g2} , Figure 3-2) brought the kinetic system into closer agreement with the measurements [FIGURE 3-10 (c)]. Further increasing k_{g2} by a factor of 200 drastically improved the fit of the kinetic model to the PTR-MS measurements (Figure 3-11). This is, in effect, increasing k_{g2} to several times the value of k_{gf} (~ 15 times greater at 0.20 mbar H_2O). Assuming that the system is near the high pressure limit, this yields a pseudo-second order rate constant in the range of $\sim 10^{-11} \text{ cm}^3 \cdot \text{molec}^{-1} \cdot \text{sec}^{-1}$ at 0.20 mbar, increasing with water pressure.

In order to test the fit results for E/N dependence, they were compared to results from measurements made at constant water pressure and varying E/N. de Gouw et al.³ present measurements of cluster formation over a range of drift tube voltages at 2.4 mbar, 25% relative humidity, and 298.15 K. The unmodified model (Figure 3-13) shows similar results to their measurements for H_3O^+ and $\text{H}_3\text{O}^+(\text{H}_2\text{O})_1$, though the agreement for larger clusters is poor. The modified kinetic scheme (Figure 3-14) does not match the measured cluster distributions very well, although it does predict $\text{H}_3\text{O}^+(\text{H}_2\text{O})_2$ clusters at higher voltages than does the equilibrium model and unmodified kinetic model do. These results

indicate that the factors controlling the fit obtained at 130 Td are likely to be E/N dependent.

The disparity between the measurements and unmodified model outputs is intriguing, and highlights a lack of knowledge about the chemistry of protonated clusters under the conditions of the drift tube. The improved fit of the kinetic model to our data by increasing the rate of conversion of $\text{H}_3\text{O}^+(\text{H}_2\text{O})$ to $\text{H}_3\text{O}^+(\text{H}_2\text{O})_2$ (via k_{g2}) could be construed several ways. First, other reactions are acting to form $\text{H}_3\text{O}^+(\text{H}_2\text{O})$; it is possible that a three body reaction between H_3O^+ and two H_2O molecules to form $\text{H}_3\text{O}^+(\text{H}_2\text{O})_2$ could explain the observations. It is also possible that extrapolating the temperature dependence of the rate constant (Equation 23) using T_{eff} under the conditions of the drift tube may not be a valid extrapolation or the rate constants for the reactions may need to be better parameterized. The fact that the modified kinetic scheme does not seem to reproduce well the measurements of cluster formation as a function of field strength may signify that there are other ion molecule processes present. The deficiency between theory and measurements should be addressed in order to develop a complete understanding of the chemistry that occurs in the PTR-MS drift tube. From the kinetics standpoint of the system, having rate constants and branching ratios for temperatures over 1400K (greater than the T_{eff} of H_3O^+ at 132 Td) in air would be ideal. These values might be obtainable using the high temperature flowing afterglow technique.⁷²

3.6 Comparison of Predicted and Measured Instrument Response

After exploration of the models ability to simulate cluster formation in the PTR-MS drift tube, kinetic data from the analytes in our standard cylinder were put into the model and the theoretical cluster normalized response to each compound (cneps/ppbv) was

determined. The cluster normalized response was estimated by taking the ratio of the number concentration of the protonated analyte per ppbv of starting material ($x_{RH^+} \cdot \text{ppbv}^{-1}$) to the sum of the first three protonated clusters ($x_{H_3O^+}$, $x_{H_3O^+(H_2O)}$, and $x_{H_3O^+(H_2O)_2}$), and then normalizing to 10^6 $H_3O^+(H_2O)_n$ ($n=0\dots2$) clusters:

$$\text{Equation 30: } \frac{cncps}{ppbv} = \frac{x_{RH^+}}{ppbv} \cdot \frac{10^6}{x_{H_3O^+} + x_{H_3O^+(H_2O)} + x_{H_3O^+(H_2O)_2}}$$

The relative theoretical cluster normalized response was compared to the relative measured cluster normalized response (from Chapter 2) to estimate the ability of the model to predict the values obtained with the PTR-MS. The relative response at different cluster distributions is compared to the maximum response, which gives an idea of how the model captures the observed trends in response observed within the PTR-MS.

For each compound, the model was run without modification and with k_{f2} increased by 200 as discussed above. For all analyte compounds, the initial mixing ratio was modeled to be 1 ppbv, a mixing ratio that is conceivable for many compounds that are both present in the atmosphere and detectable with the PTR-MS.

3.6.1 Benzene and Toluene

Benzene and toluene were examined first as their ionization pathway in the PTR-MS is the simplest. They only react with H_3O^+ because their proton affinity is sufficiently low that they cannot undergo proton transfer with any $H_3O^+(H_2O)_n$ clusters. The rate constant used (k_{r1}) for benzene was $1.9 \times 10^{-9} \text{ molec}^{-1} \cdot \text{cm}^3 \cdot \text{s}^{-1}$, and rate constant used for toluene was $2.2 \times 10^{-9} \text{ molec}^{-1} \cdot \text{cm}^3 \cdot \text{s}^{-1}$.⁷³ The results of these calculations are shown in Figure 3-15 (a) for benzene and Figure 3-15 (b) for toluene. For both compounds, there is good agreement between the models and instrument at low cluster fractions, but both versions of the model

slightly over predict the relative response, with benzene having a more pronounced difference between model and measurements. There is very little difference between the standard and modified model results for these compounds, as the only source of protonation for these compounds is H_3O^+ , which is not significantly affected by increasing $k_{\text{eff}2}$.

3.6.2 Isoprene and Acetone

The chemistry for isoprene and acetone is more complex than that of benzene and toluene and requires additional consideration. Isoprene can be protonated by $\text{H}_3\text{O}^+(\text{H}_2\text{O})$, while acetone can also be ionized by $\text{H}_3\text{O}^+(\text{H}_2\text{O})$ and $\text{H}_3\text{O}^+(\text{H}_2\text{O})_2$ to form a mix of protonated acetone and proton bound clusters of acetone and water.⁷⁴ The rate constant for the reaction of isoprene with H_3O^+ ($k_{\text{p}11}$) is $2.0 \times 10^{-9} \text{ molec}^{-1} \cdot \text{cm}^3 \cdot \text{s}^{-1}$, and the rate constant for its reaction with $\text{H}_3\text{O}^+(\text{H}_2\text{O})$ ($k_{\text{p}12}$) is $1.8 \times 10^{-9} \text{ molec}^{-1} \cdot \text{cm}^3 \cdot \text{s}^{-1}$.⁷⁴ The results of the calculation with isoprene is shown in Figure 3-15 (c). The addition of the second source of proton transfer keeps the response to isoprene fairly uniform when plotted against the fraction of clusters, as response only decreases when $\text{H}_3\text{O}^+(\text{H}_2\text{O})_2$ becomes more dominant than $\text{H}_3\text{O}^+(\text{H}_2\text{O})$. The unmodified model and modified model produce very similar results for isoprene under low cluster conditions, as they both produce similar distributions of H_3O^+ and $\text{H}_3\text{O}^+(\text{H}_2\text{O})$. At higher cluster fractions, the modified model shifts the population of hydrated clusters to $\text{H}_3\text{O}^+(\text{H}_2\text{O})_2$ more than the unmodified version, which results in a decrease in predicted response to isoprene. Thus, the modified model does a better job of capturing the measured response of isoprene, as the unmodified model shows a much steeper drop in response that occurs well after the measured response drops.

Acetone features the most complex chemistry considered in this model. Acetone can undergo direct proton transfer with H_3O^+ and $\text{H}_3\text{O}^+(\text{H}_2\text{O})$ ($k_{\text{p}11}$ of 4.1×10^{-9} , $k_{\text{p}12}$ of 1.16×10^{-9}

molec⁻¹·cm³·s⁻¹). It can also undergo ligand switching reactions with H₃O⁺(H₂O)_n (1 ≤ n ≤ 3) ($k_{k1-1}=2.15\times 10^{-9}$, $k_{k2-2}=2.45\times 10^{-9}$, $k_{k2-1}=5\times 10^{-11}$, $k_{k3-3}=2.35\times 10^{-9}$, $k_{k3-2}=4.8\times 10^{-11}$ molec⁻¹·cm³·s⁻¹).⁷⁴ The model results for acetone are shown in Figure 3-15 (d). Because there are so many pathways for protonation of acetone, it displays a response at most cluster fractions. The modeled and measured results are very similar for this compound. At high cluster fractions, the modified model predicts lower relative response than the unmodified version.

3.7 Conclusions

By using a kinetics model to simulate the cluster formation and destruction reactions within the PTR-MS drift tube, it is possible to reproduce several characteristics of the PTR-MS instrument, including cluster distributions changing with drift tube humidity and decreasing sensitivity as H₃O⁺ is converted into H₃O⁺(H₂O)_n clusters. The kinetic model shows that the protonated cluster distributions along the length of the drift tube are not in steady state, so that H₃O⁺ is present in higher number densities at the beginning of the drift tube than at the end, after it has undergone cluster formation with water vapor in the ambient air and from the ion source. The kinetics model also highlights the gaps in the available kinetic data for cluster chemistry, as the kinetics model does not give the same cluster fractions as the equilibrium model that uses a single T_{eff} . Additionally, neither the kinetics nor the equilibrium model can reproduce the measurements of clusters made with the PTR-MS. By increasing the rate constant for formation of H₃O⁺(H₂O)₂ from H₃O⁺(H₂O), the kinetics model could be made to more accurately reproduce the measured results in situations where high water vapor pressures are present in the PTR-MS drift tube.

This modification does not improve the agreement when the model output is compared to measurements made across a range of E/N ratios.

Overall, the kinetics model does a fair job of predicting the relative trends in response of the PTR-MS instrument over a range of drift tube water pressures. Cluster normalized responses can also be produced using this technique. However, the uncertainty in our experimental data is very large; thus it is difficult to draw solid conclusions about the accuracy of the technique. It appears that the model results for relative cluster normalized response are more accurate when the rate of $\text{H}_3\text{O}^+(\text{H}_2\text{O})$ to $\text{H}_3\text{O}^+(\text{H}_2\text{O})$ conversion is increased to fit the modeled cluster distributions. In particular, the improved model results for isoprene are much more similar to those measured with the PTR-MS, indicating that the improved model really does reflect cluster distributions in the drift tube, and the observed distributions are not a product of some instrumental fault.

Ultimately, the ability to model the cluster formation, proton transfer, and ligand switching reactions in the PTR-MS drift tube is limited by the availability of kinetic data. In order to capture typical conditions in the PTR-MS, namely high temperatures, in the presence of N_2 or air as a bath gas, and with water vapor present. By determining these values, it should be possible to better predict instrumental efficiency and improve instrument designs, so that real instruments perform exactly as designed.

3.8 Figures and Tables

Table 3-1. The values from Lau et al.³¹ for the thermodynamics and forward kinetics of the $\text{H}_3\text{O}^+(\text{H}_2\text{O})_n$ - $\text{H}_2\text{O}+\text{M}\rightleftharpoons\text{H}_3\text{O}^+(\text{H}_2\text{O})_n+\text{M}$ system. The values of a and b are parameters for Equation 23 ($k_{gr} = a \cdot T^{-b}$), giving a third order rate constant with units of $\text{molec}^{-2} \cdot \text{cm}^6 \cdot \text{sec}^{-1}$.

n	ΔH° ($\text{kJ} \cdot \text{mol}^{-1}$)	ΔS° ($\text{J} \cdot \text{K}^{-1} \cdot \text{mol}^{-1}$)	a	b
1	-132.30	-101.74	3.70×10^{-17}	4
2	-81.64	-90.85	4.10×10^{-8}	7.5
3	-74.94	-118.90	4.20×10^{-7}	8.1
4	-53.17	-97.97	2.20×10^7	14
5	-48.57	-104.67	4.60×10^9	15.3

Table 3-2. Test conditions to compare the kinetics and equilibrium models and measurement made using the PTR-MS. Runs 0-10 represent the partial pressures of water at 20°C, runs 11-23 represent calculated water pressures during the measurements, and runs 23-29 are completely theoretical. †Run 0 was made with 100 molec·cm⁻³ of H₂O present to increase the speed of integration. This miniscule amount of water had no meaningful bearing on this calculation.

Run	RH @ 20°C	P _{Drift} (mbar)	H ₂ O (mbar)	H ₂ O Molec·cm ⁻³ ·10 ¹⁴	Air Molec·cm ⁻³ ·10 ¹⁴
0	0	2.00	0.000	0.0 [†]	455.2
1	10	2.00	0.006	1.3	453.9
2	20	2.00	0.011	2.5	452.6
3	30	2.00	0.017	3.8	451.4
4	40	2.00	0.022	5.1	450.1
5	50	2.00	0.028	6.3	448.8
6	60	2.00	0.033	7.6	447.6
7	70	2.00	0.039	8.9	446.3
8	80	2.00	0.045	10.1	445.0
9	90	2.00	0.050	11.4	443.7
10	100	2.00	0.056	12.7	442.5
11		2.00	0.043	9.8	445.4
12		2.00	0.070	15.9	439.3
13		2.00	0.097	22.0	433.2
14		2.00	0.123	28.1	427.1
15		2.00	0.150	34.2	421.0
16		2.00	0.177	40.3	414.9
17		2.00	0.204	46.4	408.8
18		2.00	0.231	52.5	402.7
19		2.00	0.257	58.6	396.6
20		2.00	0.284	64.7	390.5
21		2.00	0.311	70.8	384.4
22		2.00	0.338	76.9	378.3
23		2.00	0.400	91.0	364.1
24		2.00	0.500	113.8	341.4
25		2.00	0.600	136.5	318.6
26		2.00	0.700	159.3	295.9
27		2.00	0.800	182.1	273.1
28		2.00	0.900	204.8	250.3
29		2.00	1.000	227.6	227.6

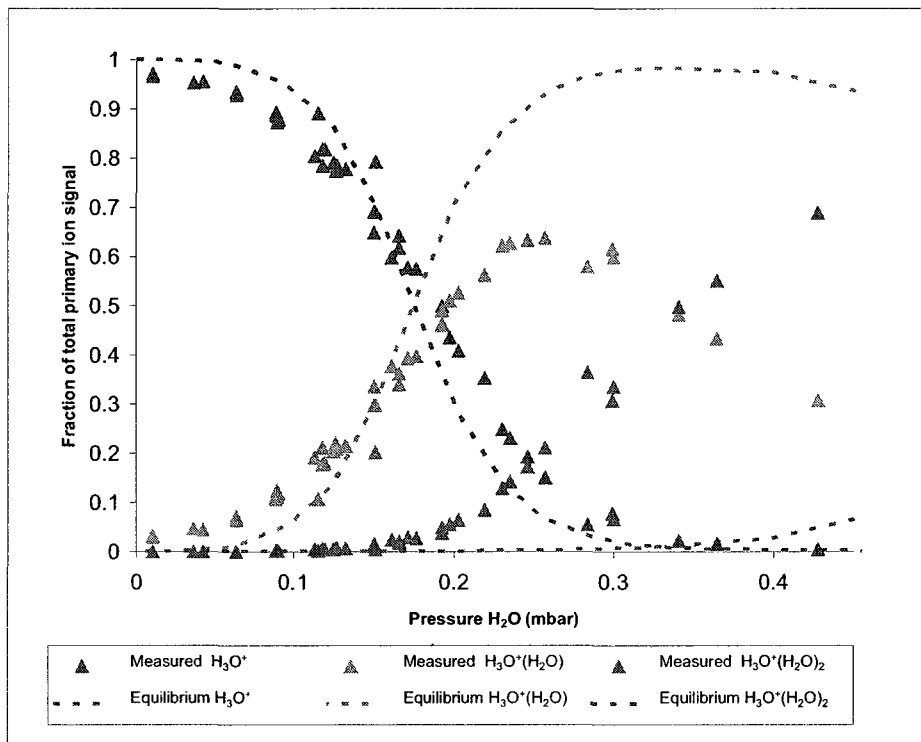


Figure 3-1. The equilibrium model (dashed lines) does not reproduce cluster distributions observed in the PTR-MS drift tube (triangles). The equilibrium model over predicts H₃O⁺ (red) levels at low water pressures, and at pressures over 0.2 mbar, over predicts H₃O⁺(H₂O) (green), and does not predict significant quantities of H₃O⁺(H₂O)₂ (blue) that are observed in the PTR-MS drift tube.

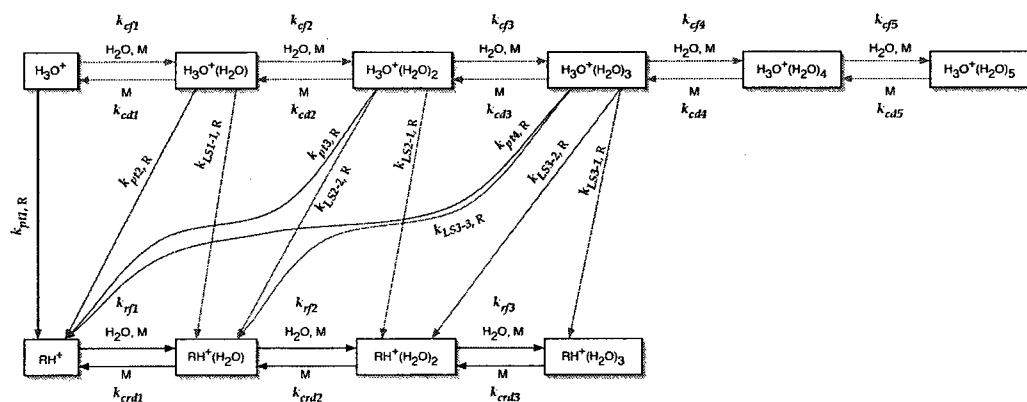


Figure 3-2. The reaction pathways simulated by the kinetics model. The model features formation and destruction pathways for protonated complexes (blue arrows), proton transfer reactions (brown arrows), ligand switching reactions (green arrows), and hydration/dehydration reactions of products (black arrows).

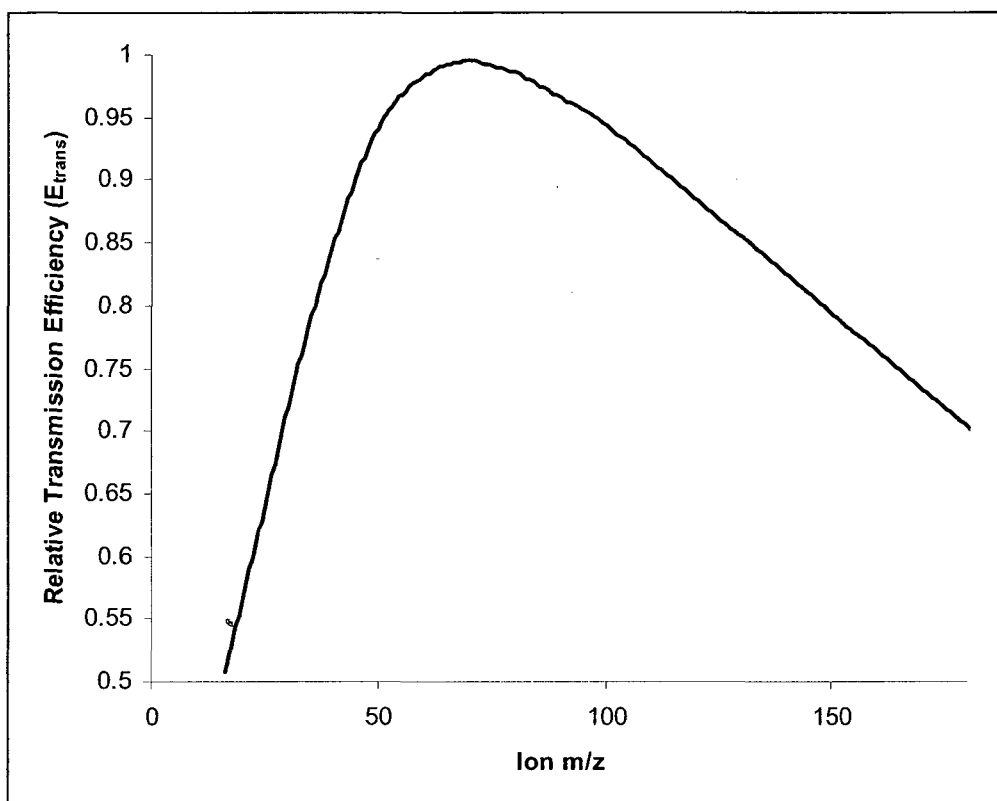


Figure 3-3. The relative transmission efficiency (E_{trans}) as a function of an ions mass-to-charge ratio within a PTR-MS instrument. E_{trans} is used to scale the predicted ion molecule distributions so that results are comparable with PTR-MS measurements. This transmission curve was supplied with a PTR-MS instrument.

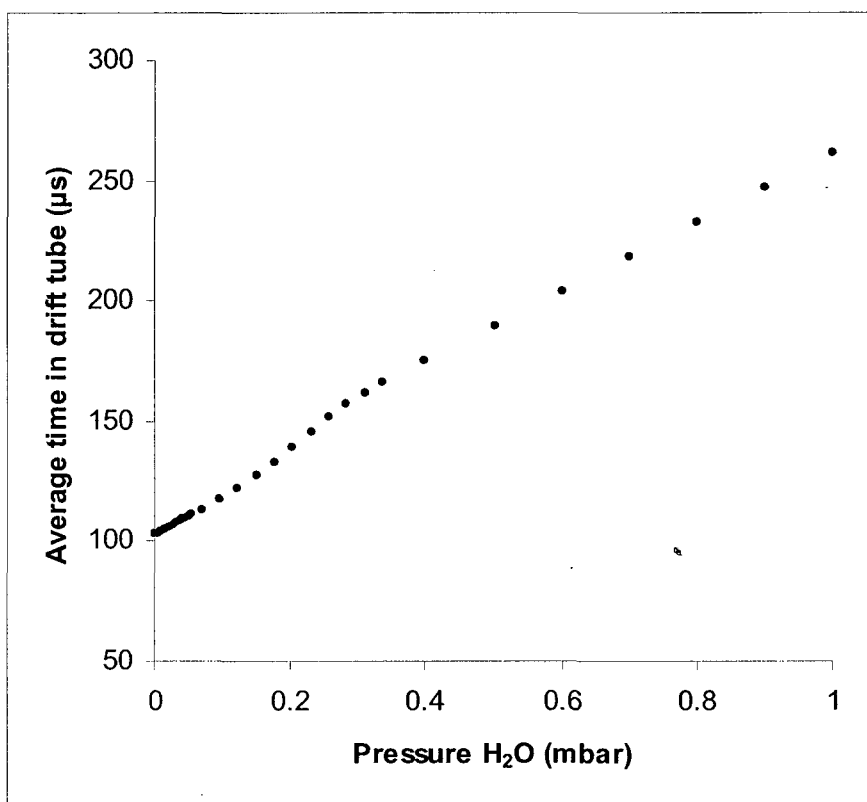


Figure 3-4. The average time it takes for an ensemble of protonated water clusters to traverse a 10 cm drift tube. Conditions in the drift tube are 2 mbar total pressure, 45°C, and 60V·cm⁻¹

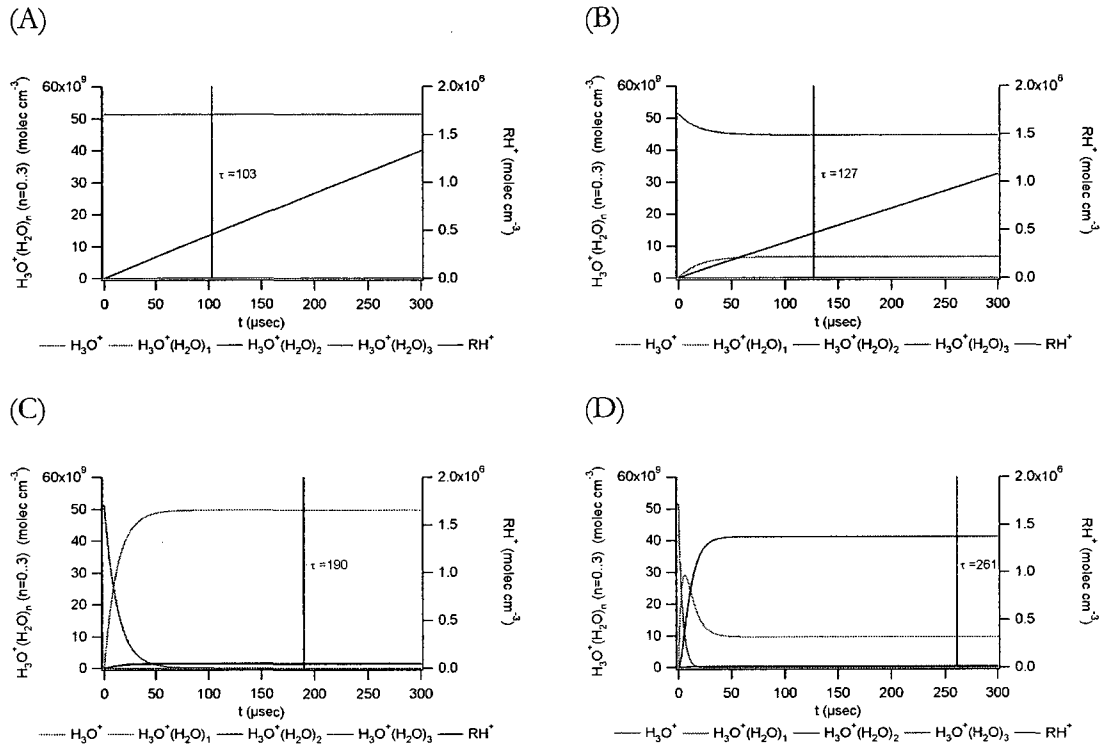


Figure 3-5. Kinetics model results for (a) 10% relative humidity (at 293K), and water vapor pressures of 0.15 (b), 0.50 (c) and (d) 1.00 mbar in the drift tube, with a total drift tube pressure of 2mbar and 60V cm^{-1} field strength. The vertical line indicates the average time it takes for an ion to travel the length of a 10 cm drift tube.

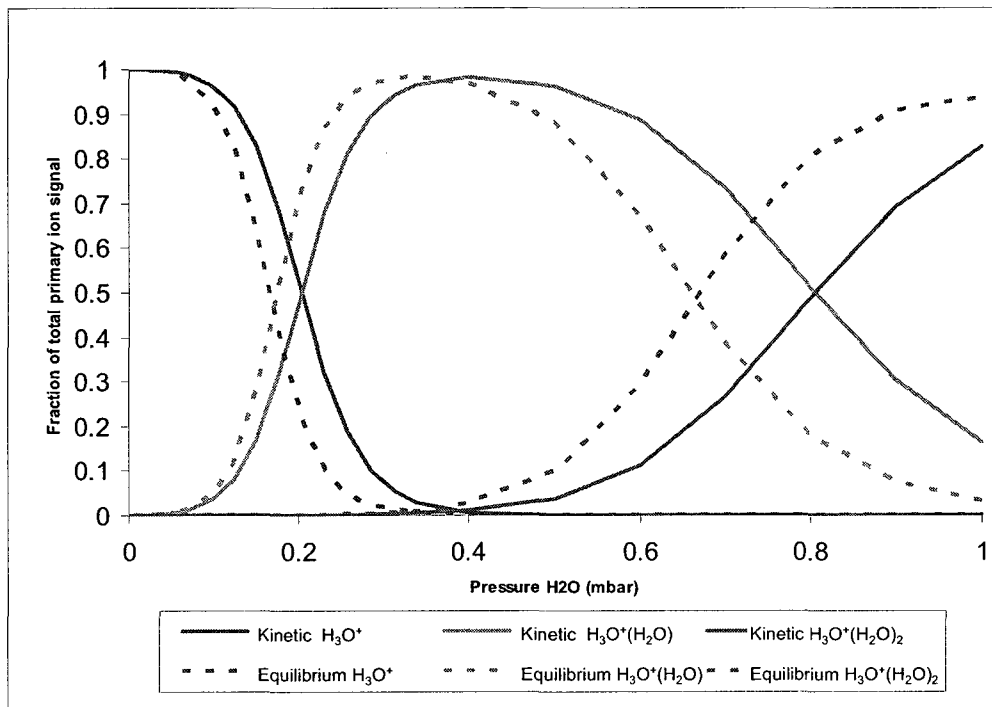


Figure 3-6. Kinetics and equilibrium models of cluster distributions at different water pressures in the drift tube.

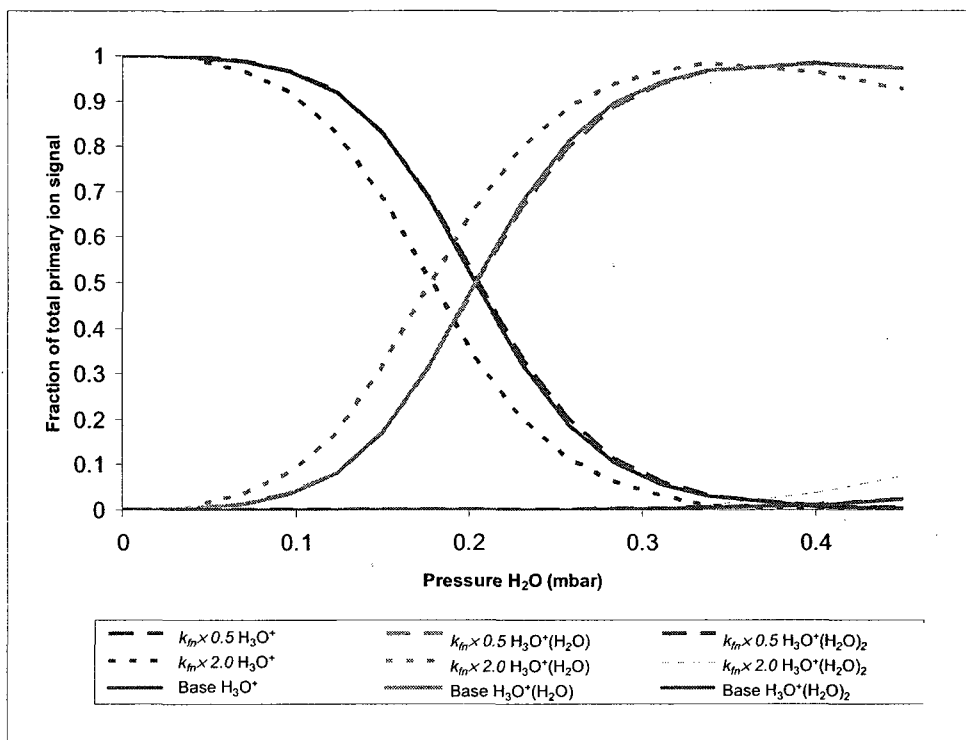


Figure 3-7. The results of model sensitivity study to illustrate the effect of the uncertainty of the kinetic constants, where the rate coefficients of the forward reactions are doubled and halved.

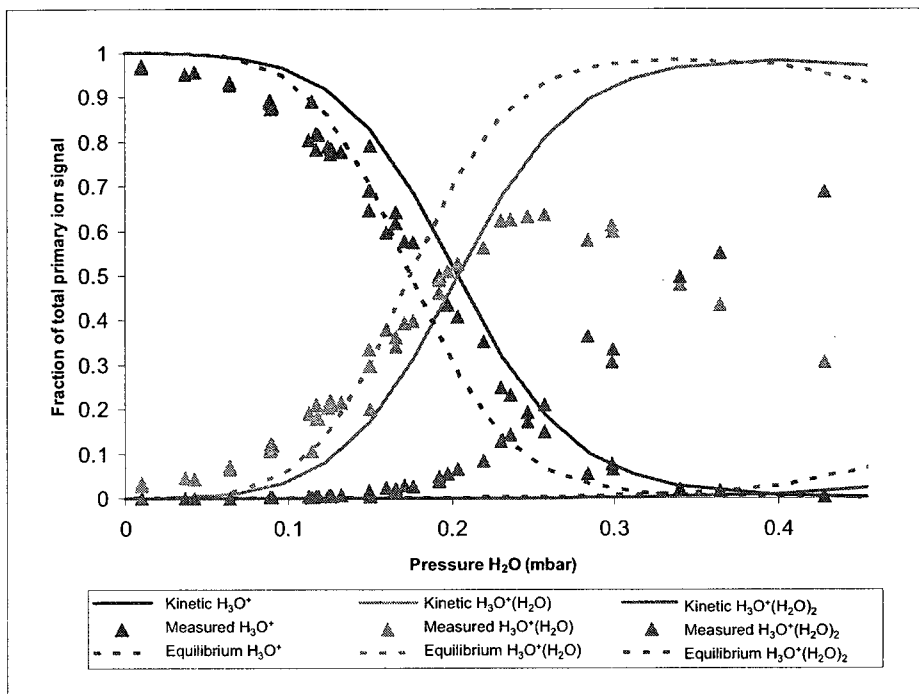
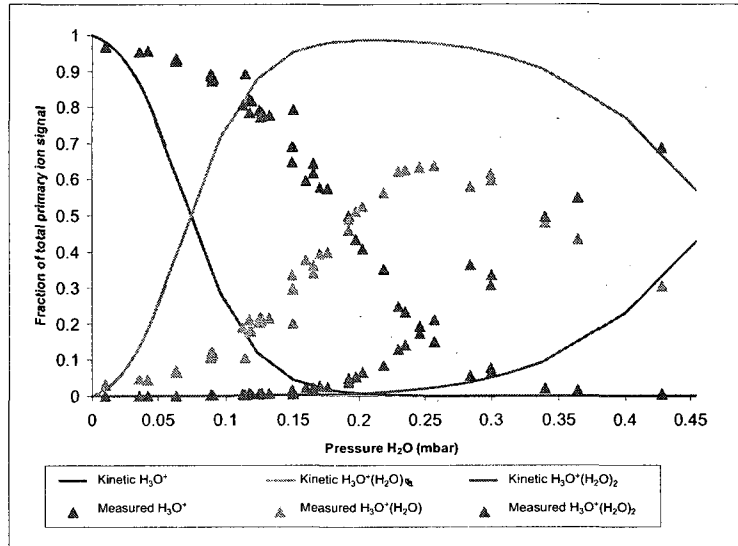


Figure 3-8. A comparison between humidity dependent cluster distributions measured in the PTR-MS and cluster distributions predicted by the kinetics and equilibrium models. Both models over predict relative proportion of clusters measured by the PTR-MS, particularly at higher water pressures.

(A)



(B)

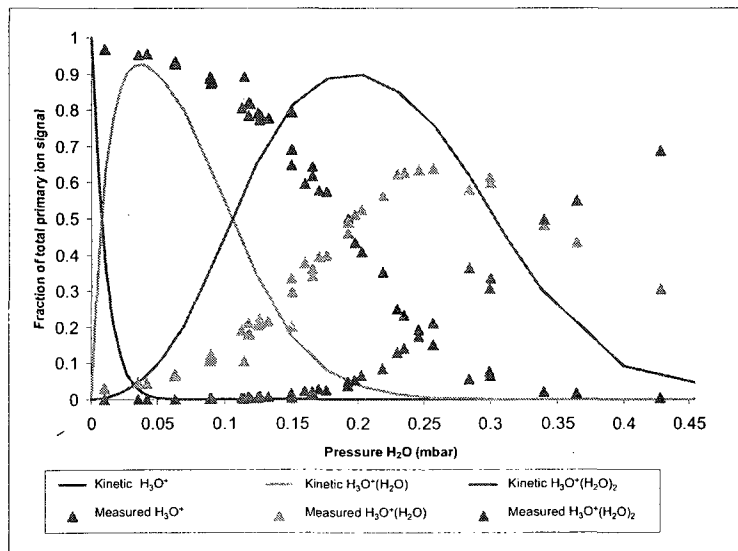


Figure 3-9 (a-b). The effect of reducing the estimated T_{eff} in the cluster model by 20% (a) and by 50% (b), showing that the variance in the effective temperature of reaction in the drift tube alone does not account for the discrepancy between the kinetics model and measurements.

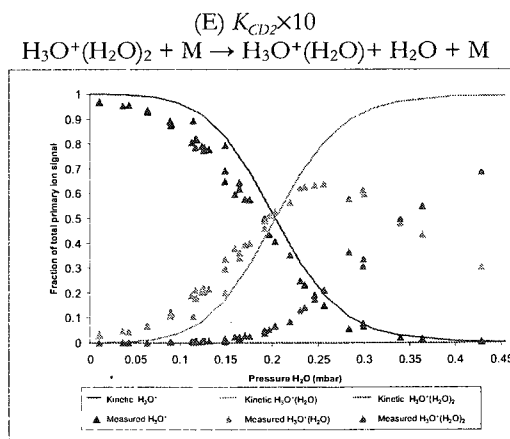
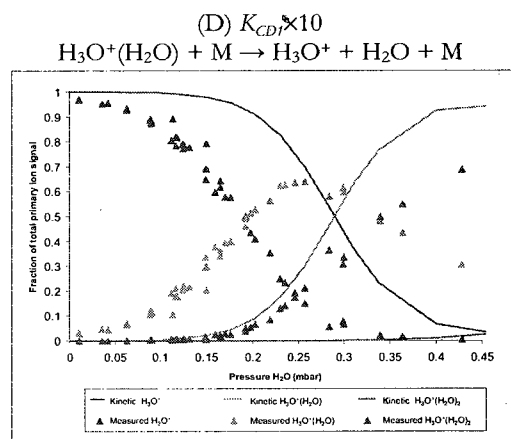
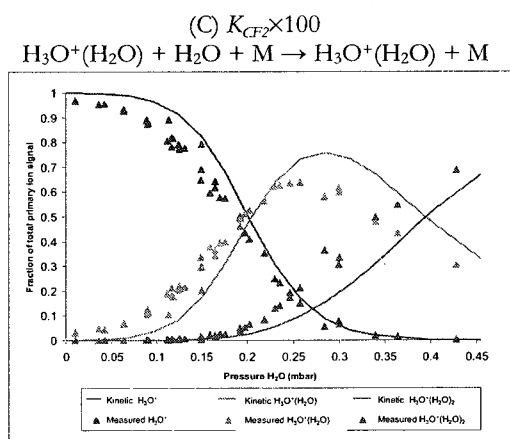
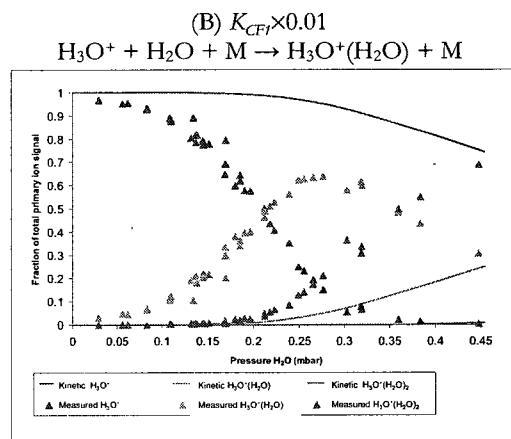
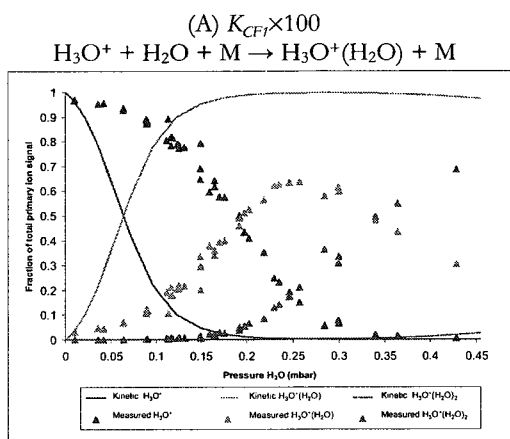


Figure 3-10 (a-e). Examples of various outcomes of kinetics model sensitivity testing. By changing the rate constants for cluster formation and destruction, different possible mechanisms for the measured cluster distributions were explored.

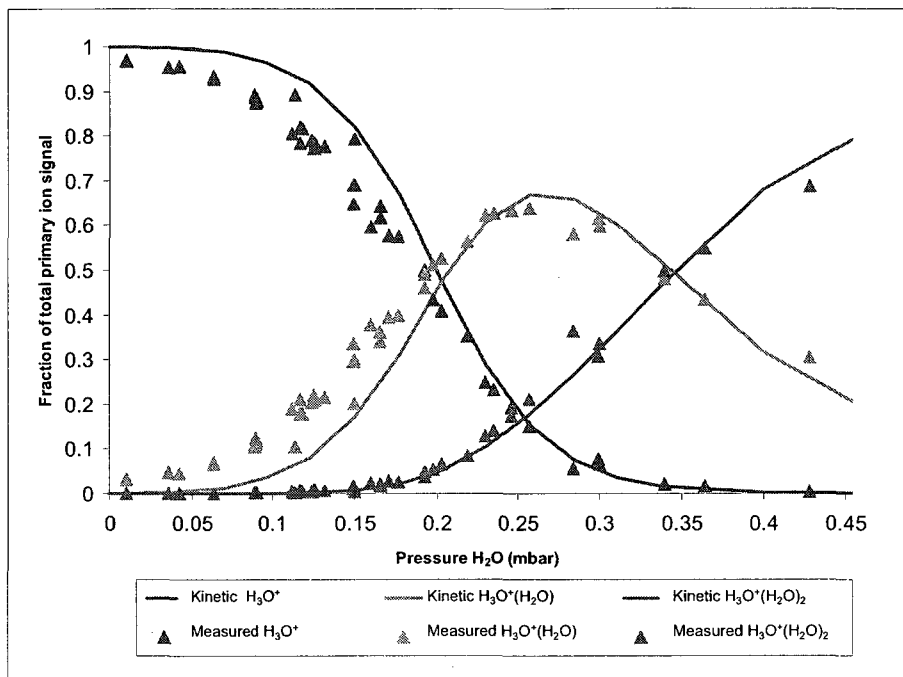


Figure 3-11. Improved match between the kinetics model and measurements caused by increasing the rate of $\text{H}_3\text{O}^+(\text{H}_2\text{O})_2$ formation from the reaction of $\text{H}_3\text{O}^+(\text{H}_2\text{O})$ and H_2O by a factor of 200.

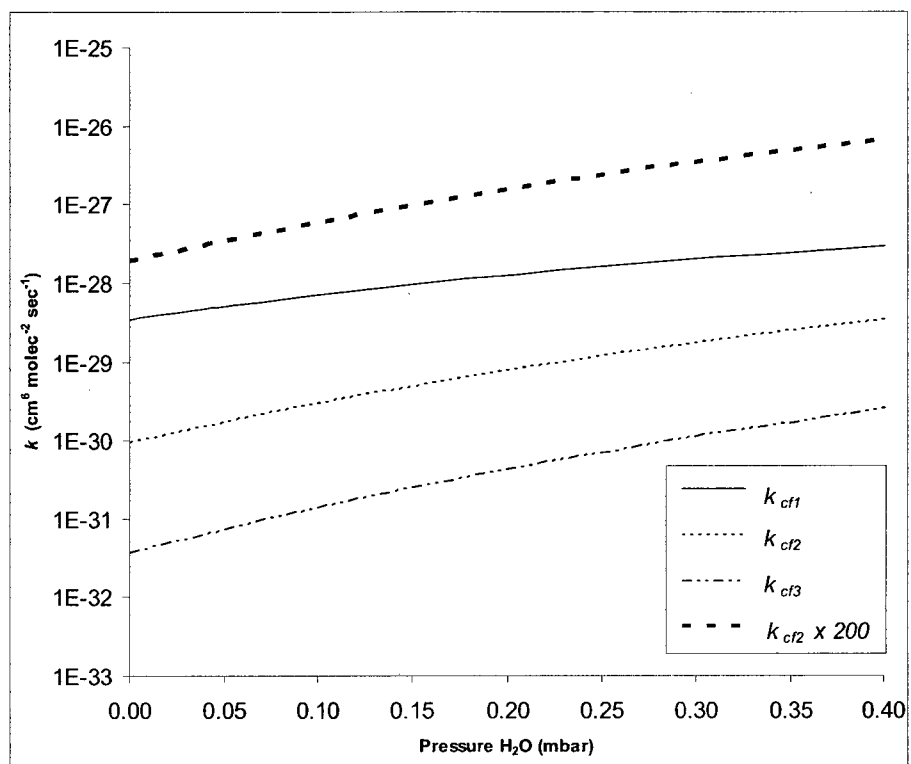


Figure 3-12. The three rate constants for cluster formation as a function of water pressure, along with k_{g2} increased by the factor of 200 to fit to the measured cluster distributions.

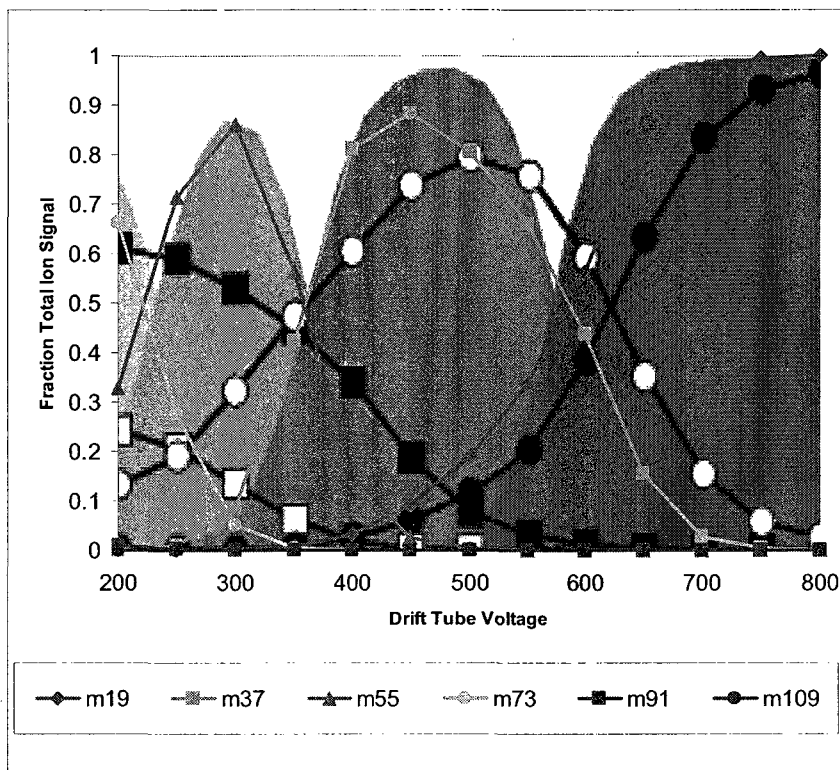


Figure 3-13. Kinetics model results superimposed on equilibrium model results (shaded curves) and measurements (black circles and squares) by de Gouw et al.³. The darkest shaded areas corresponds to H_3O^+ (m19), with successively lighter shades representing higher order clusters ($\text{H}_3\text{O}^+(\text{H}_2\text{O})_n$) (m37, m55, and m73). Solid black circles represent m19, open circles represent m37, black squares represent m55, and open black squares represent m73.

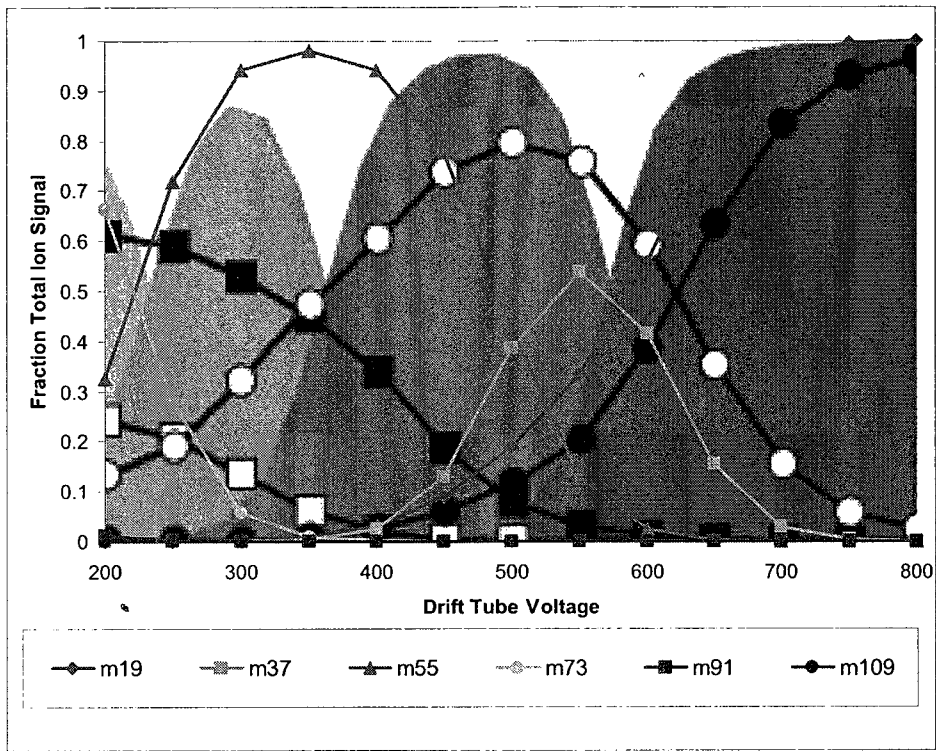


Figure 3-14. Modified kinetics model results superimposed on equilibrium model results and measurements by de Gouw et al.³ See Figure 3-13 for discussion of the symbols used.

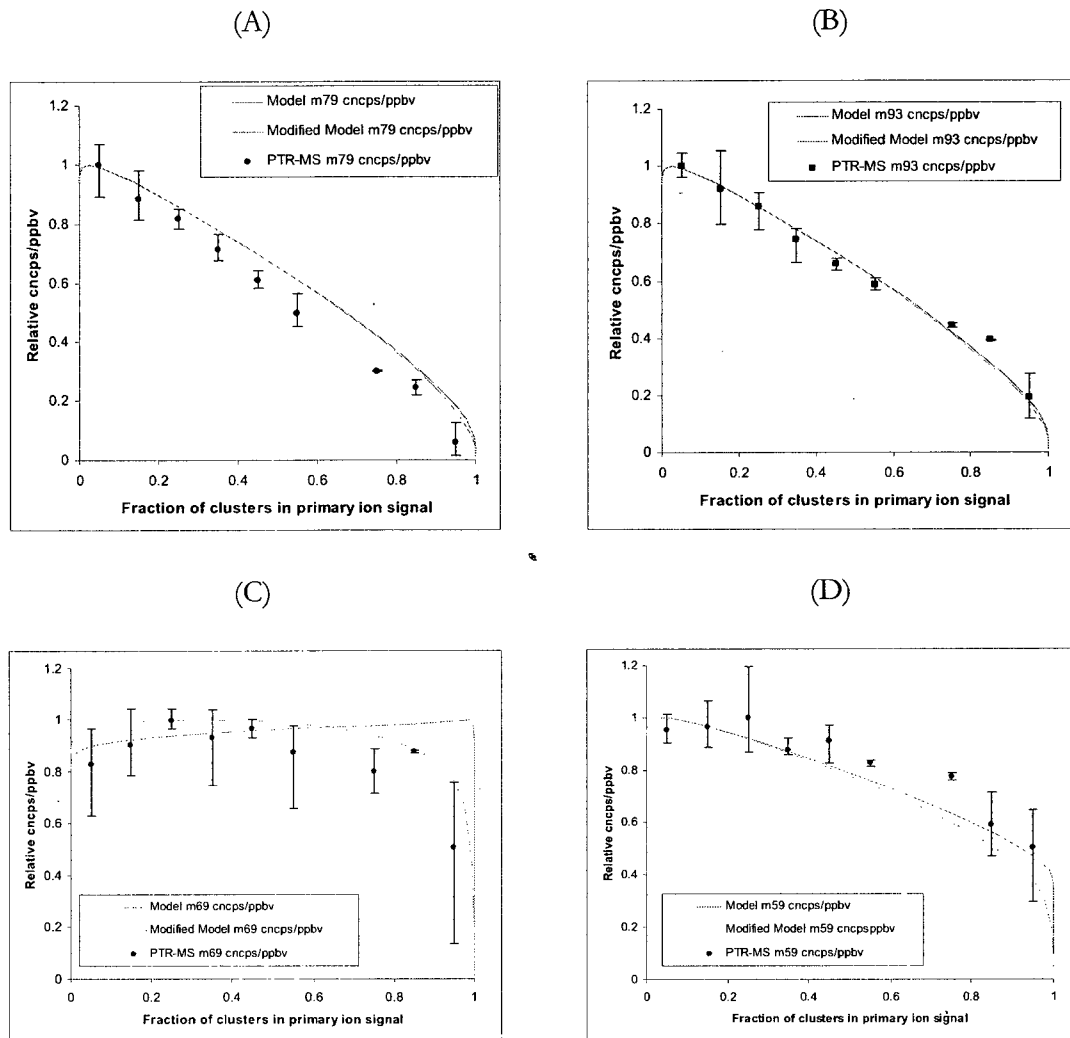


Figure 3-15. The relative response of benzene (a), toluene (b), isoprene (c), and acetone (d) as the fraction of clusters in the total primary ion signal increases, as measured by the PTR-MS in Chapter 2, and modeled using the kinetics model in both the original and modified states here.

CHAPTER 4

CALIBRATION, VALIDATION, AND MEASUREMENTS OF ACETIC ACID USING PTR-MS ON APPLIEDORE ISLAND DURING ICARTT

4.1 Introduction

Proton Transfer Reaction Mass Spectrometry (PTR-MS) has emerged as a valuable tool for monitoring Volatile Organic Compounds (VOCs) in the ambient atmosphere. Requiring only power and ultra-pure water for operation, PTR-MS instruments achieve parts-per-trillion by volume (pptv) level limits of detection and fast response to a wide range of atmospherically relevant compounds.³⁻⁵ Using PTR-MS, trace gas mixing ratios can also be estimated using proton transfer reaction kinetics, allowing quantitative monitoring (albeit with a margin of error) for compounds lacking a calibration standard. However, the PTR-MS technique has one important limitation to consider, selectivity. The only metrics used to identify compounds in PTR-MS are the proton affinity of a target compound [which must be greater than that of water ($>692 \text{ kJ}\cdot\text{mol}^{-1}$)], and the m/z of the protonated target compound (which is monitored using the mass spectrometer). The majority of PTR-MS instruments currently in use are limited to unit mass resolution as a result of the limitations of their quadrupole mass analyzer. This limitation makes it possible for isobaric protonated molecules and ion fragments to convolute the signal at a specific m/z , leading to inaccuracies in the compound quantification. Therefore, it is important to compare compounds measured using PTR-MS with measurements from an independent technique to

ensure that the signal at a specific m/z is characteristic of a target compound. For many VOCs, GC based techniques are ideal for this task. Comparisons between GC and PTR-MS instruments have shown that several compounds can be accurately measured in ambient air at various locations with a low probability of complicating signals from other compounds.^{24, 75, 76} However, in-depth characterization of PTR-MS measurements is an ongoing project, as there are compounds that have not borne in-depth validation against other techniques. Additionally, local chemistry may lead to some mass channels being harder to interpret in certain geographic areas (i.e., urban centers) than in others (i.e., rural areas). This chapter provides the first in-depth discussion on calibrating PTR-MS instruments for atmospheric acetic acid measurements, validating the results against an independent measurement technique, mist chamber samples analyzed using ion chromatograph (MC/IC), and then interpreting the atmospheric relevance of the acetic acid measurements made with a PTR-MS during the International Consortium for Atmospheric Research on Transport and Transformation campaign (ICARTT).⁷⁷ This work also serves to elucidate the methodology used to calibrate the acetic acid measurements by PTR-MS in Jordan et al.²⁶

Acetic acid is the dominant organic acid in the atmosphere, with mixing ratios reported from the pptv to a few tens of parts-per-billion by volume (ppbv) range in ambient air. It contributes to the acidity of raindrops and aerosol particles. Acetic acid is introduced into the atmosphere through primary anthropogenic, biological emissions from vegetation and soils, and combustion sources.^{34, 78, 79} Secondary production of acetic acid also occurs through oxidation of alkenes by ozone and hydroxyl radical.^{22, 80, 81} However, it reacts slowly with atmospheric hydroxyl radical and does not readily photolyze in the troposphere, and the major loss pathway is through dry and wet deposition.^{34, 82} Moreover, atmospheric acetic acid measurements are challenging as the compound readily adsorbs to transfer lines and

instrument surfaces. Several analytical techniques, including denuders, impregnated filters, selective resins, and mist chambers have been used with varying degrees of success.³⁵ In this study we demonstrate that PTR-MS instruments can be calibrated to measure ambient acetic acid with precision and accuracy.

Acetic acid readily participates in proton transfer reactions, making it a candidate for detection using PTR-MS. It reacts with H_3O^+ at with a rate constant of $3.0 \times 10^{-9} \text{ molec}^{-1} \cdot \text{cm}^3 \cdot \text{sec}^{-1}$, and has a proton affinity of $784 \pm 8 \text{ kJ} \cdot \text{mol}^{-1}$.⁸³ Protonated acetic acid $(\text{CH}_3\text{COOH})\text{H}^+$ is measured at m/z 61 in the PTR-MS mass spectrum and can undergo dehydration to produce acylium ions (CH_3CO^+ at m/z 43) inside the PTR-MS drift tube. It has been shown that this dehydration pathway is disfavored (endothermic by $113.7 \text{ kJ} \cdot \text{mol}^{-1}$) at ambient temperatures, but its probability increases with temperature, and is dependent on the E/N ratio of the drift tube.^{58,83} At very high field strength ($\geq 200 \text{ Td}$, $1 \text{ Td} = 10^{-17} \text{ V} \cdot \text{cm}^2$), another fragment appears at m/z 15, the methyl cation CH_3^+ .¹ Several other conceivable atmospheric compounds can contribute to these mass channels, including: glycoaldehyde, propanols, peroxyacetic acid, and ethyl acetate for m/z 61.^{3, 4, 25, 27, 63, 84, 85} Many compounds may also fragment to give an ion at m/z 43, which coincides with fragment ions from acetaldehyde, propanols, butanal, peroxyacetonitrates (PANs), and ethyl acetate.^{3, 25, 85, 86} However, these compounds are not usually present in large mixing ratios for most conditions experienced in a rural atmosphere, enabling several research groups to monitor acetic acid levels in ambient and controlled atmospheres using PTR-MS.^{13, 22-24, 28, 81, 84, 86-90}

Direct calibrations of PTR-MS instruments to measure acetic acid at atmospherically relevant mixing ratios have been a challenging prospect. In spite of numerous situations where the compound has been monitored,^{1, 15, 20, 23, 87, 91-94} reports of direct PTR-MS calibrations of acetic acid are sparse in the literature. For example, Lee et al.²² calibrated their

instrument by diluting neat acetic acid into a Teflon bag with purified air. Wyche et al.⁸⁴ used a permeation tube to calibrate their CIR-TOF-MS. Warneke et al.^{32, 85} used uncertified permeation tubes to generate gas phase acetic acid to characterize fragmentation and humidity dependence, but did not generate a calibration factor. Additionally, there have been several promising measurement comparisons of acetic acid measurements using PTR-MS and other techniques. de Gouw et al.²⁴ used an indirect calibration by referencing the PTR-MS signal to mist chamber data. Christian et al.⁹⁵ compared several analytical techniques for monitoring biomass burning emission and found that correcting the signal at m/z 61 for acetic acid fragmentation gave good agreement with open path FTIR measurements (PTR-MS/FTIR=1.17 \pm 0.34). A detailed review of past reported calibrations and comparisons, along with the results obtained in this study, are summarized in Table 4-1.

4.2 Experimental:

For the work presented here, two different proton transfer reaction mass spectrometers were used. The first instrument [PTR-MS-1 (SS)] was originally configured as a standard sensitivity model. The second [PTR-MS-2 (HS)] was a high sensitivity model, which features an additional vacuum stage between the drift tube and the quadrupole mass spectrometer. Later, the standard sensitivity model was upgraded to high sensitivity [PTR-MS-1 (HS)]. In addition to the high sensitivity upgrade, PTR-MS-1 (HS) was further modified so that the flow path between the ion source skimmer and the turbo pump was shortened from 37 cm to 15 cm in order to reduce the amount of water vapor entering the drift tube from the ion source. Reducing the amount of water entering the drift tube, the probability of reverse proton transfer reactions to water molecules from ionized compounds is reduced, thereby increasing the response to compounds with a proton affinity close to

water. This modification is similar to that described elsewhere,⁴⁶ and was not done to specifically enhance the performance of PTR-MS-1 (HS) for measurement of acetic acid.

Acetic acid is a *sticky* compound, meaning that it adsorbs to all transfer lines and instrument surfaces. Because of this, acetic acid presents a challenge to many techniques for generating accurate standards and robust calibration methods. Additionally, acetic acid is very soluble in water. These properties make it exceedingly difficult to generate compressed gas cylinders with stable mixing ratios of acetic acid, and it is hard to achieve quantitative retrieval through wetted surfaces like mass flow controllers and in-line valves. Instead of using synthetic or whole air standards contained in high pressure cylinders, a permeation source is used to generate stable mixing ratios of acetic acid, as described previously.⁷⁹ To avoid hysteresis problems with wetted surfaces and dead volumes in the acetic acid flow path, a free flowing calibration system was used where the acetic acid was only exposed to inert glass, stainless steel, and Teflon surfaces. All gas flows were controlled upstream of the permeation oven and the PTR-MS. The permeation oven was well insulated from variation in ambient temperature; the oven temperature was thermostatically controlled and embedded in a large thermal block to buffer it against variations in room temperature and cycling of the heating elements (Figure 4-1). Purified air was generated using a Pd-on-alumina (0.5%) bead filled catalytic converter (Apel-Riemer Environmental) operating at 425°C. This purification technique removes hydrocarbons and other reactive impurities from air while leaving major constituents like water vapor and CO₂ intact. The flow of purified air was then split into two channels, which were controlled by mass flow controllers (MKS Instruments). Both flows were controlled upstream of the permeation oven using to avoid exposing the wetted surfaces in the controllers to acetic acid. A constant permeation flow (F_{perm}) of 100 ($\pm 5\%$) cm³·min⁻¹ was directed to the permeation oven through 0.62 cm (1/4")

Teflon tubing. The permeation flow configuration was arranged to minimize the ambient air swept through the oven when it was opened to introduce a permeation tube. The second purified air channel was a variable dilution (F_{dil}) flow that ranged between 0 and 7000 ($\pm 5\%$) $\text{cm}^3 \cdot \text{min}^{-1}$. The dilution flow was mixed with the permeation flow at a T-union, forming a combined flow ($F_{perm} + F_{dil}$) that was sub-sampled 61 cm downstream by the PTR-MS. A length of tubing extended beyond the PTR-MS inlet to prevent lab air from mixing into the system. The total length of the transfer lines after the permeation oven was less than one meter. This was to prevent backpressure from developing in the permeation oven, which would increase the emission rate of the permeation tube. Acetic acid was generated by diluting neat acetic acid emitted from a gravimetrically certified $103 \pm 5\% \text{ ng} \cdot \text{min}^{-1}$ permeation tube (Kin-Tek, Inc.) held at the tube's certification temperature of 30° C . This was the smallest permeation rate available at the time of ordering, a note that is further discussed below.

The mole fraction of acetic acid from the calibration system was calculated from the emission rate of the permeation tube (ε), the permeation flow (F_{perm}), and the dilution flow (F_{dil}). To determine the mixing ratio of acetic acid generated by the permeation system, the emission rate of the permeation tube was converted to $\text{molec} \cdot \text{min}^{-1}$ by Equation 31:

Equation 31:
$$\Xi = \frac{\varepsilon \cdot N_A}{M \cdot 10^9}$$

where ε is the emission rate of the permeation tube ($\text{ng} \cdot \text{min}^{-1}$), N_a is Avogadro's number ($6.0221 \times 10^{23} \text{ molecules} \cdot \text{mol}^{-1}$) M is the molar mass of compound in the permeation tube (acetic acid in this case, $60.052 \text{ g} \cdot \text{mol}^{-1}$).⁹⁶ In order to determine the mixing ratio of acetic acid in the flow of gas from the permeation oven, it is convenient to express the gas flows $\text{molec}^{-1} \cdot \text{min}$ (\tilde{F}_i):

Equation 32:
$$\tilde{F}_i = \frac{F_i \cdot P \cdot N_A}{R \cdot T}$$

where P is the ambient pressure (assumed 1 atm in this study), R is the ideal gas constant ($82.504 \text{ K}^{-1} \cdot \text{mol}^{-1} \cdot \text{cm}^3 \cdot \text{atm}^{-1}$), T is the ambient temperature in Kelvin. The final mole fraction of acetic acid (x) in the final flow from the permeation oven using:

Equation 33:
$$x = \frac{\Xi}{(\tilde{F}_{dil} + \tilde{F}_{perm} + \Xi)}$$

where \tilde{F}_{dil} is the dilution flow in $\text{molec} \cdot \text{min}^{-1}$, and \tilde{F}_{perm} is the permeation flow in $\text{molec} \cdot \text{min}^{-1}$.

This relationship imparts some notable constraints on the generation of a calibration gas from a permeation source. The permeation source emits its target molecule at a constant rate, so there is a constant amount being released into the sample stream under any given set of flow conditions per unit of time. In order to change the mixing ratio of the target compound in the calibration gas, the dilution flow was increased. Therefore, there are some practical limits to this technique. At sufficiently high flow rates, the catalytic converter can be overwhelmed, (usually above $5000 \text{ cm}^3 \cdot \text{min}^{-1}$, but sometimes compound breakthrough has been observed at $2000 \text{ cm}^3 \cdot \text{min}^{-1}$ when heavily contaminated ambient air is present) and the resulting flow of air will carry contaminants from the ambient atmosphere. Additionally, very high gas flows may cause pressure build up in the transfer lines around the permeation oven, altering the permeation rate of the target molecule from the permeation tube. Because the mixing ratio of the target compound is controlled by F_{dil} its mixing ratio is inversely proportional to F_{dil} implying that very large increases in flow are required for sequentially smaller changes in mixing ratio. This is in contrast to the linear dependence of product mixing ratio on ϵ . In order to calibrate any instrument to representative mixing ratios for a

target compound, it is very important to obtain a permeation tube with an appropriate ε because it is challenging to reduce the mixing ratio using dilution alone. Figure 4–2 shows the dependence of acetic acid mixing ratio on dilution flow.

All instrument configurations were tested under our standard operating conditions with a drift tube pressure of 2.0 mbar, temperature of 45°C, voltage of 600V, yielding corresponding field strength 132 Td (1 Td=10⁻¹⁷ V·cm²·molec⁻¹). To explore the fragmentation and sensitivity dependence on field strength, the calibration of PTR–MS–1 (HS) was performed with drift tube voltages of 400, 433, 481, 530, and 600V, corresponding to E/N ratios of 88, 95, 106, 116, and 132 Td, respectively.

To ensure that products from the reaction between O₂⁺ and acetic acid did not bias results, the ion source was optimized such that O₂⁺ was less than 1% of the H₃O⁺ signal. Each calibration experiment was started without the permeation tube in the oven to obtain a background signal. When the signal for m/z 61 stabilized, the permeation tube was placed into the oven. When the m/z 61 signal stabilized again, the secondary dilution flow was reduced to increase the acetic acid mixing ratio so that a multipoint calibration could be obtained. As a check for outside contaminants, the mass spectrum between m/z 33 and m/z 99 was regularly scanned (every 20 measurement cycles).

The sensitivity of the PTR–MS to acetic acid is expressed in terms of the *calibration factor* (Equation 34). The calibration factor is the sensitivity (Hz at m/z 61 for every ppbv acetic acid) normalized to the primary ion signal (Hz of H₃O⁺, m/z 19), and scaled by 10⁶. The units of the calibration factor are ncps·ppbv⁻¹.

Equation 34:
$$\frac{ncps}{ppbv} = \frac{m/z\ 61}{H_3O^+ \cdot [Acetic\ Acid]} \times 10^6$$

4.3 Results:

4.3.1 Standard Sensitivity Calibrations with PTR-MS-1 (SS)

Initial studies were carried out using the Standard Sensitivity PTR-MS in our laboratory at the University of New Hampshire. Different calibration curves were measured using both the gravimetrically certified and cross-calibrated permeation tubes in order to optimize the calibration technique. This PTR-MS was located at the Thompson Farm Observing Station during the ICARTT campaign and remained there until it was replaced by our high sensitivity PTR-MS [PTR-MS-2 (HS)] in 2005.

During these calibration experiments, the instrument typically generated a primary ion (H_3O^+) signal of 2-4 Mhz. (A review of the distributions of protonated clusters measured by all PTR-MS configurations in this study are listed in Table 4-3). The background signal in both m/z 61 was 6.3 ± 1.7 ncps, and the average background for m/z 43 was 6.3 ± 1.9 ncps. A typical calibration curve with the signal in ncps is displayed in Figure 4-3 (a). The mixing ratios of acetic acid measured in this curve (and all others) were 8.4 ± 0.8 , 13.8 ± 1.4 , 20.4 ± 2.0 , and 26.8 ± 2.7 ppbv. As mentioned previously, the entire mass spectrum was scanned periodically during the calibration process. It is worth noting that during one calibration experiment, grounds maintenance activities involving gasoline powered grass cutting equipment occurred near the system inlet, and many signals appeared in the mass spectrum besides those attributed to acetic acid. Data from this time period were removed from the final calculations.

Overall, the standard sensitivity PTR-MS responded relatively rapidly to changes in the acetic acid mixing ratio. This was quantified by calculating the rise time, which is the time it took to go from 10% to 90% of the final signal. Generally, the rise times were less than an

hour, although ultimate stability took about twice as long to achieve. Additionally, the time to achieve signal stability was shorter for high mixing ratios than for low. The rise times were calculated from a 10 point moving average of the data and are shown in Figure 4-4 (a). The rise time decreases as mixing ratios increase. The average rise time for the transition from 0 to 8.4 ppbv is 48 minutes, but is only 15 minutes for the transition from 20.4 to 26.8 ppbv. The rise times correspond to the maximum rate of change in mixing ratio the system can detect, which is the ratio of the mixing ratio change to the rise time in $\text{ppbv}\cdot\text{min}^{-1}$, (Figure 4-4(b)). The slowest rate of change occurred when the acetic acid mixing ratio was increased from 0 to 8.4 ppbv, resulting in an average rate of $0.2 \text{ ppbv}\cdot\text{min}^{-1}$. Values for the intermediate mixing ratios were similar in magnitude ($0.25 \text{ ppbv}\cdot\text{min}^{-1}$), but could be differentiated from the slightly larger values obtained at the 20.4 ppbv step. The final step (26.8 ppbv) exhibited much faster maximum rate of $0.4 \text{ ppbv}\cdot\text{min}^{-1}$, 2.5 times faster than that of the first step. The calibration for PTR-MS-1 (SS) yields a calibration factor for acetic acid (m/z 61) of $7.0 \pm 0.3 \text{ ncps}\cdot\text{ppbv}^{-1}$. The acylium ion (m/z 43) generates a calibration factor with the same value, 7.0 ± 0.3 .

The ratio of m/z 61 to m/z 43 on PTR-MS-1 (SS) was 0.86 or 46% and 54%, respectively of the total acetic acid signal (m/z 61+ m/z 43). In comparison, this value is among the lowest published values, but the calibration factor is very similar to the one obtained by de Gouw et al.²⁴ Upon inspection of the scan data, a small signal at m/z 79 was present when the calibration flow was on, which correlated with m/z 61. This signal is attributed to the hydrated acetic acid water cluster $\text{CH}_3\text{COOH}_2^+(\text{H}_2\text{O})$. While protonated benzene would also appear in this mass channel, m/z 79 did not increase above the limit of detection when calibrations were done on PTR-MS-2 (HS). This rules out the possibility of

benzene contamination in the permeation tube. External contamination from lab air is also ruled out by the consistent presence of m/z 79 and the reproducible ratio to m/z 61 and 43 in all of the calibration curves carried out with PTR-MS-1 (SS). The only time that laboratory air could enter the calibration system is when the flow of acetic acid is initiated, when the permeation tube was placed in the oven. If benzene-laden air was entering the system through this route, it would seem more likely to show a decrease in m/z 79 over the course of the calibration as it was flushed from the system. However, the signal at m/z 79 started with the flow of acetic acid, and increased in step with the mixing ratio of acetic acid.

A strong humidity dependence of PTR-MS sensitivity to acetic acid was not expected. Warneke et al.³² explicitly noted the absence of a humidity dependence. Furthermore, high E/N ratios are very effective in suppressing cluster formation. To evaluate the possibility of a humidity dependence on acetic acid sensitivity, desiccant and molecular sieve filters (DriRite, Alltech) were attached to the inlet line of the catalytic converter to remove ambient water vapor from the sample air stream. Overall, reduction of the amount of water vapor entering the PTR-MS inlet resulted in reduction in the fraction of water clusters in the drift tube. For the studies where the air was at ambient humidity, the average ratio of $\text{H}_3\text{O}^+(\text{H}_2\text{O})$ (m/z 37) to H_3O^+ (m/z 19) was 0.09, and the ratio of $\text{H}_3\text{O}^+(\text{H}_2\text{O})_2$ (m/z 55) to H_3O^+ was 7.5×10^{-4} . With the filters in-line, these values reduced to 0.05 and 2.1×10^{-4} , respectively. The calibration factor from m/z 61 obtained in dry air was 6.9 ± 0.3 ncps·ppbv⁻¹, while the calibration factor at m/z 43 was 5.6 ± 0.3 ncps·ppbv⁻¹. The calibration factor at m/z 61 was within the uncertainty of the calibration factor obtained under normal conditions, but the one at m/z 43 was lower by 1.4 ncps·ppbv⁻¹. The total response (the sum of m/z 61 and m/z 43) is 12.5 ± 0.4 . The fragmentation ratio of m/z 61 to m/z 43 was also higher, 1.05. Additionally, for the dry curve, m/z 79 did not exceed the

limit of detection. The net result of reducing the humidity in the drift tube is decreased fragmentation and somewhat lower ionization efficiency of acetic acid. A summary of the calibration factors obtained for PTR-MS-1 (SS) is provided in Table 4-1 and a summary of the fragmentation ratios is given in Table 4-2.

4.3.2 Calibration of a High Sensitivity PTR-MS [PTR-MS-2 (HS)]

Our other PTR-MS [PTR-MS-2 (HS)], a high sensitivity PTR-MS, has been stationed at the Thompson Farm field site performing measurements of trace gasses as part of the AIRMAP project since 2005. After the laboratory based calibration studies, the permeation system was transported to the field site at Thompson Farm and reassembled for use with PTR-MS-2 (HS). The same calibration procedure was performed as with PTR-MS-1 (SS). The background signal was monitored for several hours, and was then followed by the 4 step calibration curve. This instrument was operated under the same conditions as PTR-MS-1 (SS): The drift tube was kept at 2.0 mbar, 45°C, 600V, for field strength of 132 Td. The ion source was used with 11 sccm of water, and the discharge settings were 600V and 0.8 mA. Again, during the calibration, m/z 61 and m/z 43 were monitored, and a full spectrum scan (between m/z 33 and 99) was initiated by the analysis sequence every 20 minutes during calibrations to check for contamination. The calibration curve obtained with this instrument is shown in Figure 4-3 (b). The PTR-MS-2 (HS) displayed a more rapid response than PTR-MS-1 (SS) with the acetic acid signal stabilizing within the period of a measurement cycle (less than 20 seconds). During the calibration, the average primary ion signal (m/z 19) was 5.15 MHz. The background signal at m/z 61 was 3.22 ± 0.30 ncps, and the background signal at m/z 43 was 2.29 ± 0.24 ncps.

From the calibration experiment, the response at m/z 61 was 8.5 ± 0.4 ncps·ppbv⁻¹, and the response at m/z 41 was 4.9 ± 0.2 ncps·ppbv⁻¹. The total signal (m/z 61 and m/z 43) was 13.4 ± 0.4 ncps·ppbv⁻¹. The ratio of the signal at m/z 61 to m/z 43 was 1.47. This value is significantly higher than that of PTR-MS-1 (SS). The source of this result is uncertain; however, the amount of water vapor in the drift tube may have something to do with the different fragmentation ratios. PTR-MS-2 (HS) had much smaller cluster distributions for this study, the ratio $H_3O^+(H_2O)$ (m/z 37) to H_3O^+ (m/z 19) was 0.01, and the ratio of $H_3O^+(H_2O)_2$ (m/z 55) to H_3O^+ (m/z 19) was 1.4×10^{-5} . These values are ~20% of those obtained with PTR-MS-1 (SS). The calibration factor obtained for PTR-MS2 (HS) is provided in Table 4-1 and the fragmentation ratios are provided in Table 4-2.

4.3.3 PTR-MS-1 (HS) Calibration and E/N dependence

After the calibrations of PTR-MS-1 (SS), the instrument was upgraded to the high sensitivity configuration using a conversion kit supplied by Ionicon Analytic. The main difference between the standard sensitivity and the high sensitivity configuration is the addition of a second turbo pump, which provides additional pumping capacity in the detection region of the PTR-MS. As mentioned in the introduction, PTR-MS-1 was further modified to increase the pumping capacity of the skimmer region between the hollow cathode discharge and the drift tube. Originally, this path was 37 cm long. By changing the position of vacuum fittings and rotating the ion source 120°, it was possible to replace the original 32 cm, 0.62 cm (1/4" inch) OD Teflon tube with a 10 cm tube, shortening the flow path to 15 cm.

An enhanced test procedure was developed for this instrument in order to explore the relationship between the field strength in the drift tube (the E/N ratio) and the

calibration factor for acetic acid. The drift tube was maintained at 2.0 mbar and 45°C. The mixing ratio of acetic acid was stepped from zero (for background determination) to 7.0, 13.8, and 26.8 ppbv. At each calibration level, the drift tube was stepped through the following voltages: 400, 433, 481, 530, and 600V, corresponding to E/N ratios of 88, 95, 106, 116, and 132 Td.

For PTR-MS-1 (HS), the average H_3O^+ signal was 1.1-1.8 MHz for all field strengths. At 132 Td, the ratio of $\text{H}_3\text{O}^+(\text{H}_2\text{O})$ (m/z 37) to H_3O^+ (m/z 19) was 4.67×10^{-3} , and the ratio of $\text{H}_3\text{O}^+(\text{H}_2\text{O})_2$ (m/z 55) to m/z 19 was 3.0×10^{-6} . These values are much lower than those obtained with PTR-MS-1 (SS) and with PTR-MS-2 (HS) (Table 4-3), indicating the effectiveness of the shortened skimmer flow path in removing water from the ion source. At the lowest E/N (88 Td), the fraction of $\text{H}_3\text{O}^+(\text{H}_2\text{O})$ increased to 9.69×10^{-2} and $\text{H}_3\text{O}^+(\text{H}_2\text{O})_2$ was 2.97×10^{-2} of the primary ion signal. The calibration factors obtained during these measurements are shown in Figure 4-5. At E/N 132 Td, the calibration factor for m/z 61 was 10.9 ± 0.7 ncps·ppbv⁻¹. This value increased inversely with E/N to 30.8 ± 2.6 ncps·ppbv⁻¹ at an E/N ratio of 88. The calibration factor at m/z 43 remained relatively constant with field strength, with a calibration factor of 4.9 ± 0.3 at E/N of 132 Td, and decreasing to 4.1 ± 0.4 at an E/N of 88 Td.

4.3.4 Clusters and Fragmentation: E/N Ratios and Humidity

Studies of the chemistry between H_3O^+ and acetic acid conducted at lower ion-molecule collision energies (using select ion flow tube (SIFT) and flowing afterglow (FA)) have not detected ions at m/z 43 as a reaction product; thus, the fragmentation of acetic acid is initiated by the higher ion molecule collision energies present in the drift tube.^{83,97} The ratio of m/z 61 to m/z 43 decreases at higher E/N values, indicating that

greater amounts of fragmentation occur with increasing collision energy. The ratios of (m/z 61)/(m/z 43), the ratios of hydrated clusters, and the fraction of each ion in the acetic acid signal obtained in each experiment are shown in Table 4–2. The ratio is 5.96 at E/N of 88 Td, decreasing to 1.94 at E/N of 132 Td. Fragmentation also varies between the PTR–MS instruments. PTR–MS–1 (HS) showed the least fragmentation with a ratio of 1.94, followed by PTR–MS–2 (HS) with a ratio of 1.47, and finally PTR–MS–1 (SS) with 0.86. The fragmentation ratio of acetic acid in PTR–MS–1 (SS) increased to 1.05 when dry calibrations were performed. This finding suggests that fragmentation is dependant on water vapor in the drift tube.

To further examine the impact of humidity on fragmentation, the ratio of $H_3O^+(H_2O)$ (m/z 37) to H_3O^+ (m/z 19) was plotted along with the ratio of acetic acid to acylium ion across all the calibration studies (Figure 4–6). The relative strength of the signal at m/z 37 to m/z 19 in the PTR–MS can be used as a proxy for the amount of water vapor in the drift tube.^{29, 32} The trend in this value correlates with the fragmentation of acetic acid: PTR–MS–1 (HS) had the lowest fraction of m/z 37 and the least amount of fragmentation, while PTR–MS–1 (SS) had the largest fraction of m/z 37 and the most fragmentation. Thus, there appears to be a relationship between water vapor and fragmentation of acetic acid; however, this does not appear to have a significant effect on sensitivity at m/z 61, as the calibrations obtained for the dry and normal conditions are the same within the uncertainty of the measurements.

A weak signal at m/z 79 was also present at E/N ratios of 88 Td and 96 Td, but was not detectable at higher E/N ratios in PTR–MS–1 (HS). This result reinforces the earlier conclusion that the signal at m/z 79 is a hydrated acetic acid cluster [$CH_3COOH_2^+(H_2O)$] rather than benzene contamination. A signal at m/z 79 was also detected at an E/N ratio of

132 Td using PTR-MS-1 (SS); however, this was much weaker than the signal detected at the low E/N ratios and is indicative of ligand switching reactions occurring between acetic acid and $\text{H}_3\text{O}^+(\text{H}_2\text{O})$. It is unclear if there is any direct relationship between increased fragmentation and the presence of these clusters. Hartungen et al.⁹⁸ also noted the presence of this ion in their standard sensitivity PTR-MS (comprising 3.7% of the total acetic acid signal), noting that the presence of the ion was enhanced by the high humidities present in their experiments. The fraction of m/z 37 was ~25% in their study, much higher than the results presented here. In following with their discussion, it is likely that the hydrated acetic acid clusters undergo collision induced dissociation subsequent to their formation, explaining why the signal at m/z 79 is very small. The protonation, fragmentation, and ligand switching pathways are illustrated in Figure 4-7.^{83, 98} Further studies using SIFT could elucidate the kinetics of the ligand switching pathway and show if the formation of the acylium ion is related to that process.

4.4 Measurements of Acetic Acid on Appledore Island during ICARTT 2004

4.4.1 Overview

During the ICARTT campaign,⁷⁷ our group operated the PTR-MS-2 (HS) on Appledore Island, which is located 11 km off the coast of New Hampshire, USA (42.97°N, 70.62°W), and is managed by the Shoals Marine Lab (www.sml.cornell.edu) and hosts an AIRMAP Monitoring Station (airmap.sr.unh.edu). The observing station is located in a 20 m tall World War II era observing tower. The PTR-MS was operated from July 2nd to August 13th 2004, using the same drift tube and ion source conditions as those in the calibration experiments. A total of 25 mass channels corresponding to various VOCs of interest were

monitored with dwell times between 5–20 seconds. However, acetic acid is the only VOC measured by the PTR–MS during ICARTT considered in the following discussion.

Ambient air was drawn from the top of the tower through a 30.5 m long, 9.525 mm ID PFA Teflon tube, with a flow rate of $\approx 75 \text{ L}\cdot\text{min}^{-1}$. A membrane pump was used to draw sub–stream of air from the main inlet line at a flow rate of $1 \text{ L}\cdot\text{min}^{-1}$, from which the PTR–MS sampled. Every 2.5 hours, the PTR–MS control software automatically switched the sample flow through a 13 cm long, 1.27 cm ID 0.5% Pd–on–alumina bead catalytic converter at 450° C for 30 minutes. The catalytic converter oxidizes VOCs from the sample stream to provide a measurement of instrument background. No special modifications were made to the instrument to remove aerosol particles from the sampled air or otherwise modify for acetic acid measurements.⁹⁹ It is worth noting that there are several significant gaps in the dataset due to power fluctuations and outages on the island. However, 6625 individual measurements were made by the PTR–MS during the campaign.

A time series of acetic acid mixing ratios are shown in Figure 4–8. The average relative uncertainty of the PTR–MS measurements of acetic acid over the course of the ICARTT campaign is estimated to be 18.3% (2σ).¹⁰⁰ In addition to the PTR–MS data, several other data sources were used for this analysis. Hourly meteorological data was obtained from the IOSN3 monitoring station on Isle of Shoals, NH, (www.ndbc.noaa.gov). The carbon monoxide (CO) and ozone (O_3) data are from measurements at the AIRMAP observation station (airmap.sr.unh.edu).

4.4.2 Comparison with MC/IC Measurements

4.4.2.1 MC/IC Suitability and Operation

To validate the measurements of ambient acetic acid mixing ratios using the PTR-MS, the results were compared with concurrent gas phase acetic acid measurements made by MC/IC over two hour intervals during ICARTT.¹⁰¹ The MC/IC technique has been successfully deployed by several groups to quantify organic acids in the atmosphere on ships, aircraft, and stationary field sites.^{79, 101-103} Configured appropriately, the MC/IC system differentiates between gas phase and aerosol phase acetic acid, and the chromatographic separation provides positive identification of the compound, making MC/IC a robust measurement technique. For the MC/IC measurements of acetic acid, the precision was 10%, and the limit of detection for acetic acid was ~3 pptv.^{35, 104} In order to meaningfully compare the PTR-MS and MC/IC technique, the PTR-MS measurements were averaged into the two hour sample collection window employed by the MC/IC. Only data corresponding to the time periods when both instruments were operational are included (Figure 4-9).

4.4.2.2 Results of PTR-MS and MC/IC Measurements

For the data shown in Figure 4-9, several features are apparent when comparing the PTR-MS and MC/IC data sets. First, the mixing ratios reported by the PTR-MS are generally larger than those of the MC/IC. The benefit of the time resolution offered by the PTR-MS technique is shown by the high variation of the its acetic acid signal over the 2 hour integration period of the MC/IC system. This is highlighted by the light blue shading around the PTR-MS measurements, which illustrates the minimum and maximum values on the integration interval. A correlation plot of the acetic acid data from the PTR-MS and

MC/IC measurements is shown in Figure 4–10. The resulting slope of a weighted orthogonal least squares regression (OLS) (Figure 4–10), is 1.14 ± 0.06 (2σ), and the intercept is 49 ± 20 (2σ) pptv, and the correlation coefficient (R^2) for the data is 0.78, showing reasonably good agreement between the two techniques.

4.4.2.3 Analysis of Possible PTR–MS Interferences

There are several possible factors influencing the slope of the correlation between the PTR–MS and the MC/IC measurements. The PTR–MS had unusually high background counts (i.e., 10's of Hz compared to <10 Hz at m/z 79, m/z 93 and other mass channels) at m/z 61 during the campaign, and the background signal tracked the ambient signal. This is usually indicative of the transfer lines between the catalytic converter not fully desorbing or that the catalytic converter does not remove acetic acid efficiently with increased levels in ambient air. Additionally, if the background counts are anomalously high because of insufficient purification, the measured mixing ratios should have a low bias, because the amount subtracted from the measurement signal would be too large.

Since the PTR–MS instrument was not calibrated for acetic acid measurements while in place on Appledore Island, it is possible that mechanical changes in the instrument as a result of moving from the UNH to Appledore would result in different performance. It is also possible the balance of the signal at m/z 61 was the result of a combination of interfering compounds, such as glycoaldehyde, isopropanol, hydroxyacetic acid, *n*-propanol, or ethyl acetate that caused a positive sampling bias. The MC/IC technique separates particles from the bulk sample stream. Any particle phase acetic acid would be sampled by the PTR–MS and volatilized inside of the heated transfer lines. A topic of future work would be to further improve the agreement between the two techniques. Possible routes

would be to use a PTR-MS that features a time-of-flight mass spectrometer to analysis the different components at m/z 61, or to use an in situ acetic acid calibration to ensure that mechanical shocks do not skew the analysis. As discussed later on (Section 4.5), we have significantly improved the quality of the background determination since this study. Overall, we conclude that there is good agreement between PTR-MS and MC/IC measurements of acetic acid.

4.4.3 Analysis of Acetic Acid Measurements on Appledore Island during the ICARTT Campaign.

Acetic acid mixing ratios were reported for several other locations during the ICARTT campaign: our group operated a second PTR-MS [PTR-MS-1 (SS)] at the AIRMAP research station at Thompson Farm, located in rural New Hampshire.²⁶ Another group operated a PTR-MS at Chebogue Point, Nova Scotia.⁹⁰ The average and range of acetic acid values decreased the further away from the continent each measurement site was from the continent. On Appledore Island during ICARTT campaign, the average and the median mixing ratio of acetic acid was $607.9 \pm 341.8(1\sigma)$ pptv and 530.0 ± 25.4 pptv, respectively. The minimum was 74.7 ± 3.7 pptv, and the maximum was $3,555.0 \pm 170.6$ pptv, the mixing ratio at the lowest 10th percentile of measurements was at 264.2 ± 12.7 pptv, and the highest 90th percentile is at 1047.6 ± 50.3 pptv. During the summer of 2004, the median mixing ratio at Thompson Farm was 620 pptv, with the 10th percentile at 150 pptv and the 90th percentile at 2050 pptv. Directly comparable statistics for Chebogue Point are not published, but mixing ratios generally lie between 788 and 332 pptv.

Compared to Appledore Island, the median mixing ratio at TF of acetic acid was 90 pptv higher, the 90th percentile mixing ratio was 1003 pptv higher, and the 10th percentile

was 100 pptv lower. The lower 10th percentile value is possibly attributed to the stable nocturnal inversion layer that forms over the New England region. When the nocturnal boundary layer is present, acetic acid becomes depleted by deposition processes. At sunrise the nocturnal boundary layer dissipates, resulting in air mass mixing, photochemistry, and emission processes that increase the significance of sources over sinks (i.e., wet and dry deposition) for the acetic acid levels at Thompson Farm.²⁶ The lower average and lower 90th percentile of acetic acid at Appledore Island is similar to that of methanol and acetone, which have similar sources and sinks to acetic acid.¹⁰⁵ Chebogue Point is further downwind of many continental emissions sources than Appledore Island, providing more time for atmospheric processing and deposition. Qualitatively, the mixing ratios observed there seem more dampened than at Appledore Island; the range in reported characteristic mixing ratios of acetic acid are much smaller than those measured at Thompson Farm and Appledore Island.⁹⁰

4.4.3.1 Acetic Acid Wind Direction Dependence

In order to examine the effect of meteorology on the mixing ratios of acetic acid, the PTR-MS, CO, and O₃ measurements were binned with the 1 hour average meteorological data obtained from the IOSN3 station (Figure 4-11). This merged dataset was then used to search for an acetic acid mixing ratio dependence on wind direction and wind speed.

To examine the effect of wind direction on the acetic acid mixing ratios advecting over Appledore Island, the measurements were grouped into 30 degree bins by wind direction (Figure 4-12 a-e). For the majority of the measurements made, air masses originated from the south, with 160 hours of measurements made between 165 and 195 degrees, in contrast, there were only 20 hours of measurements when the wind originated

from the north (between 345 and 15 degrees). A weak directional dependence is observed in the acetic acid levels present in air masses reaching Appledore Island, with less than a factor of two separating the sector with the highest mixing ratio (the south east at 825 pptv) from the lowest mixing ratio sector (the north at 474 pptv). Furthermore, a second peak in average appears between the southern and south–southwest sectors (743 pptv). The larger average and maximum acetic acid mixing ratio, coupled with the greater standard deviation in those sectors indicates that there is a source region to the south of Appledore Island.

4.4.3.2 Acetic Acid Wind Speed Dependence

The relationship between acetic acid mixing ratios and wind speed at Appledore Island was examined, as gas exchange with the ocean is often a function of wind speed.¹⁰⁶⁻¹⁰⁸ In the past, wind speed dependence of methanol and acetone mixing ratios have been recorded on Appledore Island, indicating that those compounds have an oceanic sink.¹⁰⁵ Similarly a positive correlation between windspeed and both dibromomethane and bromoform has been observed at Appledore Island, showing that the ocean is a net source of those halogenated compounds.¹⁰⁹ Following those observations, the acetic acid measurements were tested for wind speed dependence by averaging them by windspeed (Figure 4–13a). The average mixing ratio was ~700 pptv until the wind speed reached 7 $\text{m}\cdot\text{s}^{-1}$, followed by a slight increase to 800 pptv at 10 $\text{m}\cdot\text{s}^{-1}$. There are relatively few measurements at speeds less than 2 $\text{m}\cdot\text{s}^{-1}$ and greater than 10 $\text{m}\cdot\text{s}^{-1}$. Overall it suggests that the acetic acid mixing ratios at Appledore Island are not influenced by wind speed (Figure 4–13b). In order to check the possibility that there was a directional bias obscuring this trend, the wind rose was divided into four sectors, (north, east, south, and west), and correlation plots were used to evaluate the acetic acid mixing ratio dependence on wind

speed. No clear functional relationship between wind speed and acetic acid mixing ratio is evident (Figure 4–14).

This result suggests that the net effect of direct oceanic emission or deposition is minor compared to enhancement from transport and photochemical production and wet deposition processes. While increased deposition of acetic acid with increasing speed may play some factor in the determining the mixing ratio, other factors (emission strength, wet deposition, and photochemical processes) control the observed mixing ratios.

4.4.3.3 Diurnal Variation of Acetic Acid

The daily variation of acetic acid was investigated to see if there are regular patterns that could be associated with diurnal transport, emission, and loss processes. To achieve this, the data was bin averaged by hour-of-day (EST, UTC minus 5 hours) (Figure 4–15 a–d). During the night, winds originated from the southwest transporting air from the continent close to Appledore Island, while during the daytime winds from the southeast were dominant. Coincident with changing wind direction were lower nighttime temperatures and wind speeds (Figure 4–15c and Figure 4–15d). To further illustrate the regularity of the daily pattern, the hourly acetic acid mixing ratios for the study are plotted by the hour of the day, and color coded by wind direction (Figure 4–16). With few exceptions, on every day of the study, acetic acid mixing ratios decreased overnight and into the morning hours with winds coming out of the southeast, as shown by the high density of red traces (Figure 4–16). After 0600 EST, the mixing ratios increased as the winds shifted to the southwest (yellow–green traces). Figure 4–17a shows the difference between the average during the night–time low (between 0400 and 0800 EST) and the average for the rest of the day (between 0800 and 2200 EST). For the days where there was sufficient concurrent data to compute the

difference only two days during the campaign (7/14 and 7/19) showed a decrease in mixing ratio. Figure 4-17 (b) depicts the daily change in acetic acid mixing ratio, calculated as the difference between the nighttime minimum and the daily light maximum. For the campaign, the average difference between the daytime maximum and nighttime minimum was 585 pptv. That the mixing ratio of acetic acid displays daily increases in mixing ratio, occurring at the same time, corresponding with the onset of sunlight and change in wind direction, indicates that mixing ratio of acetic acid at Appledore Island is partially controlled by a daily transport process.

Numerous other studies have found diurnal transport phenomena are important control on air quality in coast New England. White et al.¹¹⁰ reported a landbreeze/seabreeze transport regime using wind profiler data and back trajectories obtained for this same time period. They go on to describe the sources of air masses that bring high levels of ozone to Appledore Island. The authors found that ozone mixing ratios have a lobed distribution, with enhanced mixing ratios coming from both the south east and the south west, with pronounced increases in the same southern sectors where we observe the maxima in acetic acid. A cluster analysis of back trajectories show that these zones correspond to air masses that come directly from the coast in the south west sector, and to more processed air masses from Boston and coastal cities which come to Appledore's south east sector through the Gulf of Maine. That there is coincidence of high ozone and acetic acid implicates anthropogenic emissions and photochemical processing as a source of elevated levels of acetic acid at Appledore Island. This is inline with findings of many other studies.¹¹¹⁻¹¹⁵

Chen et al.¹¹⁶ took a different approach to understanding the chemical signature of gases over Appledore Island. They examined diurnal trends in VOCs, and classified air masses by age and source region at both Appledore Island and Thompson Farm. The

diurnal trend in acetic acid does not match the diurnal trends in any of the other VOCs in that study; methanol and acetone were relatively constant throughout the day, and hydrocarbon loadings increased overnight. A principal component analysis found that air quality at Appledore Island has three important input regimes: fresh emissions from nearby terrestrial and anthropogenic marine sources; processed urban air masses originating from mid-Atlantic states and the Ohio River Valley; and clean marine conditions. Comparing the acetic acid mixing ratios with the different factors from the principle component analysis, acetic acid levels were elevated at the same time that that the factors indicating fresh or aged emissions were dominant. Periods of low acetic acid tended to coincide with the factors indicating for marine air masses and sometimes for processed air masses as well. However there are points where all three factors are high, indicating mixed source characteristics and the mixing ratio of acetic acid was low. This result may mean that acetic acid has a unique set of controls compared to the gasses selected in their analysis.

That the levels of acetic acid are high when the primary emissions are the dominant control on air quality indicates that acetic acid is being emitted from local vegetative and anthropogenic sources in the seacoast region. This would coincide with a land breeze, when winds originate from the south west. Elevated mixing ratios of acetic acid that are present when factors for aged air masses are high indicate that photochemical production is active, a scenario that reflects air transported northward from coast cities. Because acetic acid usually peaks when both factors are positive indicates that a combination of primary emissions and secondary sources influences the mixing ratios observed at Appledore Island. Including other photochemically produced oxygenated species like ketones, alcohols, and aldehydes in the principal component analysis would help elucidate the significance of aging processes on

the air masses observed at Appledore Island and improve understanding of their contribution to ambient acetic acid.

4.4.3.4 Acetic Acid Relationships with CO and Ozone

Because enhanced acetic acid mixing ratios are coincident with elevated mixing ratios of anthropogenic species, we consider the possibility of predicting acetic acid mixing ratios by developing an emission ratio based on CO. Both CO and acetic acid are released by biomass and fossil fuel combustion.^{34, 117, 118} Correlation between the mixing ratio of acetic acid and CO is indicative of a common combustion source and primary emissions. An

enhancement factor $\frac{\Delta Acetic Acid}{\Delta CO}$ was determined by taking the background levels of each

compound (lower 2.5% of the measurements, 141 pptv for acetic acid, and 107 ppbv for CO), and an orthogonal least squares linear regression was used to find the slope of a line with the shortest perpendicular distance to all the pairs of acetic acid and CO data points

(Figure 4–18). The slope ($\frac{\Delta Acetic Acid}{\Delta CO}$) of the regression is 8.71 ± 0.54 (95% confidence)

$\text{pptv}\cdot\text{ppbv}^{-1}$, with $R^2=0.36$. The slope is similar to those obtained in aged forest fire plumes measured over New England during the NEAQS–ITCT2k4 campaign (measured between 0.9 and 12.9 $\text{pptv}\cdot\text{ppbv}^{-1}$).⁹⁴ It is possible that the higher ratio observed here is a product of

photochemical aging of air masses, causing enhanced mixing ratios of acetic acid in addition to those released as a primary source or that primary biogenic emissions contributed to the observed mixing ratios. Using the linear relationship between CO and acetic acid, the mixing ratio of acetic acid was estimated from the CO measurements (Figure 4–19). The mixing

ratio of acetic acid predicted by the $\frac{\Delta Acetic Acid}{\Delta CO}$ relationship tracks the acetic acid

measurements made by the PTR-MS, although there are some periods of disagreement, particularly in the period between 7/20 and 7/25, when CO mixing ratios were elevated for several days in a row. This similarity may indicate that it is possible to use CO to estimate the trends of acetic acid, implicating anthropogenic emissions as a source of acetic acid at Appledore Island.

The correlation between ozone and acetic acid is used to examine the strength the photochemical source of acetic acid. Acetic acid can be produced through ozonolysis and photochemical oxidation of alkenes and biogenic compounds.^{21, 22, 34, 80, 81, 119} Increased ozone mixing ratios would increase production of acetic acid from its parent compounds. A correlation plot of ozone and acetic acid is shown in Figure 4-20. An orthogonal least squares linear regression of the data gives a slope ($\frac{\Delta \text{Acetic Acid}}{\Delta O_3}$) of 23.99 ± 0.09 pptv·ppbv⁻¹, with R²=0.29. At ozone mixing ratios above 35 ppbv, there appears to be small, positive correlation between ozone and acetic acid. Otherwise, without considering mixing ratios of hydrocarbons that can oxidize to form acetic acid, there does not appear to be a strong relationship between acetic acid and ozone mixing ratios.

4.5 Improving PTR-MS Measurements of Acetic Acid: Current Progress and Future Directions

It is instructive to analyze the data collection methods during the ICARTT campaign to put the improvements in our technique into perspective. A plot of the signal obtained over the course of the campaign is shown in Figure 4-21. During the ICARTT campaign, our measurements of acetic acid at m/z 61 were hampered by high background count rates. It is not entirely clear what the source was of the high background signal. Further inspection of this dataset has not enabled determination of the “true” background signal during this

time period. However, Figure 4-21 shows there is clearly a decrease in background signal over the course of the campaign. Our PTR-MS was relatively new at the time, and it is possible that various wetted surfaces within the instrument, particularly the Teflon spacers within the drift tube had not yet been passivated and were steadily desorbing compounds that interfered at m/z 61. An important observation is that our background signals never reached a plateau during a calibration interval, and that they trended with ambient acetic acid mixing ratios. Several other gasses showed breakthrough behavior (were incompletely removed by the catalytic converter) at high mixing ratios, including methanol, acetaldehyde, and acetone.

In order to improve the quality of our background signal, we have adjusted our method for determining background measurements. We have replaced our original, short catalytic converters with ones that are 40.6 cm (16") long and heated to 625° C. We employed custom coiled nozzle heaters (Watlow, Inc.) instead of commodity fiberglass covered wire heating elements (Omega, Inc). The coiled nozzle heater grips the catalytic converter tightly and applies heat evenly along its length. They also feature a much higher maximum operating temperature than the wire elements. The goal in the increased length and operating temperature is to prevent breakthrough of ambient VOCs in order to obtain better background measurements.

An additional source of elevated background signals during ambient VOC events is adsorption to transfer lines. Thus, even with the improved catalytic converter, the signal of strongly adhering compounds does not stabilize within the period of a sample cycle. To minimize any hysteresis effects, the transfer lines have been shortened to the minimum feasible length and any unnecessary wetted surfaces (i.e., valves, flow controllers) between the PTR-MS and the intake manifold have been eliminated. Furthermore, our background

measurement protocol has been changed from a 30 minute period before every 2.75 hours of sampling to a 70 minute period before every 25 hours. The change in timing gives the transfer lines more time to flush, while avoiding a temporal bias in the dataset. Since there are more data points collected in each background measurement period, it is possible to get a better idea of when the system is purged. Also, background measurements that are prone to hysteresis effects are more easily identified and eliminated. An example of our current signal quality is shown in Figure 4–22, with a short period of measurements in Figure 4–23 to provide more detail about the transition between measurement and background periods. The ambient signal [in normalized counts per second (ncps)] is shown in blue, the background measurements are shown in black, and measurements retained for determination of mixing ratios are shown in green. The range of mixing ratios of acetic acid during this time period was similar to that observed during ICARTT, yet the elevation of the background signal was not present and variance of the background signal during VOC events was greatly reduced.

Future areas of improvement should focus on increasing the flush rate of ambient and zero gas through the transfer lines. Heating the transfer lines between the catalytic converter valve and the PTR–MS may greatly improve response times. Another step would be to optimize the transfer lines between the drift tube and the manifold to reduce or eliminate dead volumes where compounds could be retained. The benefits of this are underscored by the difference in response time difference between PTR–MS 1 (SS) and PTR–MS–2 (HS), latter of which responds almost instantly in comparison. Increasing the volumetric flow rate of background air should also be explored. The longer and hotter catalytic converters are still being used with a sampling rate of $1 \text{ L}\cdot\text{min}^{-1}$, and the maximum flow rate without breakthrough has not yet been explored. Employing an automated calibration system that uses permeation tubes would also be very beneficial in a future

comparison study between PTR-MS and another acetic acid measurement technique. There is still some uncertainty about the influence of other compounds on the signal at m/z 61, and online calibrations interspersed with measurements would help reduce that uncertainty when comparing to other techniques. High mass resolution time of flight (TOF) detectors would also be able to use their superior mass resolution to quantify interferences by having the ability to discriminate between compounds that are nominally isobaric at unit mass resolution inherent in most quadrupole based mass filters.

4.6 Conclusions

PTR-MS is a valuable technique for monitoring many atmospheric VOCs. By using permeation tube based calibration source, and high flow rates of dilution gas in a low back-pressure mixing system, it is possible to calibrate the PTR-MS at low ppbv mixing ratios. Our calibrations and others reported in the literature show that acetic acid fragments to varying degrees in different PTR-MS systems. Fragmentation may be mediated by the amount of water vapor available in the drift tube, as fragmentation increases in instruments that have lower ion source skimmer pumping capacities. The difference in fragmentation ratios between different instruments emphasizes the importance of parameterizing each instrument's performance, as fragmentation of acetic acid is not precisely reproducible from one system to another. At 132 Td, we obtain calibration factors that vary between 7 and 10 ncps for this compound.

During the ICARTT campaign, our group measured acetic acid using PTR-MS concurrently with the operation of an MC/IC system on Appledore Island. A comparison of the measurements concluded that the PTR-MS systematically over-predicted acetic acid by 17-20%. There are several analytical concerns which may play a role in this difference: the

background measurements were unusually high at m/z 61 during the campaign, and the instrument was transported and serviced several times before it was calibrated. The plurality of these concerns means that we cannot quantify any influence by isobaric compounds in the measurements. However it would appear that the effects of other compounds are not major and that the dominant signal at m/z 61 is acetic acid.

The measurements of acetic acid at Appledore Island show that its mixing ratio is elevated when the air masses originate from southern regions, with maxima in the same wind sectors as ozone maxima, and that acetic acid and CO are moderately correlated with each other. By employing an acetic acid to CO enhancement ratio of $12.1 \text{ pptv}\cdot\text{ppbv}^{-1}$ it was possible to estimate temporal trends in acetic acid on the basis of CO mixing ratios.

We conclude that PTR-MS can be used to monitor acetic acid in rural and remote atmospheres. However, further work needs to be done in order to quantify the nature of chemical interferences in different environments. Deploying online calibration systems during campaigns and the usage of high mass resolution PTR instruments will further alleviate these concerns.

4.7 Acknowledgements

We would like to thank Dr. Kevan Wyche and Dr. Paul Monks from the University of Leicester for providing detailed information about the response of their CIR-TOF-MS instrument to Acetic Acid. We would also like to thank Dr. Anita Lee of the US EPA, and Dr. Carsten Warneke of NOAA for providing clarification on their acetic acid calibration techniques.

4.8 Figures and Tables

Reference	PTR Method	Pressure (mbar)	Temp. (°C)	V Drift (Volts)	E/N (Td)	Acetic Acid Cal Method	Calibration Factor (ncps:ppbv ⁻¹)	Ratio m/z 61/43
Warneke et al. ⁸⁵	SS-PTR-MS	N/A	N/A	N/A	~120	N/A	N/A	5.7
de Gouw et al. ²⁴	SS-PTR-MS	2.4	23	700	~120	ID	8 ± 0.4	N/A
Christian et al. ⁹⁵	SS-PTR-MS	2.0	??	600	130	N/A	N/A	2.3
Hartungen et al. ⁹⁸	SS-PTR-MS	2.0	60	600	138	N/A	N/A	0.9
Lee et al. ²¹	HS-PTR-MS	2	??	600	120	TB	N/A	N/A
Malikania et al. ²⁸	HS-PTR-MS	1.8–2.2	60–30	580*	110	HS	N/A	0.04
Wyche et al. ⁸⁴	CIR-TOF-MS	6–9	40	†	90–140	PT	45.95 ± 1.38 (Low E/N) [†] 17.42 ± 0.52 (High E/N)	5.9 7.6
This work	SS-PTR-MS-1	2.0	45	600	132	PT	7.0 ± 0.3	0.9
This work	SS-PTR-MS-1	2.0	45	600	132	PT [‡]	6.9 ± 0.3	1.05
This work	HS-PTR-MS-2	2.0	45	600	132	PT	8.5 ± 0.4	1.5
This work	HS-PTR-MS-1	2.0	45	600	132	PT	10.9 ± 0.7	1.9
This work	HS-PTR-MS-1	2.0	45	530	116	PT	14.3 ± 0.8	2.9
This work	HS-PTR-MS-1	2.0	45	481	106	PT	17.9 ± 1.1	3.7
This work	HS-PTR-MS-1	2.0	45	433	95	PT	23.0 ± 1.7	4.5
This work	HS-PTR-MS-1	2.0	45	400	88	PT	30.8 ± 2.6	6.0

Table 4-1. A summary of acetic acid calibrations reported in the literature, and in this study. Key: SS-PTR-MS: Standard Sensitivity PTR-MS. HS-PTR-MS: High Sensitivity PTR-MS. CIR-TOF-MS: Chemical Ionization Time of Flight Mass Spectrometer. SS-PTR-MS-1 our groups first PTR-MS instrument, operating in standard sensitivity configuration. HS-PTR-MS-2 our groups second, high sensitivity PTR-MS. HS-PTR-MS-1, our group's first PTR-MS upgraded to high sensitivity, with modified ion source. Pressure, Temp. and V correspond to the drift tube conditions. Highlighted values are derived from other values given in the reference. E/N is in Townsend (Td). The calibration methods are coded as follows: ID: Indirect. TB: Teflon Bag. HS: Head Space. PT: Permeation Tube. Calibration factor for acetic acid is in (ncps:ppbv⁻¹), normalized to a primary ion signal of 1×10⁶ Hz. N/A means data is not available. *Drift tube voltage inferred from reported values in reference. †The CIR-TOF-MS features a ramped field strength, with a voltage that varies non-linearly across the length of the drift tube. The E/N values here are associated with the field strength at the end of the drift tube. The fragmentation ratios for CIR-TOF-MS were determined at 120 and 90 E/N, while the calibration factors were determined at 140 and 90. ‡ HzC scrubbed from sample air.

Table 4-2. Cluster and fragment distribution data obtained over a range of E/N values with PTR-MS-1 (HS). The unshaded columns are the relative strength of the first water cluster [$\text{H}_3\text{O}^+(\text{H}_2\text{O})$, m/z 37], and the second water cluster [$\text{H}_3\text{O}^+(\text{H}_2\text{O})_2$, m/z 55]. The light grey column is the fragmentation ratio of protonated acetic acid (m/z 61) to the acylium ion (m/z 43). The dark grey column is the fractional strength of each ion in the acetic acid signal (m/z 43 + m/z 61 + m/z 79) at each E/N, derived from the scan data collected over the course of the experiment. Above an E/N of 106, m/z 79 was not observed using PTR-MS-1 (HS) or PTR-MS-2 (HS).

E/N (Td)	(m/z 37) (m/z 19)	(m/z 55) (m/z 19)	(m/z 61) (m/z 43)	Fraction m/z 43	Fraction m/z 61	Fraction m/z 79
PTR-MS-1 (HS)						
88	9.69×10^{-1}	3.34×10^{-2}	5.96	0.12	0.86	3.0×10^{-2}
95	3.87×10^{-1}	4.87×10^{-3}	4.48	0.15	0.85	1.0×10^{-2}
106	1.00×10^{-1}	4.86×10^{-4}	3.66	0.18	0.82	
116	2.59×10^{-2}	4.94×10^{-5}	2.89	0.23	0.77	
132	4.67×10^{-3}	3.01×10^{-6}	1.94	0.30	0.70	
PTR-MS-1 (SS)						
132	8.69×10^{-2}	7.25×10^{-4}	0.86	0.53	0.46	5.0×10^{-3}
132 (Dry)	5.92×10^{-2}	3.61×10^{-4}	1.05	0.49	0.51	
PTR-MS-2 (HS)						
132	1.32×10^{-2}	2.05×10^{-5}	1.47	0.40	0.60	

Table 4-3. The average and standard deviation of the signal for protonated clusters in the primary ion signal in the different PTR-MS configurations used in this study.

Instrument	E/N (Td)	H ₃ O ⁺ (m/z 19) (hz ± 1σ) × 10 ⁶	H ₃ O ⁺ (H ₂ O) (m/z 37) (hz ± 1σ) × 10 ⁴	H ₃ O ⁺ (H ₂ O) ₂ (m/z 55) (hz ± 1σ)
PTR-MS-2 (HS)	132	5.150 ± 0.191	6.807 ± 3.137	105 ± 75
PTR-MS-1 (SS)	132	3.122 ± 0.131	27.047 ± 2.156	2266 ± 395
PTR-MS-1 (SS) Dry	132	3.614 ± 0.147	2.141 ± 2.916	1306 ± 396
PTR-MS-1 (HS)	88	1.647 ± 0.114	15.963 ± 9.079	55299 ± 9365
PTR-MS-1 (HS)	95	1.361 ± 0.200	5.276 ± 16.422	6632 ± 3526
PTR-MS-1 (HS)	106	1.386 ± 0.195	1.391 ± 5.872	674 ± 566
PTR-MS-1 (HS)	116	1.048 ± 0.384	0.272 ± 1.218	52 ± 47
PTR-MS-1 (HS)	132	1.082 ± 0.127	0.051 ± 0.103	3 ± 8

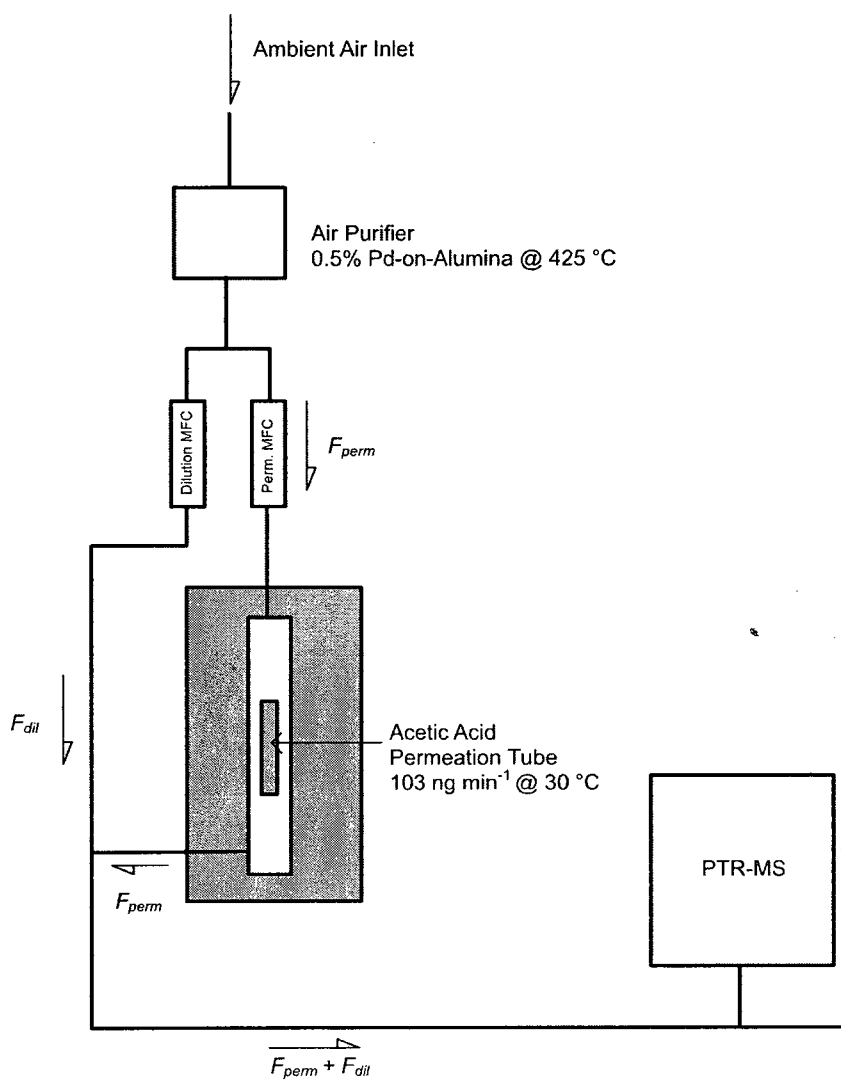


Figure 4-1. The flow of gases through the permeation oven used to calibrate the PTR-MS for measuring acetic acid.

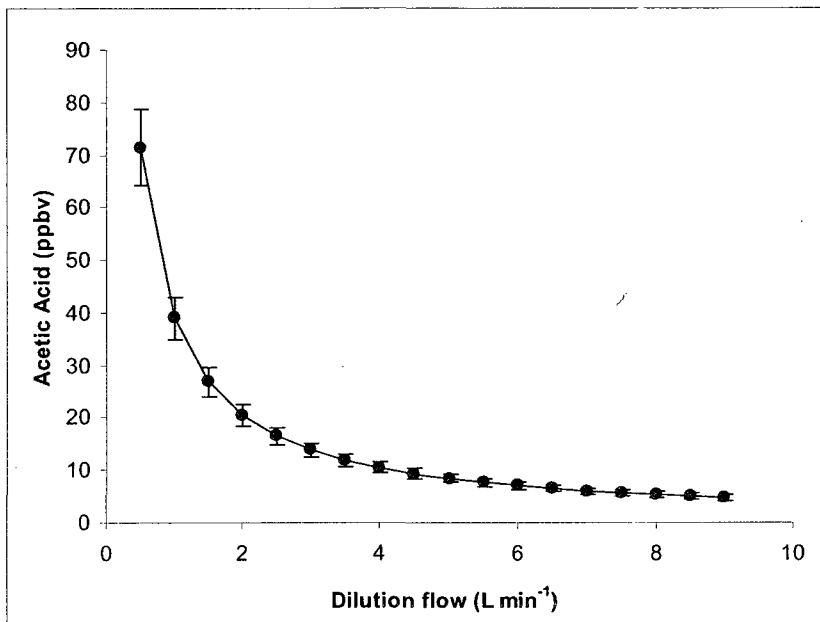


Figure 4-2. Estimated mixing ratios of acetic acid generated from a $103 \text{ ng}\cdot\text{min}^{-1}$ permeation tube, and a $100 \text{ cm}^3\cdot\text{min}^{-1}$ permeation flow.

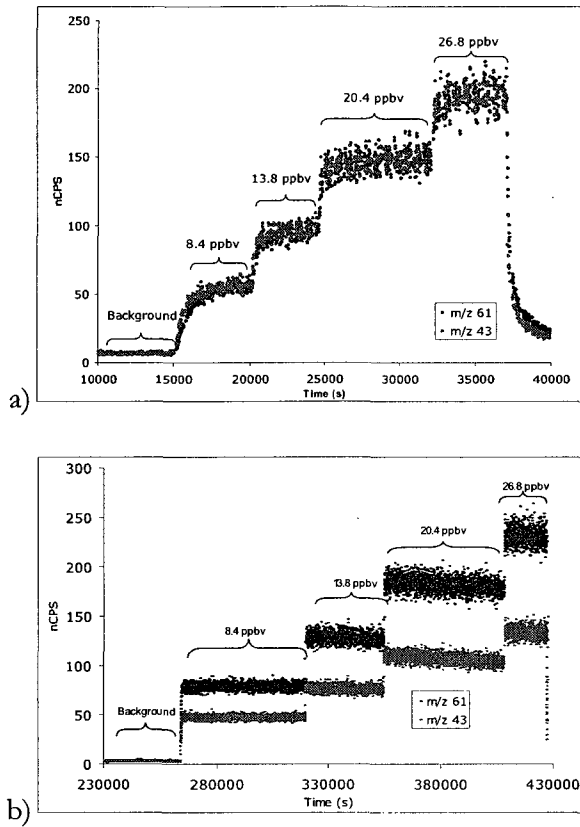


Figure 4-3. (a) A typical calibration curve for acetic acid, measured with PTR-MS-1 (SS). The regular gaps are a result of the instrument scanning the mass spectrum every few acquisition cycles. (b) The calibration curve for acetic acid measured using PTR-MS-2 (HS).

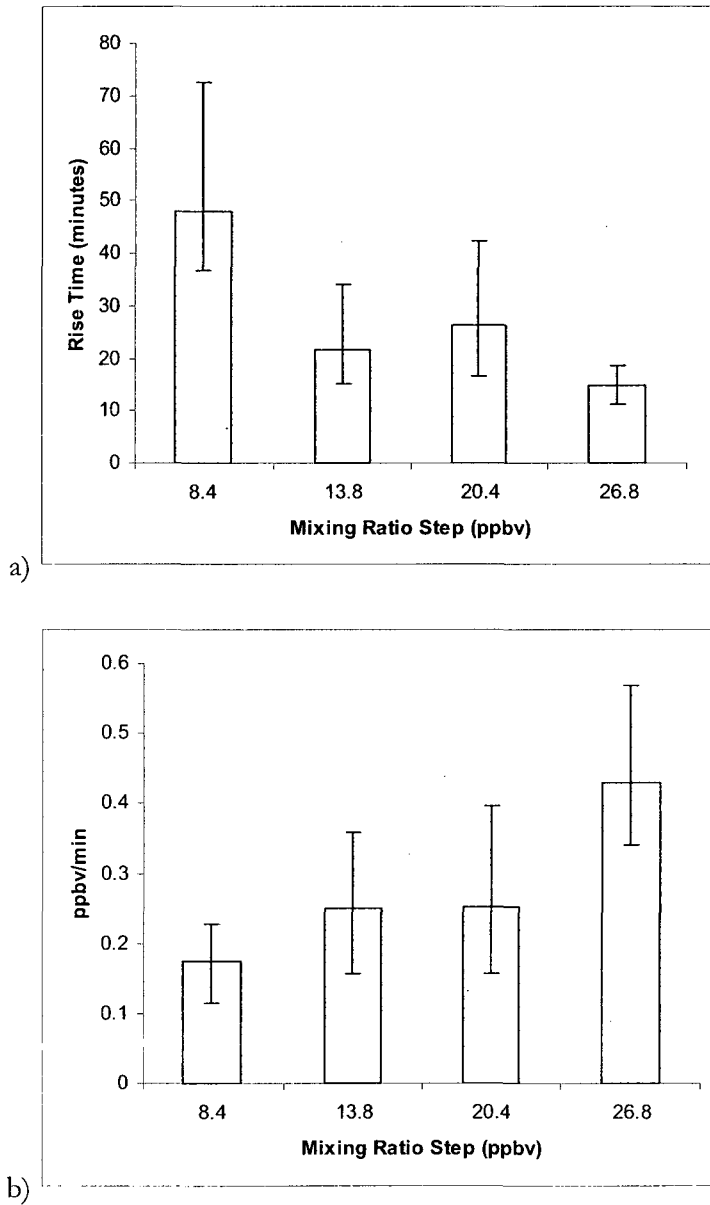


Figure 4-4. (a) Rise times (in minutes) measured with PTR-MS-1 (SS), calculated from the transition time between measurements during calibration. The mixing ratio corresponds to the rise time from the previous level to the next. Error bars represent minimum and maximum values. (b) The maximum rate of change in mixing ratio ($\text{ppbv}\cdot\text{min}^{-1}$) implied by the measurement of rise time of the instrument. Error bars correspond to the minimum and maximum values measured.

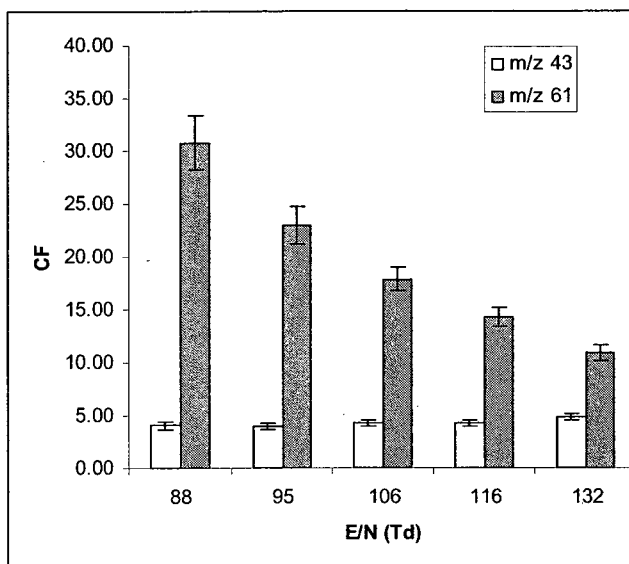


Figure 4-5. PTR-MS-1 (HS) calibration factors (CF) (in ncps·ppbv⁻¹) for acetic acid over a range of E/N ratios.

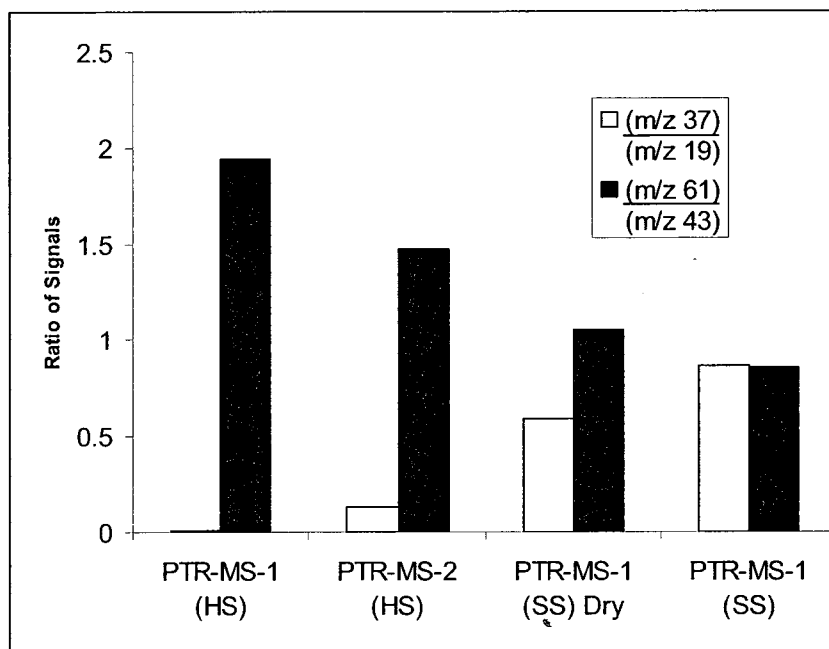


Figure 4-6. Increase in the ratio of acetic acid fragments relative to protonated acetic acid, as $H_3O^+(H_2O)$ (m/z 37) becomes more dominant in the primary ion signal. The ratios of m/z 37 to m/z 19 is multiplied by 10 for clarity.

Acetic Acid Protonation, Fragmentation, and Water Cluster Formation Pathways

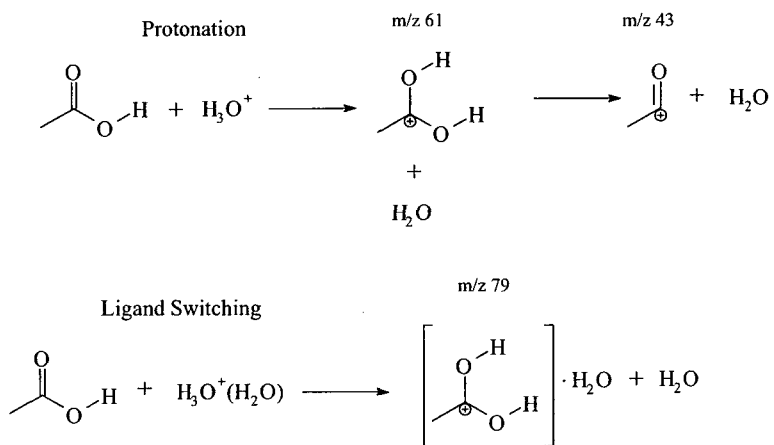


Figure 4-7. Several protonation and fragmentation pathways of acetic acid. The top pathway depicts the protonation and then decomposition pathway discussed by Mackay et al.⁸³ The bottom pathway shows a possible ligand switching pathway that forms a protonated water and acetic acid cluster that could explain the occurrence of a signal at m/z 79.

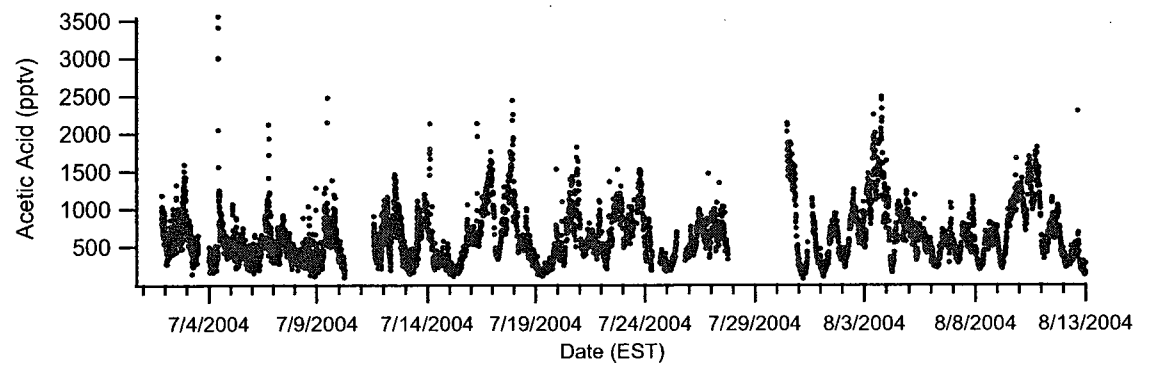


Figure 4-8. Acetic Acid measurements made by PTR-MS 2 (HS) during ICARTT.

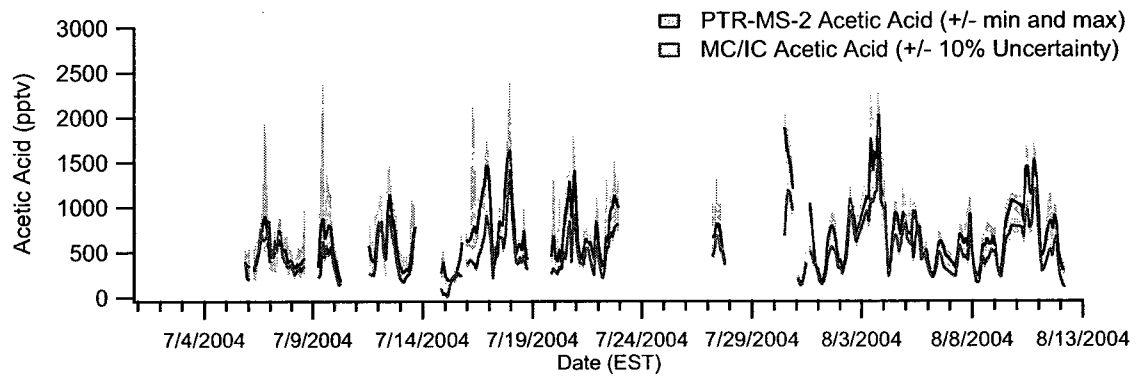


Figure 4-9. PTR-MS (blue) and MC/IC (red) data for periods where both techniques were operational. The PTR-MS results are averaged over the 2 hour time period of each MC/IC sample. The blue shading represents the minimum and maximum PTR-MS measurements over each 2 hour period.

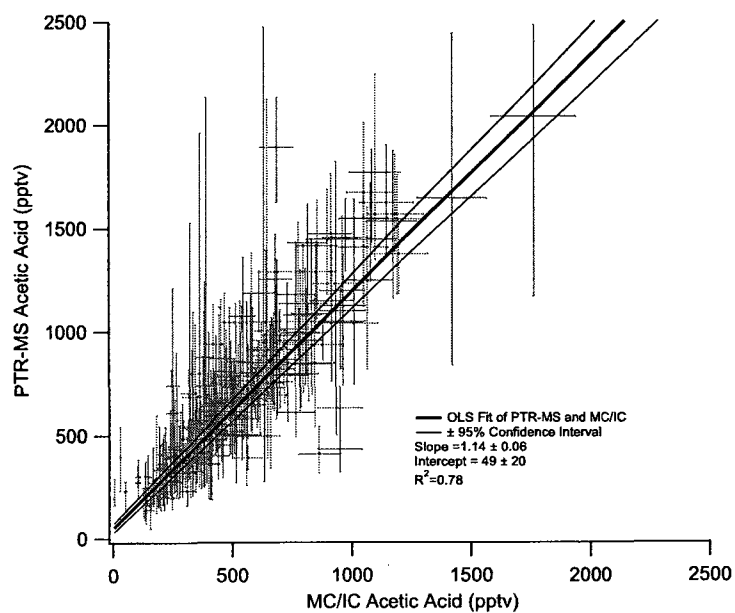


Figure 4-10. A scatter plot of the PTR-MS and MC/IC measurements of acetic acid on Appledore Island during the ICARTT campaign. The slope of PTR-MS to MC/IC data is 1.14 ± 0.06 (2σ). There is also 49 ± 20 (2σ) pptv intercept. The correlation coefficient (R^2) for the data is 0.78.

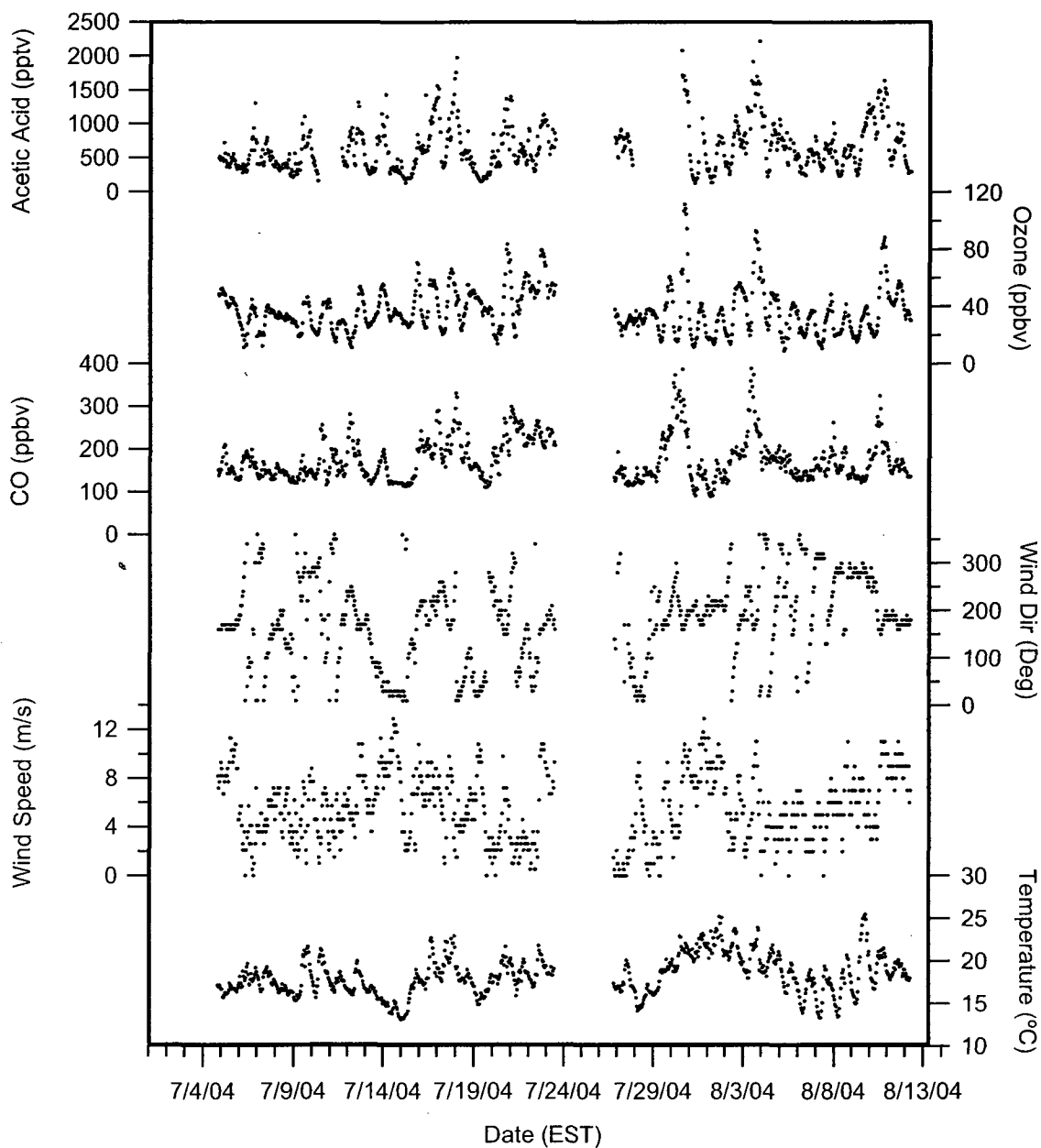


Figure 4-11. Time series data of acetic acid (measured with the PTR-MS), and CO, ozone on Appledore Island, and wind speed, wind direction (degrees), and temperature measured on Isle of Shoals at the IOSN3 Station. All data is averaged over the 1 hour interval of the reported meteorological date.

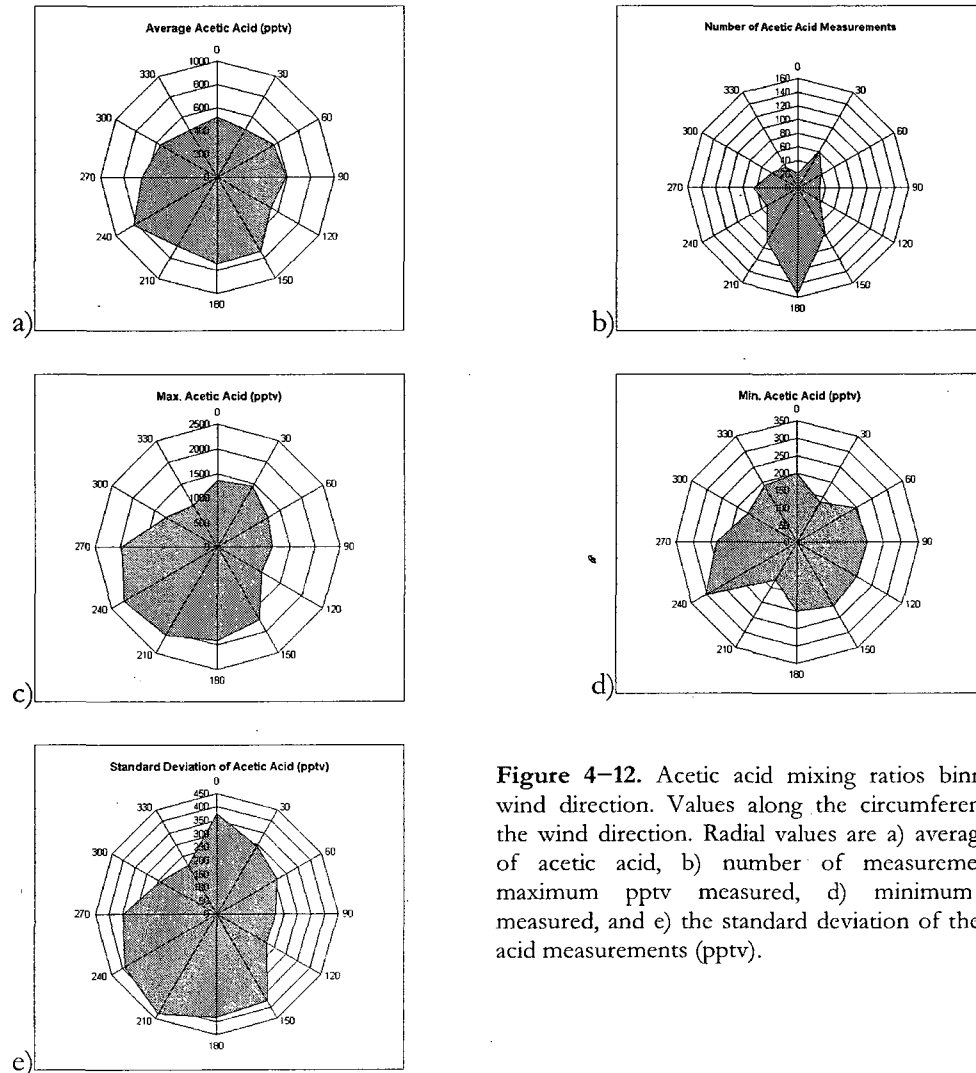


Figure 4-12. Acetic acid mixing ratios binned by wind direction. Values along the circumference are the wind direction. Radial values are a) average pptv of acetic acid, b) number of measurements c) maximum pptv measured, d) minimum pptv measured, and e) the standard deviation of the acetic acid measurements (pptv).

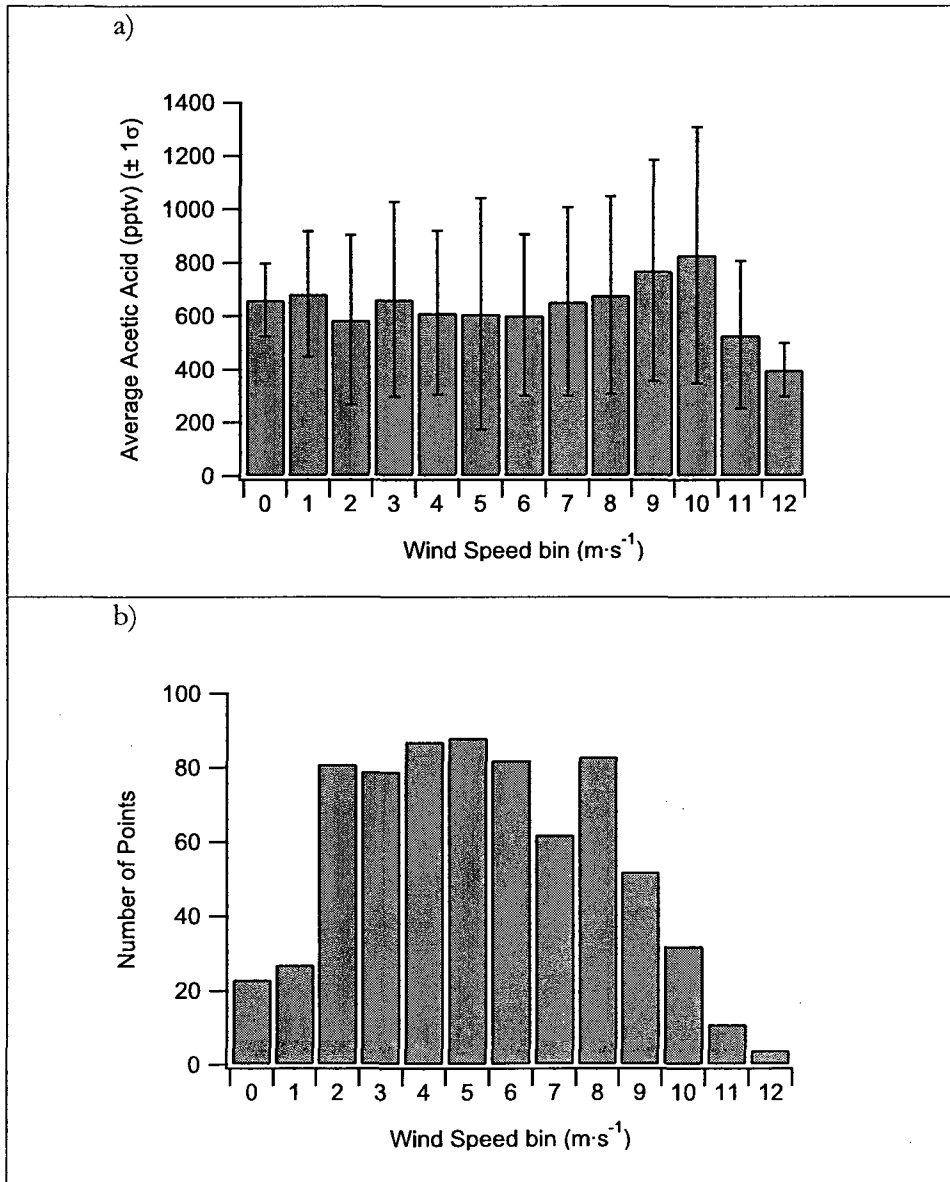


Figure 4-13. a) Acetic acid mixing ratios averaged by wind speed b) the number of points in each wind speed bin.

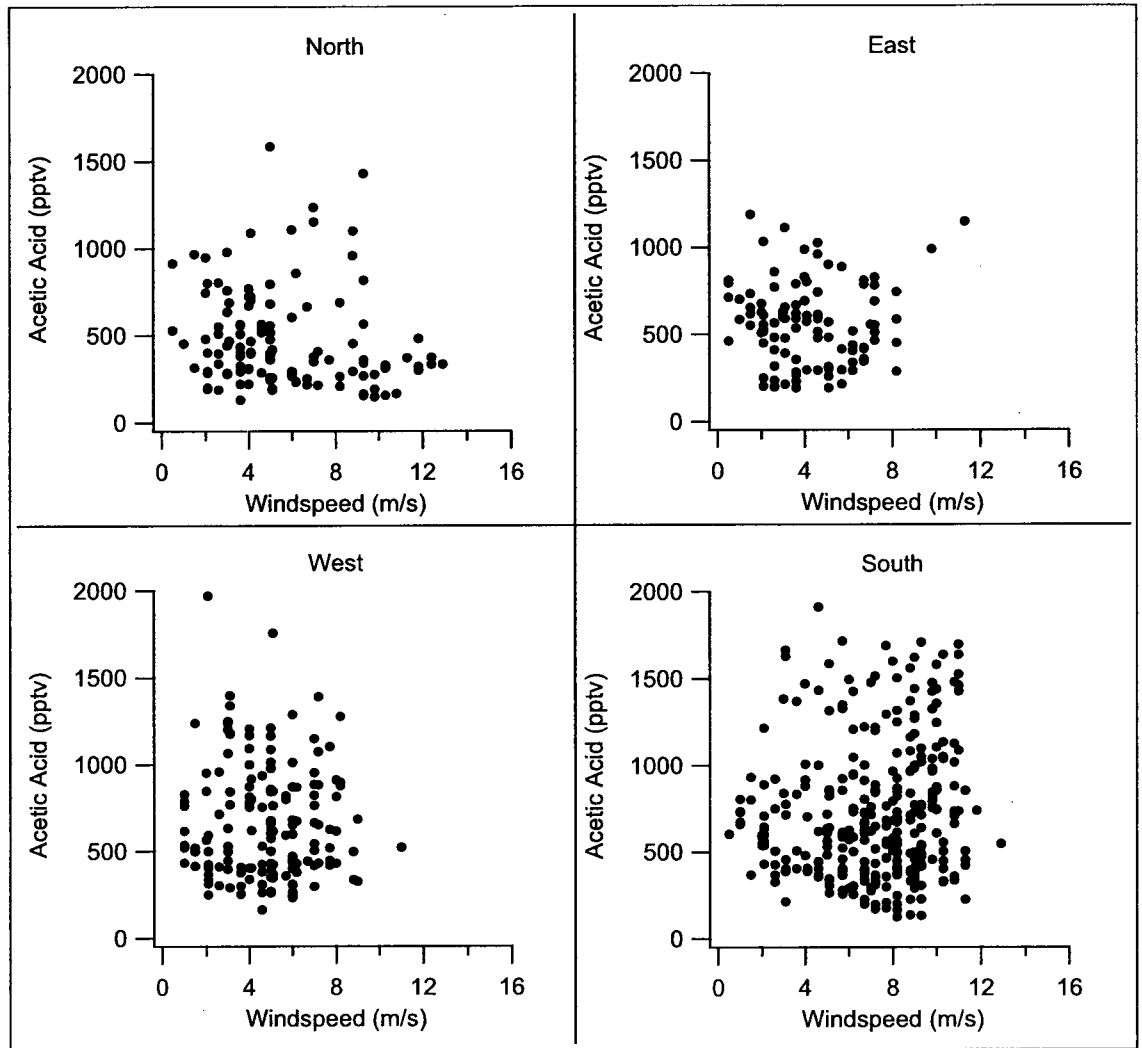


Figure 4-14. Scatter plots of acetic acid and wind speed, binned by source direction.

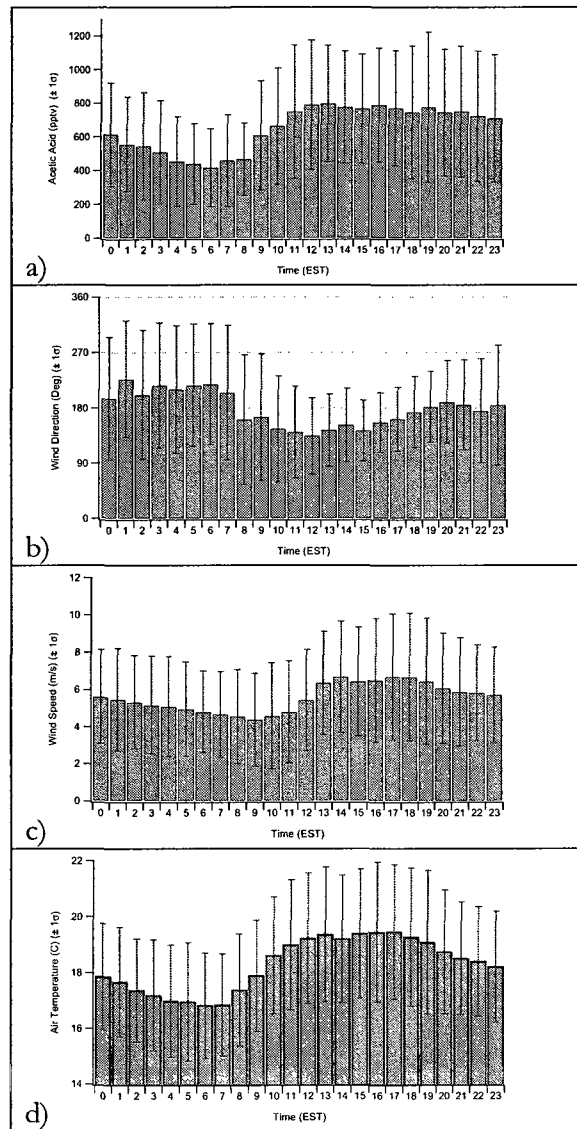


Figure 4-15. a) Acetic acid, b) wind direction c) wind speed, and d) temperature at Appledore Island binned by the time of day. Error bars represent one standard deviation in all cases. Although within the standard deviation of the measurements, the average of the acetic acid signal shows a diurnal trend that is reflected in wind speed, wind direction, and temperature data.

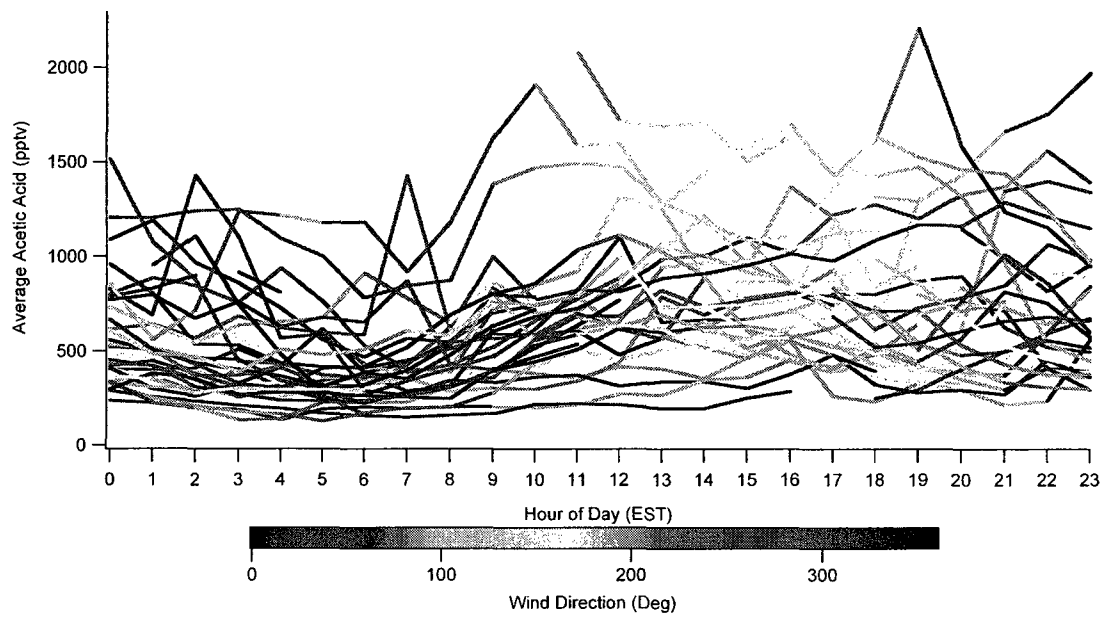
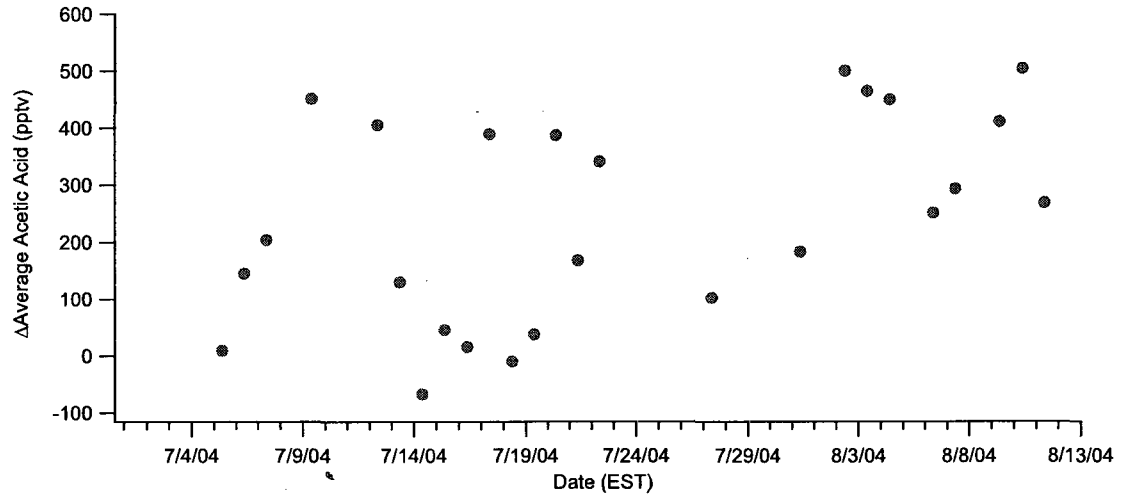


Figure 4-16. Acetic Acid mixing ratios for each day of the campaign, plotted by hour. The color coding represents wind direction, with black originating from the north, and yellow from the south. There is a daily pattern of shifting wind direction and changing acetic acid mixing ratios.

a)



b)

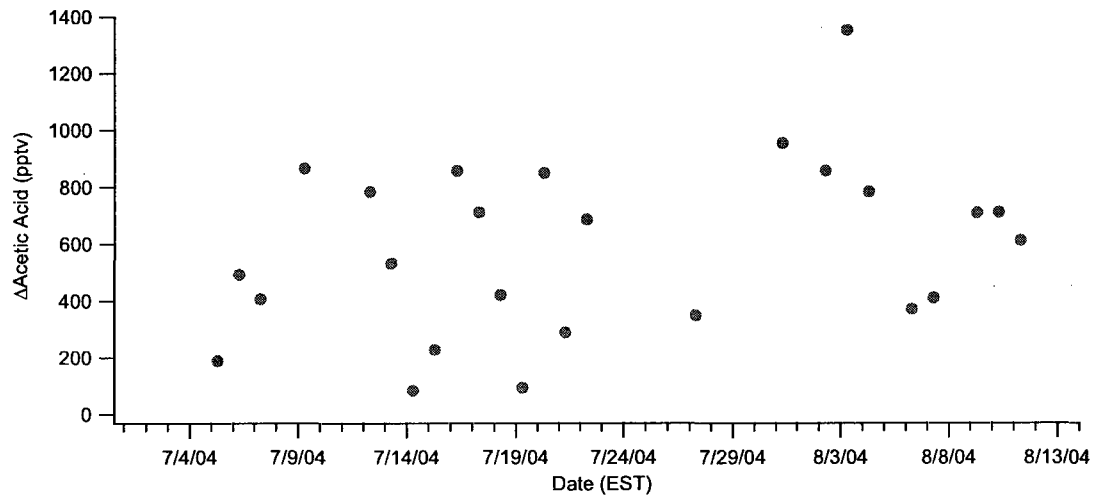


Figure 4-17. (a) The difference between the daytime average mixing ratio (0800 and 2200) and the late night average mixing ratio (between 0400 and 0800). (b) The difference between the nighttime minimum and the daylight maximum values.

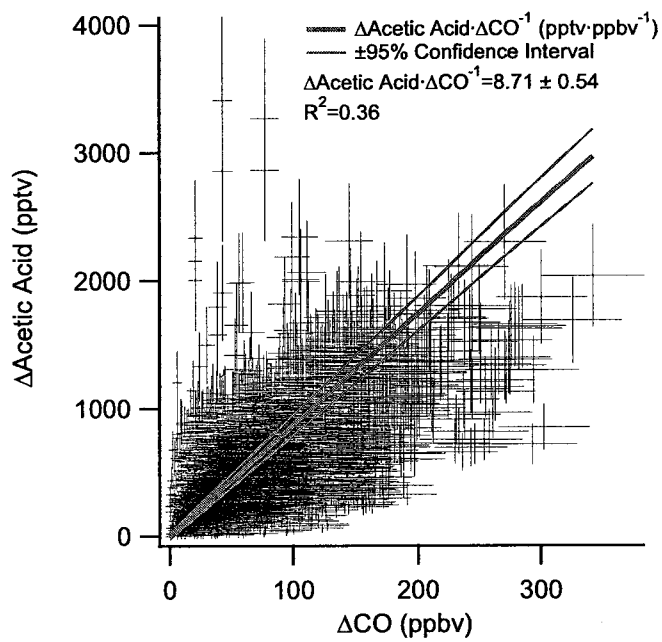


Figure 4–18. An orthogonal least squares linear regression to determine enhancement ratio of acetic acid to CO at Appledore Island during ICARTT 2004. The slope of the regression 8.71 ± 0.54 (95% confidence interval) pptv \cdot ppbv⁻¹, $R^2 = 0.36$

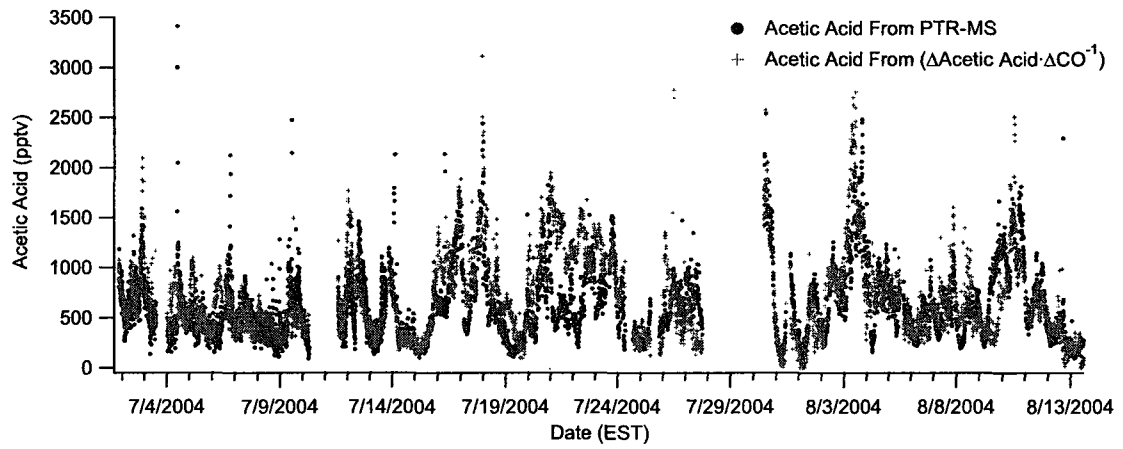


Figure 4-19. Measured acetic acid mixing ratio, compared with those predicted by the linear regression of the CO and acetic acid data set in Figure 4-18.

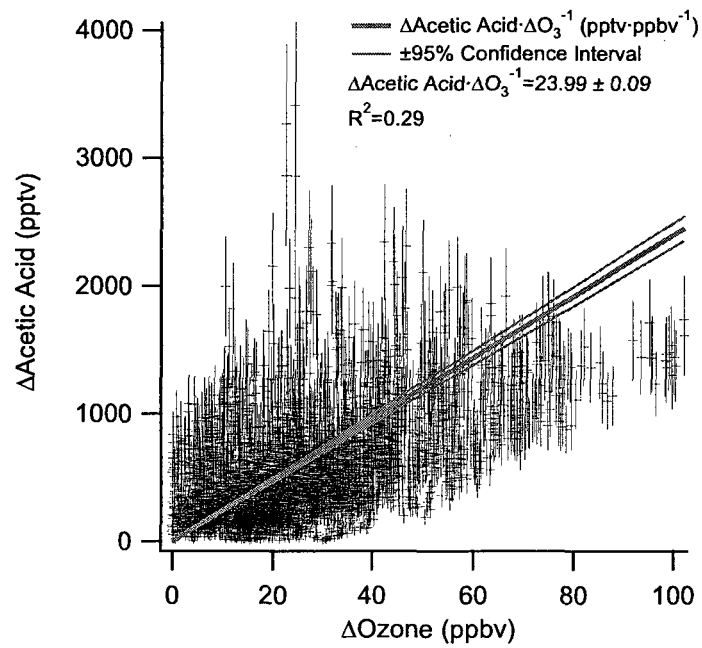


Figure 4-20. An orthogonal least squares linear regression on the enhancement of acetic acid to the enhancement of ozone measured on Appledore Island during ICARTT. The slope of the regression is 23.99 ± 0.09 (95% Confidence Interval) pptv·ppbv⁻¹ pptv acetic acid, and an $R^2=0.29$.

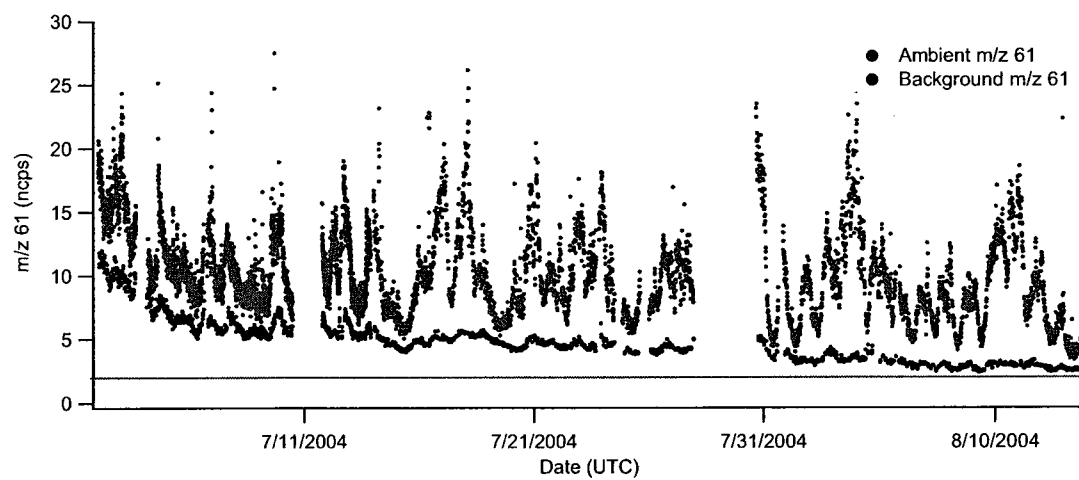


Figure 4–21. Measured signal at m/z 61 (blue) and measured background (black) during the ICARTT campaign. The red line is a horizontal guide for reference to the descending background signal over the course of the study.

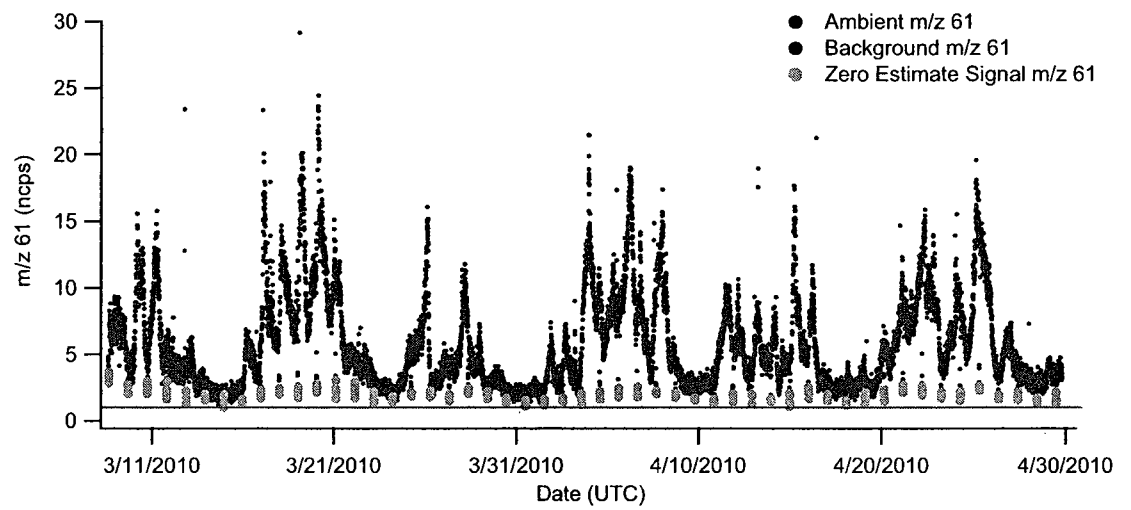


Figure 4–22. Measured ambient signal at m/z 61 (blue) and background signal (black) from our current configuration. The first 30 minutes of the background signal are discarded as the signal of acetic acid is not yet stable, the remaining background signal points that are used to determine the background are in green. The red line is a horizontal guide for reference.

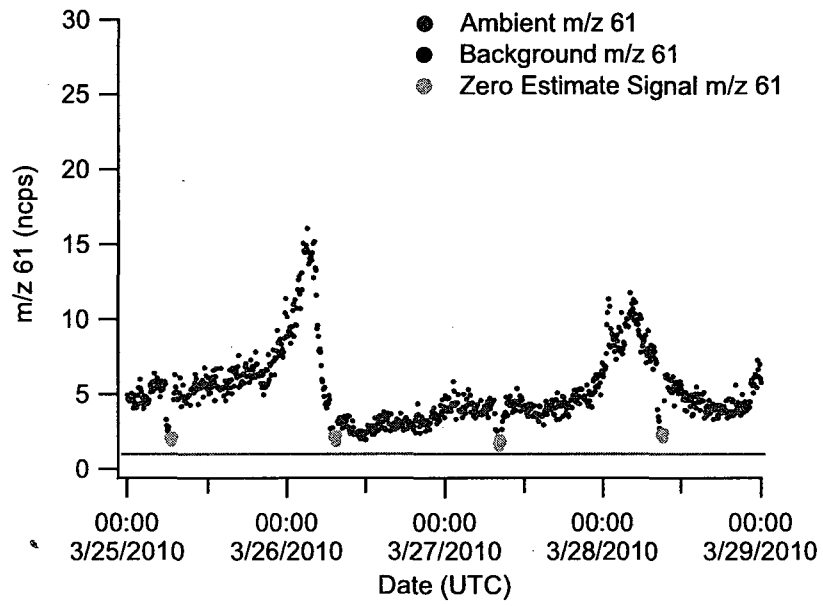


Figure 4-23. A detail view of the measurement (blue), and air sampled through the catalytic converter (black) sampled (black), and background measurements determined from the background signal (green).

CHAPTER 5 :

STORM IMPACTS ON MONOTERPENE MIXING RATIOS OBSERVED AT A RURAL SITE IN NEW HAMPSHIRE

5.1 Introduction

Monoterpenes and other volatile organic compounds (VOCs) are released by vegetation in response to various sources of stress, including heat, light, drought, physical trauma and infestation.¹²⁰⁻¹²³ They can also be released from ground litter that has fallen from trees.¹²⁰ The global budget for monoterpene emission is estimated to be 127 Tg C per year, comprising an important part of the biogenic VOC budget.³⁸ Monoterpenes readily oxidize in the presence of atmospheric oxidants (OH, O₃, NO₃, Cl), to form an array of oxygenated VOCs. These compounds can go on to nucleate into secondary organic aerosol particles or adsorb onto preexisting nuclei.^{21, 22, 124-128} The aerosol particles formed from organic compounds such as monoterpenes are thought to play an important role in controlling the radiative balance of the atmosphere.^{41, 129} Thus, considerable effort is underway to quantify global monoterpene fluxes to understand the interactions between ecosystems, climate and air quality.¹³⁰ To date, most studies have focused on quantifying fluxes from typical, healthy ecosystems, although there is increasing interest in understanding how ecosystems respond to parasitic pressures, as this could be a feedback mechanism important to predicting future climate.^{131, 132}

The goal of this chapter is to examine the impact of storm systems on ambient monoterpene levels. There is very little data available on how precipitation and intense storm events alter monoterpene emissions, although the general observation has been that storms induce monoterpene emissions.^{133,134} Monoterpene fluxes from a ponderosa pine forest have been noted to be ~130% greater than predicted as a result of precipitation events.¹³⁵ Summertime storm systems can bring intense winds and hail, which can knock branches, leaves, and needles from trees, acting as a form of mechanical stress known to increase monoterpene emissions.^{120,136} The rainfall associated with storm systems soaks the leaves and needles, which can increase monoterpene emissions in certain plant and tree species.¹³⁷

This project makes special use of the high time resolution that is a key feature of PTR-MS instruments. This high time resolution allows for observations of events that happen more quickly than can be resolved by more traditional online VOC analysis techniques based on chromatographic separations. In previous studies, the high time resolution allowed for eddy covariance flux measurements of select VOCs, and to generate high time resolution VOC measurements aboard ships and aircraft.^{20, 23, 24} The fast response and high time resolution of the PTR-MS technique are particularly valuable in this study as changes in monoterpene mixing ratios occur on the scale of minutes with the arrival of storm events.

5.2 Experimental

5.2.1 Measurements at Thompson Farm

Since 2004, atmospheric VOC measurements have been made using a PTR-MS at the University of New Hampshire (UNH) AIRMAP network monitoring site at Thompson Farm (43.1078°N, 70.99518°W). The instrument operation has been described previously.²⁶

All operational parameters have remained essentially the same, with the exception of moving the instrument: it was moved to a new building located approximately 1 km from the old measurement site in June 2009. The PTR-MS was operated with an ion source water flow rate of $11 \text{ cm}^3 \cdot \text{min}^{-1}$, a discharge current of 8 mA and a 600 V potential, giving a primary ion signal of $2\text{-}10 \times 10^6$ Hz. The ion source extraction voltages were tuned to keep the contaminant O_2^+ signal less than 1% of the primary ion signal, ensuring that the primary ionization pathway was through the proton transfer reaction with H_3O^+ . The drift tube was kept at 2.0 mbar, 600V, and 45°C , corresponding to reduced field strength of 132 Td. The quadrupole mass spectrometer was operated in single ion mode, monitoring a mass table of 47 discrete m/z channels with a dwell time 10-20 seconds per channel. The signal at m/z 137 was used to monitor the mixing ratio of monoterpene compounds, as it is not possible to speculate isobaric monoterpenes using the PTR-MS technique. Every 24 hours, the instrument switched to measure background signal by drawing ambient air through a 1.27 cm (0.5") OD, 46 cm (18") long 0.5% Pd-on-alumina bead catalytic converter held at 625°C for approximately 1 hour. A secondary standard was automatically introduced into the stream for 30 minutes after background signal determination, thereby comprising our online calibration system. The flow of the secondary standard cycles through three different flow rates over time, so that every three background/calibration periods, a three point calibration is generated. This online calibration system provides a metric of instrument response made on a daily basis, and is done in conjunction with more thorough offline calibrations done with primary standards and a standard dilution system (Apel Riemer Environmental). This 25.5 hour cycle ensures that the zero frequency does not introduce a temporal bias into the PTR-MS data stream.

Additional measurements from Thompson Farm in this analysis include ozone, NO₂, photolysis rate (jNO₂), particle number density, wind speed, wind direction, temperature and relative humidity. For 2004 to 2007, all measurements from the original Thompson Farm site were used. For 2008, the PTR-MS was still located at the original site, but jNO₂ was obtained from the new site. All other measurements were obtained from the original site. For 2009, all measurements were performed at the new field site. The data were averaged over a 5 minute time period that is approximately on the time scale on the PTR-MS dataset. Further details about these measurements can be found at <http://www.airmap.sr.unh.edu/>.

5.2.2 Determination of Storm Events

Because of the highly localized scope of intense storm events (like thunder and hail storms) and the lack of a specific instrument at Thompson Farm to determine rain and hail at high time resolution, proxy sources were used to establish points in time when intense summer storms were active over the field site. Deducing the presence of storm events at Thompson Farm was a two stage process. The United States National Climatic Data Center (NOAA NCDC) maintains a publicly accessible storm event database (<http://www4.ncdc.noaa.gov/cgi-win/wwcgi.dll?wwEvent~Storms>). This database is regional in scale and contains data on events from eyewitness sources. The database is organized by city and county, but this data does not provide explicit listings of hail and storm events over Thompson Farm because it is an unmanned station in a sparsely populated area. Storm history data was retrieved for Strafford and Rockingham counties. Events marked as “Hail”, “Thunderstorm Wind”, “Tornado”, and “Funnel Cloud” were chosen as indicators of periods in time when storms would be active over Thompson Farm. These events were reduced from a list of 228 individual events to a list of unique event days

(as events often happen concurrently across the region). This yielded a total of 37 event days between June of 2004 and September of 2009, which are listed in Table 5-1. Unfortunately, several of these storm events caused power outages at Thompson Farm, so little or no analysis was conducted for the following events: 08/20/2004, 6/20/2006, 7/28/2006, and 8/8/2008.

Precipitation data (hourly precipitation rate) was obtained from the NCDC NEXRAD Doppler radar inventory for the day of each event and 24 hours thereafter (<http://www.ncdc.noaa.gov/nexradinv/>). For this study, data from the radar site located in Boston, MA was used (callsign: KBOX). This data is available in 5-10 minute time resolution and is calculated for 1km grid squares. The radar data was manually analyzed to determine the onset of light precipitation ($0.00'' < 0.10''$ per hour), surges in precipitation rate ($> 0.10''$ per hour), duration of the surge, and cessation of precipitation. The maximum precipitation rate at Thompson Farm, the maximum rate in the area, the general direction of travel, and the relative area most affected by the storm were noted. On days where there were multiple peaks in precipitation, each peak was considered a unique event. Additionally, storms were classified as brief and compact, or part of a regional precipitation event. Compact events were a few hours in duration, easily bounded by the 48 hour data retrieval interval and feature localized heavy precipitation. Regional precipitation events often lasted longer than the 48 hour interval, and generally had lower hourly precipitation intensities, with some never going over $0.10''$ per hour over the Thompson Farm grid square. Surges were defined as the point in time where rainfall increased to over $0.10''$ per hour in the Thompson Farm grid square or over $0.25''$ per hour in three adjacent grid squares. This last condition was included because Thompson Farm frequently appears to have less precipitation in the radar signal than in surrounding grid squares. It is not apparent if this is a real difference in

precipitation rate (perhaps influenced by the open agricultural fields in the area that contrast to an otherwise wooded region) or an artifact of the radar signal retrieval. As the objective of analyzing the radar data is to determine the passage of storm events, the three square filter allows this condition to be met in the cases where storms pass over the site, but precipitation in the Thompson Farm grid square does not increase as rapidly as the surrounding areas. A summary of the storm events determined by radar analysis is listed in Table 5-2. Additionally, the distribution by year and month of unique storm events, along with the events identified by examining the radar during periods when the PTR-MS was operational are given in Table 5-3.

5.3 Analysis

Among the storm events used in this analysis, most of the storms were associated with compact, episodic systems that did not bring prolonged periods of precipitation and did not last for more than a few hours at a time. The number of storm events varied on a year-to-year basis. In 2004 (least active year), there was just one unique event day, while in 2008 (the most active year), there were 13 unique days. The majority of unique event days fall between June and August, with just 5 days occurring in September or May. On unique event days, it is common for several intense periods of precipitation to occur over Thompson Farm, interspersed with periods of little (0.00 to 0.10" per hour) or no precipitation. Unfortunately, this list of storm events cannot be considered an exhaustive analysis of storms occurring over Thompson Farm, as it is highly dependent on the NWS storm event reporting scheme, which does not explicitly monitor the exact meteorological events occurring at our site. Several possible scenarios could escape this analysis: if a localized system was active over Thompson Farm, but did not get recognized as an event in a

monitored area, that storm would not be included in this study. Similarly, more mild storms that were not severe enough to trigger a reported event are also not examined.

Each storm event identified from the radar data was examined using the trace gas mixing ratios and meteorological measurements (i.e., temperature, wind speed, relative humidity, etc.) in the context of non-storm conditions. This analysis is important because not all the storms perturbed the measured monoterpene mixing ratio. Additionally, storms tended to arrive at Thompson Farm around 00:00 UTC (2000 Local Time), which tends to also coincide with the formation of a stable nocturnal inversion layer.¹³⁸ This layer prevents surface emissions from mixing into the free troposphere, so monoterpene mixing ratios frequently build up to several parts per billion over night and rapidly drop at sunrise. By treating each storm system as a unique event, it was possible to assess the correlation of storm events and elevation in monoterpene mixing ratios. This process also led to the rejection of enhancement events that happened on the same day that storms occurred, but did not coincide with precipitation at the Thompson Farm site. This led to the elimination of a monoterpene enhancement event on June 26, 2009.

The qualitative analysis showed that the storm events could be generally categorized based on the trends of mixing ratios around the time a storm was over Thompson Farm.

Type A: These events showed a rapid increase in monoterpene mixing ratio that coincided with the passage of a storm. These increases ranged from a few hundred pptv to tens of ppbv. The mixing ratios then remained elevated for several hours. During this period of time, winds were calm ($\sim 0 \text{ m s}^{-1}$) and levels of ozone were very low ($< 10 \text{ ppbv}$ at peak monoterpene mixing ratio). Type A events happened at night or early morning, so the combination of no wind, and minimal O_3 levels indicates that there was no transport or oxidative loss pathway for monoterpenes during these

events. These events are relatively uncommon, with only 4 present in this study.

An example of a Type A event is shown in Figure 5-2.

Type B: Events of this type showed an increase in monoterpenes mixing ratios that peaked during, or soon after a storm's passage. The mixing ratio of monoterpenes then resumed a level similar to their initial values. Compared to Type A events, these events were not temporally restricted and occurred during both daylight and nighttime hours. Type B events exhibited decreasing wind speeds during rainfall, but then remain present or subsequently increased. Ozone mixing ratios were higher during these periods, so the monoterpene mixing ratios measured during the events are generally smaller, as transport and photochemical oxidation pathways were both active. These were the most common events in this study, with 20 total events. An example of a Type B event is shown in Figure 5-3.

Type C: These events showed a decrease in monoterpene mixing ratios. These events often had a small, short lived increase in monoterpenes, but then levels dropped to below pre-storm levels. These events typically coincide with high wind speeds, and thus may simply be the effect of strong mixing with free tropospheric air. There are 6 type C events in this study. An example of a Type C event is depicted in Figure 5-4.

Type D: This is used to mark storms that do not appear to have had an easily observable effect on the monoterpene mixing ratios. A total of 5 storms were systems identified using the combined NWS storm database and NEXRAD radar data; these do not appear to have perturbed monoterpene mixing ratios at Thompson Farm. An example of a Type D event is shown in Figure 5-5.

The class assignments for each event identified by radar are shown in the “Class” column of Table 5-2, and the annual distribution of event days is shown in the “Measured Event” column of Table 5-3. Out of the original 36 events identified from the radar data, 30 were considered to have perturbed monoterpene mixing ratios in connection with the storms passage (Type A, B, or C), while 5 did not; one event caused a power outage for which there were no measurements. The storms occurred over a total of 26 days out of the original 34 unique days, spanning five different summers. Four out of the five Type A events occurred after the PTR-MS had moved to the new Thompson Farm observatory. This result is likely indicative of the different surroundings at the new site. The old observatory tower is located amidst the fields of a research farm, whilst the new observatory is located in the trees with the sample inlet above the top of the forest canopy. Given the close proximity of the inlet to a source of monoterpenes, it is possible that events classified as Type B at the original Thompson Farm site could be considered Type A at the new Thompson Farm site.

In order to quantify the trends in monoterpene mixing ratios as storms pass over Thompson Farm, the mixing ratios of monoterpenes were grouped into bins that comprised the 3 hours before the onset of rainfall, the mixing ratio before, during, and after peak precipitation, and then 3 hours after cessation of precipitation. The 3 hour windows were selected to capture the general conditions before and after the event, while attempting to exclude other factors controlling monoterpene emissions. Measurements in each of these bins were averaged for each event, and the mean taken for each type group (A, B, C, and D). For periods where there was no discernable peak in rainfall, the average mixing ratio for the entire precipitation event was used instead. The average of the bins associated with each type of event is shown in Figure 5-6.

Type A events show the largest change in mixing ratio from storm passages, increasing from 1.55 before the rain to 3.35 ppbv during peak rainfall, and then decrease slightly to 3.08 ppbv three hours after rainfall ceases. The mixing ratio increases rapidly after the precipitation rate climbs over 0.10" per hour. It is worthy of noting that the average values in the bin representing the period of time between the start and the peak for Type A events are often just single measurements. The Type A event on August 11, 2009 was excluded from the bin-averaging analysis because it occurred in the middle of the night, where the nocturnal inversion layer was present and monoterpene mixing ratios were already elevated.

Type B events show much more subtle changes in mixing ratio during storm passage. The average mixing ratio three hours before precipitation is 0.43 ppbv, and peaks at 0.88 ppbv after the maximum precipitation front passes, with a final average mixing ratio for the period 3 hours after rainfall of 0.83 ppbv. The post storm signal is quite variable for Type B events, as subsequent arrival of new storms, sustained winds, or nighttime accumulation of monoterpenes can impact the average mixing ratio of the last 3 hour bin. Generally, this final value appears to be biased upwards by nighttime increases in monoterpenes.

Type C events show a mixing ratio pattern that reflects the "dip" scenario outlined above. The monoterpene average mixing ratio 3 hours before the arrival of a storm is 1.40 ppbv, at the onset of rain it drops to 1.03 ppbv, then further decreasing to 0.78 ppbv at peak precipitation, then increasing to 0.97 ppbv. For the three hours after the storm passage, the average mixing ratio was 1.00 ppbv. Compared to the beginning of Type A events, and the trends for B and D, the mixing ratios are quite high. This is not the effect of bias of a single point either, as 5 out of 6 events start between 1 and 2 ppbv and end in a distribution

ranging from 0.44 to 1.47 ppbv. Type C events are also not associated with compact, short term storms, but are related to large regional events that last for many hours to days. It has been noted elsewhere that long rain events do not seem to coincide with the same burst in monoterpene emissions that short events do, and this could be the case here as well.¹³⁵ The increased background monoterpene levels observed in Type C events may be the result of reduced transport and photochemical activity that results from cloudy, cool, calm conditions.

Type D events show very little change in monoterpene mixing ratios with storm passages. The average mixing ratio 3 hours before the storm was 0.28 ppbv, which does not change after the onset of precipitation. During periods of peak rainfall, the monoterpene mixing ratios decrease slightly to 0.27 ppbv, and then increased to 0.31 ppbv after the intense precipitation ends. After the storms cleared, the average monoterpene mixing ratio was 0.33 ppbv. The Type D event on 6/26/2009 was excluded from this analysis as the high nighttime mixing ratio of monoterpenes (6-7 ppbv range) heavily skewed the average for the remaining Type D events.

Figure 5-7 shows the average, median, minimum and maximum change in monoterpene mixing ratios for each event type. The change is defined as the difference between the average mixing ratio 3 hours before each event and the maximum during the peak period of precipitation. In comparing all types of storm events, Type A events had an average increases of 3.60 ppbv, the Type B events had a much smaller increase of 1.07 ppbv, and Type C events decreased by 0.51 ppbv.

5.3.1 Environmental Conditions Associated with Events

In order to understand the environmental factors driving the different types of monoterpene events identified, the local climate conditions surrounding the event were

examined. Climate conditions impose significant controls on ambient monoterpene mixing ratios. Emission rates are a function of temperature and can be increased due to mechanical stress on leaves. High winds can cause leaves and needles to be torn from branches, branches to break and fall from trees, and produce greater flexing than trees normally experience during clear weather. Additionally, heavy rainfall and hail can also cause leaves and needles to become detached, as well as causing impact damage to leaves that remain attached. High wind speeds are also indicative of greater advection, removing ground level monoterpenes and transporting them aloft. These factors warrant examining the climate conditions of each event type in order to get a better understanding of the controls on measured monoterpene mixing ratios.¹³⁹ The average wind speed for each type of storm event is shown in Figure 5-8, the average temperature is shown in Figure 5-9, and the average peak precipitation rate for each event type is shown in Figure 5-10.

Unfortunately, there were only sparse meteorological data available for Type A events; instruments were not functioning during two events that occurred on August 11, 2009. The data presented are for the remaining 3 Type A events; These events are characterized by higher wind speeds than the other event types until the arrival of the peak rate of precipitation. The doubling of the average wind speed from $2 \text{ m}\cdot\text{s}^{-1}$ to $4 \text{ m}\cdot\text{s}^{-1}$ is notable. After the passage of the front, Type A events have the calmest wind conditions. These major emission events also have the highest average temperatures, averaging 27.7°C before the onset of rainfall, corresponding to greater monoterpene emission activity and the highest average precipitation rate ($0.42''$ per hour). The factors combined indicate that Type A events are characterized by a period high emission activity, high mechanical stress from wind and precipitation, followed by calm conditions where monoterpenes can accumulate in the nocturnal inversion layer.

In contrast, Type B events have slower, less variable wind speeds (1.3 to $1.5 \text{ m}\cdot\text{s}^{-1}$) before and during peak rainfall then subside to less than $1 \text{ m}\cdot\text{s}^{-1}$ after the passage of the storm. The temperature trend was very similar to Type A events, but the average temperatures were 2-4 degrees cooler in every stage of event passage resulting in lower emission rates. Similarly, the average maximum precipitation rate was $0.25''$ per hour. In compared to Type A events, Type B events exhibited lower stresses and emission activity, and greater mixing, indicating that measured monoterpene mixing ratios were smaller than those observed during the Type A events. Worth noting is that several individual Type B events had the potential to be Type A events: both high temperature and precipitation rates were present, but persistent winds after the passage of the storm likely caused the released monoterpenes to be transported away from the measurement site.

Type C events showed very low, consistent wind speeds throughout each storms passage. Wind speeds dropped slightly from 1.0 - $1.3 \text{ m}\cdot\text{s}^{-1}$ to $0.8 \text{ m}\cdot\text{s}^{-1}$ after peak precipitation, but 3 hours after the precipitation ended, wind speeds were similar to those before the storm. The temperature decreased from $22.0 \text{ }^{\circ}\text{C}$ to 19.5 - $20.2 \text{ }^{\circ}\text{C}$ as the storms passed, a trend similar to that of Type B events, although the temperatures were more stable. Type C events experienced an average of $0.23''$ per hour, slightly less than type B and almost half that of Type A. The decreases observed in monoterpene mixing ratios and their root causes used to characterize Type C events from others is not reflected well in the averages used to quantitatively characterize events. However, Type C events are quite different from other events because of their consistent temperatures, low wind speeds, and moderate monoterpene mixing ratios ($\sim 1 \text{ ppbv}$). Compared to Type A and B events, Type C events do not have strong stress factors present causing enhanced monoterpene emissions, but the

low wind speeds limit the rate of ventilation, resulting in elevated mixing ratios during the course of the event.

Type D events feature consistently higher wind speeds in the range of 1.9 to 2.4 m·s⁻¹, and the lowest temperatures, starting at 21.0 °C and dropping to 17.4 °C as each event progressed. Additionally, the average maximum precipitation rate for storms in this class was the lowest at 0.15” per hour. These values indicate that type D events occur when there was low emission activity and mechanical stress, but high rates of advection keeping *monoterpenes from building up in the area around Thompson Farm.*

In a broader scope, this analysis shows that the large, enduring monoterpene events (Type A) occur when a combination of environmental and stress factors occur to stimulate intense monoterpene emission, then minimal transport allows for these high mixing ratios to persist for a long period of time. In contrast, Type D events lack conditions of high temperature and mechanical stress and have high rates of advection, meaning that monoterpenes do not have the opportunity to build up at Thompson Farm. Type B and C events exist on a spectrum between Type A and D, where different combinations of emission factors and mixing lead to short increases in monoterpene mixing ratios but mixing and dilution processes ultimately remove them from the area.

The observed monoterpene increases in connection with storm events leads to the question of the mass of monoterpenes released into the atmosphere. The Type A events may be used to provide an upper limit, as the strong emission is coupled with low amounts of transport and mixing. For the event that occurred at 23:41 UTC on August 21st, 2009, a cell of intense precipitation that originated in the area of Derry, NH delivered a sudden hail storm Thompson Farm. During the storm, the monoterpene levels climbed to an average of 6.56 ppbv, which persisted until day break. The wind speed dropped to 0.1 m·s⁻¹ after the

start of the peak precipitation, and remained relatively constant with an average speed of $0.07 \text{ m}\cdot\text{s}^{-1}$. These calm conditions are taken to indicate the formation of a stable inversion layer. If the majority of the monoterpenes emitted as a result of the storm were captured in the boundary layer, the mass of entrained monoterpenes is given by the following expression:

Equation 35: $\Delta M = \Delta C \cdot V$

where ΔM is the total mass of monoterpenes aloft, ΔC is the increase in monoterpene concentration ($\text{g}\cdot\text{m}^{-3}$), and V is the volume of the air mass over the storm track. In this part of New England, the boundary layer height is generally between 75 and 125 meters.¹³⁸ For this analysis 75 meters is taken as a lower limit of the boundary layer height, this value could be larger (500-1000 meters) as storm passage increases mixing.¹⁰⁹ Since ΔM scales with boundary layer height, it is possible for the mass of monoterpenes emitted to be much greater than calculated here. It is assumed that the monoterpene emissions were equivalent for the entire 50 km long, 5 km wide track between Derry, New Hampshire and where the storm left land over Kennebunk, Maine, yielding an area of $2.5 \times 10^8 \text{ m}^2$, and a volume (V) of $1.9 \times 10^{10} \text{ m}^3$. During this event, the concentration of monoterpenes changed from $5.4 \times 10^{-6} \text{ g}\cdot\text{m}^{-3}$ to $3.64 \times 10^{-5} \text{ g}\cdot\text{m}^{-3}$, yielding an increase of $3.1 \times 10^{-5} \text{ g}\cdot\text{m}^{-3}$. This yields a mass (M) of 580 kg of monoterpenes released in a single storm event, or $2.3 \times 10^{-3} \text{ g}\cdot\text{m}^{-2}$ in the storm's path. It took 32 minutes from the start of the storm for mixing ratios to reach these values. The emission rate is then $4260 \text{ g}\cdot\text{km}^{-2}\cdot\text{hr}^{-1}$, or $2.1 \times 10^{11} \text{ molec m}^{-2}\cdot\text{s}^{-1}$. The results of similar analysis for the other Type A events are listed in Table 5-4. It should be noted that many of the values in this table are very conservative: emissions scale linearly with boundary layer height and storm area. Direct measurements of vertical wind speeds and night time

boundary layer heights would help constrain these otherwise rudimentary estimates. The degree of impact could also vary in different areas which a storm has passed over, as precipitation rates, wind speed, and forest composition change along its path. This is exemplified by the estimation for 8/11/2009 (Event 19), where only the edge of the storm passed over Thompson Farm. Also of note, this method of estimation does not account for monoterpenes advected aloft during the period when winds were not calm.

Monoterpenes released into the atmosphere could be reacting to form aerosols or condensing onto preexisting nuclei. The PTR-MS measurements do not provide any information about the relative amounts of speciated monoterpenes released during storm events. However, an approximation can be made by generalizing the data from laboratory studies of SOA yield from photochemical oxidation of monoterpenes. The mass yield of SOA falls between 0.5% and 58%, here 25% and is taken as a typical value.²² If the products of oxidation form spherical accumulation mode particles (diameter of 0.25 μm),¹⁴⁰ with a density of 1.25 $\text{g}\cdot\text{cm}^{-3}$,^{21,22} then there is potential to increase the number of aerosol particles by 58 to 1184 cm^{-3} during the Type A events examined in this study (Table 5-4). Given that aerosol number densities are typically in range of $\sim 1000\text{-}8000\text{ cm}^{-3}$ in rural areas,¹⁴¹ this could be an unaccounted for source of SOA. Unfortunately, it is not possible to directly quantify the aerosol formed during these events using the available particle number density data, as rainout is removing particles from the atmosphere at the same time monoterpenes are being released. Without size and composition data, it is not possible to tell if the aerosol levels observed after the storm contain SOA resulting from enhanced monoterpene emissions and oxidation. Additional data on aerosol properties during storm events might elucidate whether enhanced monoterpenes mixing ratios result in formation of SOA and, if

so, whether new particle formation occurs or monoterpene oxidation results in growth of existing particles.

5.4 Discussion

Reviewing the quantitative analysis of the initial typing method, it would seem plausible to reclassify the events on the basis of different environmental factors that control monoterpene mixing ratios. A more important goal would be to synthesize a method of estimating storm induced monoterpene emissions on the basis of the environmental factors that storms change, such as temperature, humidity, and light, as well as the sources of stress that accompany them. These factors would allow biogenic emissions models like MEGAN (<http://acd.ucar.edu/~guenther/MEGAN/MEGAN.htm>), and BEIS (<http://www.epa.gov/asmdnerl/biogen.html>) to better reflect actual emissions scenarios that deviate from calm weather conditions. Injection of additional monoterpenes into the free troposphere as a result of storms may help explain enhanced levels of secondary organic aerosol observed in other studies.⁴⁰

The estimates of storm induced emissions presented here are on the order of, and usually much larger than the estimated emissions rates of MEGAN 2.02 and BIES 3.0 during July in New England ($150\text{-}300\text{ g}\cdot\text{km}^{-2}\cdot\text{hr}^{-1}$).¹⁴² In comparison, the values obtained from Type A events range from $160\text{-}4250\text{ g}\cdot\text{km}^{-2}\cdot\text{hr}^{-1}$. Given that most events (Type B) coincide with high winds that may cause compounds to be advected into the free troposphere, storm systems could be serving as a mechanism for drawing monoterpenes into the troposphere, where they could then oxidize and form SOA or condense on preexisting particles. This is particularly important as the frequency and intensity of severe

thunderstorms is predicted to increase over time, with an additional two strong event days per year by the end of the century.^{42,43}

5.5 Conclusions

A total of 34 unique event days between May 2004 and October 2009 were isolated using the NWS database of severe storm events. The NEXRAD radar data for each of these days was used to determine a list of 29 event days where measurements were active at Thompson Farm. These events were inspected and categorized on the basis of temporal variation of monoterpene mixing ratios. Events are classified as Type A (increase in mixing ratio and long residence time), Type B (increase in mixing ratio during storm, but short residence), Type C (small decrease in mixing ratio with passage of storm), and Type D (no apparent change). Comparing various meteorological factors, it appears that Type A events tended to be observed at the new Thompson Farm site and coincided with the formation of a stable nocturnal boundary layer. Type B events, in contrast, typically do not show the formation of a stable boundary layer, and thus their mixing ratios quickly drop due to mixing and dilution. It is also possible that some or all of the Type B events are the same as Type A events, but the levels of monoterpene levels observed were reduced at the old Thompson Farm site compared to the new observatory. Type C events generally coincided with the passage of intense precipitation and bursts of wind during an otherwise long, steady rain event, and Type D events featured high winds that kept the air mass at the measurement site well mixed. Overall, monoterpene mixing ratios increased by 31% on average when a storm passed through the area, with much larger increases for Type A and Type B events. Using Type A events and accessing the storm impact provided by the radar data, it is estimated that storms cause a rate of monoterpene emissions in the range of 160-4250 g·km⁻²·hr⁻¹. Further

measurements of monoterpene mixing ratios at the new Thompson Farm site should help elucidate whether the difference in proximity to the forest changes the frequency of occurrences for Type A events.

Analyzing current monoterpene flux data may show that there is already a wealth of information available, but currently unexamined on this topic. Performing more flux measurements in areas impacted by storm events should help determine the impact of storms on monoterpene emissions. It would be particularly useful to have speciated monoterpene data in order to better predict potential SOA yield. Measurement of aerosol size and composition would help elucidate the amount of aerosol actually formed. To address the challenge of storm frequency to measuring induced emissions, it is conceivable to simulate rain events over flux measurement sites using forest fire suppression aircraft. Airborne measurement of biogenic VOCs around the base of storms may also yield information about the amounts of monoterpenes and SOA advected aloft as a result of monoterpene emissions. By increasing our understanding of this topic, we can determine whether storm induced monoterpenes could be a pathway for formation of aerosol in the troposphere.

5.6 Figures and Tables

Table 5-1. Locations and approximate times of the unique storm events in Strafford and Rockingham Counties in southern New Hampshire obtained from the NWS Event Database.

Location or County	Date and Time (EST)
Hampton Falls	8/20/04 20:30
Lee	6/8/05 17:45
Northwood	7/14/05 14:40
Barrington	7/22/05 17:57
Farmington	7/27/05 15:50
Hampton Falls	5/21/06 16:45
Milton	6/20/06 19:20
Durham	7/18/06 16:55
Exeter	7/28/06 16:35
Deerfield	8/2/06 16:00
Milton	9/24/06 13:30
Windham	5/10/07 16:35
Candia	6/2/07 16:10
Londonderry	6/5/07 13:05
New Durham	7/6/07 13:46
Stratham	9/8/07 15:30
Milton	9/27/07 7:00
Epping	6/20/08 14:30
Durham	6/22/08 13:05
Londonderry	6/23/08 14:45
Londonderry	6/24/08 14:15
Derry	6/27/08 14:59
Windham	6/29/08 16:33
Windham	7/2/08 13:05
Towles Corner	7/3/08 17:45
Strafford	7/18/08 16:52
Rochester	7/19/08 14:58
Candia	7/24/08 10:35
Deerfield	7/31/08 17:35
Londonderry	8/8/08 16:15
Londonderry	8/10/08 14:50
Millville	8/16/08 13:36
Deerfield	6/26/09 13:12
Stratham	8/11/09 7:25
South Danville	8/21/09 18:50
Newmarket	8/22/09 11:53

Table 5-2. Storm events at Thompson Farm, identified by using radar. All times are given in UTC. (EDST=UTC-4 hours). Start Precip is the time at which the radar first detected rain, Start Peak is when the rate of precipitation increased over 0.10" per hour. Stop is when the peak dropped below 0.10" per hour. Stop precip is the last radar measurement that showed precipitation. Max TF is the maximum rate of precipitation (in inches per hour), Max Map is the maximum rate of precipitation in the area. Travel is the direction the storms were going, and # is the event number.*No rainfall detected over TF, but intense precipitation was measured during peak in adjacent pixels. **Power lost during event.

Class	Start Precip.	Start Peak	Stop Peak	Stop Precip.	Max TF	Max Map	#	Travel	Disc.
b	6/8/05 22:35	6/8/05 23:09	6/9/05 0:09	6/9/05 4:29	0.50-0.75	1.25-1.50	0	SE	Compact
a	7/14/05 20:12	7/14/05 20:29	7/14/05 21:24	7/14/05 22:15	0.25-0.50	1.25-1.50	1	SE	Compact
b	7/22/05 23:09	7/22/05 23:45	7/23/05 0:36	7/23/05 0:45	0.10-0.25	1.50-1.50	2	SE	Compact
c	7/23/05 1:47			7/23/05 3:59	0.10-0.25	0.25-0.50	3	SE	Regional
b	7/27/05 21:31	7/27/05 22:05	7/27/05 22:35	7/28/05 1:55	0.10-0.25	1.50-1.75	4	SE	Compact
b	5/21/06 22:41			5/22/06 1:13	0.00-0.10	0.25-0.50	5	NE	Regional
b	8/2/06 21:24	8/2/06 21:33	8/2/06 22:28	8/2/06 23:43	0.10-0.25	0.50-0.75	20	E	Compact
d	9/24/06 18:49			9/24/06 20:03	0.00-0.10	0.25-0.50	21	E	Regional
b	5/11/07 12:35	5/11/07 12:44	5/11/07 14:33	5/11/07 16:47	0.75-1.00	1.25-1.50	22	NE	Compact
b	6/2/07 23:56	6/3/07 0:32	6/3/07 1:06	6/3/07 1:19	0.00-0.10	0.50-0.75	23	E	Regional
d	6/4/07 16:58	6/4/07 19:27	6/4/07 20:54	6/4/07 21:33	0.25-0.50	0.25-0.50	24	N	Regional
c	9/9/07 8:19			9/9/07 9:51	0.10-0.25	0.25-0.50	25	NE	Regional
b	9/9/07 9:51	9/9/07 11:12	9/9/07 11:59	9/9/07 12:16	0.10-0.25	0.25-0.50	26	NE	Regional
b	9/9/07 15:15	9/9/07 15:43	9/9/07 16:41	9/9/07 17:27	0.10-0.25	0.10-0.25	27	NE	Regional
b	6/20/08 18:59	6/20/08 19:40	6/20/08 20:50	6/20/08 20:54	0.50-0.75	1.25-1.50	6	NE	Compact
b	6/22/08 17:55	6/22/08 18:57	6/22/08 19:48	6/22/08 22:24	0.10-0.25	1.25-1.50	7	N	Regional
b	6/23/08 17:59	6/23/08 20:25	6/23/08 22:26	6/23/08 22:54	0.50-0.75	1.50-1.75	8	NE	Regional
b	6/23/08 17:59	6/23/08 19:10	6/23/08 20:05	6/23/08 20:05	0.10-0.25	0.25-0.50	28	NE	Compact
b	6/23/08 20:05	6/23/08 20:14	6/23/08 22:26	6/23/08 22:50	0.50-0.75	1.50-1.75	29	NE	Compact
d	6/24/08 20:16			6/24/08 22:00	0.00-0.10	0.25-0.50	30	NE	Compact
b	*	6/27/08 19:06	6/27/08 19:48	*	0.00	0.50-0.75	31	E	Compact
b	6/29/08 21:39	6/29/08 21:52	6/29/08 23:24	6/30/08 0:38	0.10-0.25	0.50-0.75	32	NE	Compact
b	6/30/08 7:34			6/30/08 9:00	0.00-0.10	0.25-0.50	33	NE	Regional
c	7/3/08 22:07			EP	0.00-0.10	0.00-0.10	9	NE	Regional
b	7/18/08 0:00	7/18/08 22:30	7/18/08 23:54	7/19/08 0:04	0.75-1.00	2.25-2.50	10	SE	Compact
c	7/19/08 0:41	7/19/08 1:17	7/19/08 2:08	7/19/08 2:55	0.10-0.25	1.00-1.25	11	E	Compact
c	7/19/08 6:09	7/19/08 6:47	7/19/08 7:19	7/19/08 7:49	0.10-0.25	0.75-1.00	12	NE	Regional
**	7/19/08 21:41	7/19/08 23:28		EP	0.25-0.50	0.25-0.50	13	SE	Compact
c	7/24/08 12:07	7/24/08 13:33	7/24/08 15:19	7/24/08 15:43	1.00-1.25	1.25-1.75	14	N	Compact
d	7/24/08 16:43	7/24/08 17:00	7/24/08 18:51	EP	0.50-0.75	0.75-1.00	15	NE	Compact
b	7/31/08 20:39	7/31/08 21:46	8/1/08 0:17	8/1/08 0:45	0.75-1.00	2.25-2.50	16	NE	Compact
d	6/26/09 9:19			6/26/09 10:44	0.00-0.10	0.75-1.00	17	E	Compact
a	8/11/09 11:33	8/11/09 12:16	8/11/09 13:29	8/11/09 13:59	0.50-0.75	2.25-2.50	18	SE	Compact
a	8/11/09 21:50			8/12/09 0:00	0.10-0.25	1.00-1.25	19	SE	Compact
a	8/21/09 23:41	8/21/09 23:47	8/22/09 0:51	8/22/09 1:59	0.50-0.75	0.75-1.00	34	NE	Compact
b	8/22/09 17:00	8/22/09 17:08	8/22/09 18:21	8/22/09 21:11	0.75-1.00	0.75-1.00	35	N	Compact

Table 5-3. Summary of storm event days, events identified by radar, and measured events (Type A, B, or C) examined in the study.

Year	Month	Event Days	Radar Events	Monoterpene Events
2004	May	0	0	0
	June	0	0	0
	July	0	0	0
Storm Days: 1 Measured Events: 0	August	1	0	0
	September	0	0	0
2005	May	0	0	0
	June	1	1	1
	July	3	4	4
Storm Days: 4 Measured Events: 5	August	0	0	0
	September	0	0	0
2006	May	1	1	1
	June	1	0	0
	July	2	0	0
Storm Days: 6 Measured Events: 2	August	1	1	1
	September	1	1	0
2007	May	1	1	1
	June	2	2	1
	July	1	0	0
Storm Days: 6 Measured Events: 5	August	0	0	0
	September	2	3	3
2008	May	0	0	0
	June	5	8	7
	July	5	8	5
Storm Days: 13 Measured Events: 12	August	3	0	0
	September	0	0	0
2009	May	0	0	0
	June	1	2	0
	July	0	0	0
Storm Days: 4 Measured Events: 5	August	3	4	5
	September	0	0	0
Total:		34	36	29

Table 5-4. Summary of estimated storm induced monoterpene emissions at Thompson Farm. The rise time is the period of time between the onset of the storm and the time when mixing ratios and wind speed stabilized. Length and width are the estimated length and width of the storm track based on precipitation intensity from the radar data. kg emitted is the estimated mass of monoterpenes released during the storm. Mass per area is the grams of monoterpenes per meter of ground area in the storm track, and the emission rate ER is expressed in (†) ($\text{molec}\cdot\text{m}^{-2}\cdot\text{s}^{-1}$) and (‡) ($\text{g}\cdot\text{km}^{-2}\cdot\text{hr}^{-1}$). The potential to form new particles (Δ , particles cm^{-3}) was calculated assuming a formation of accumulation mode particles (250 nm diameter), a density of 1.25 g/cm^3 and a mass conversion efficiency of 25%.

Date (UTC)	Event	Rise Time (sec)	Length (km)	Width (km)	Mass Emitted (kg)	Mass per Area ($\text{g}\cdot\text{m}^{-2}$)	ER†	ER‡	Δ (cm^{-3})
8/21/2009 23:49	34	1966	50	5	581	2.3×10^{-3}	2.1×10^{11}	4260	1184
7/14/2005 20:12	1	3545	30	15	402	8.9×10^{-4}	4.6×10^{10}	900	455
8/11/2009 21:50	19	5051	40	20	89	2.2×10^{-4}	8.0×10^9	160	57
8/22/2009 17:00	35	5450	50	10	460	9.2×10^{-4}	3.1×10^{10}	600	469

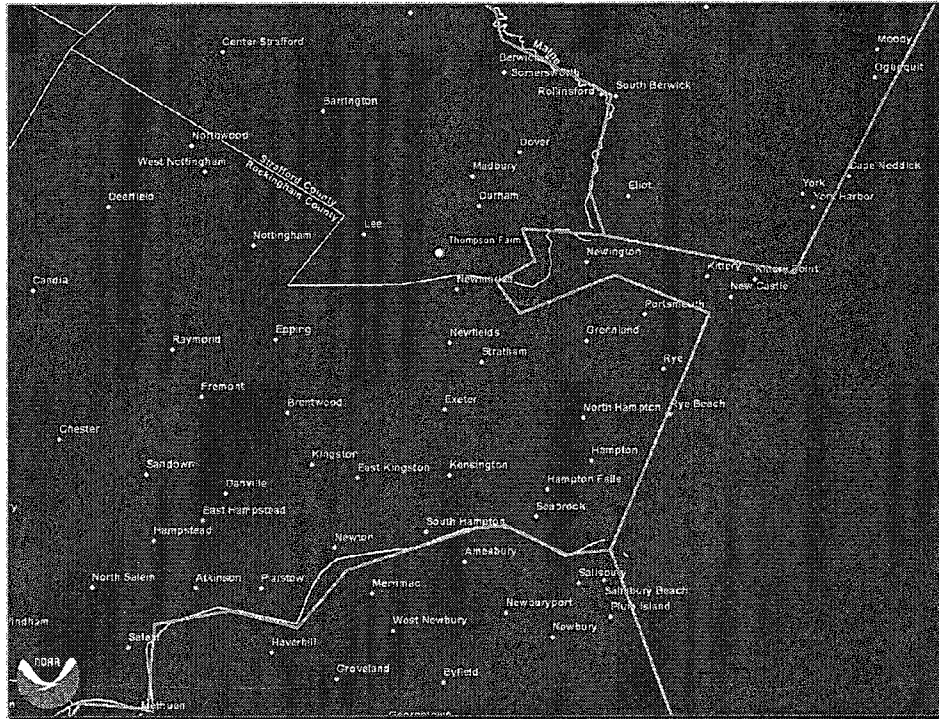


Figure 5-1. Cities and towns in the area surrounding Thompson Farm

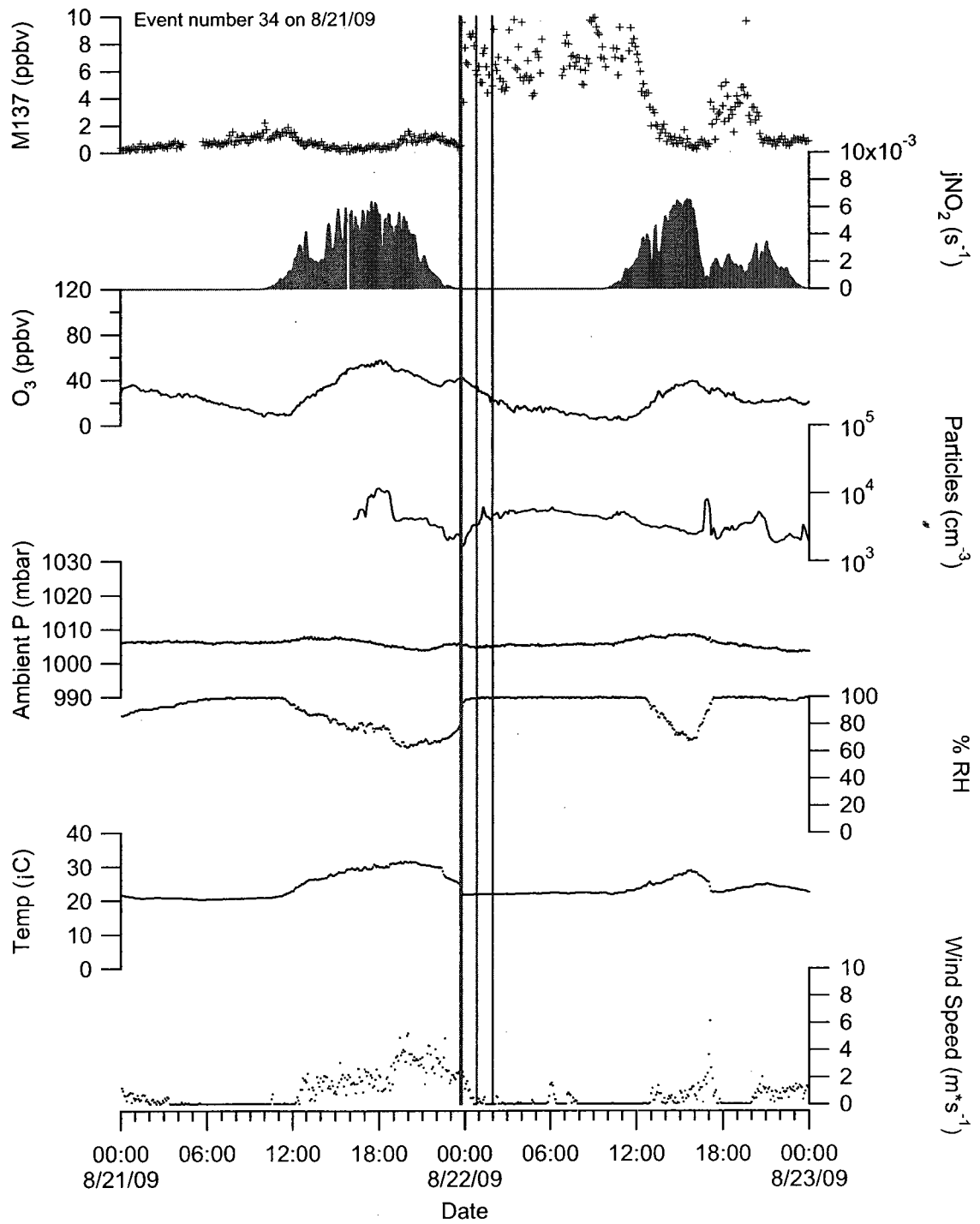


Figure 5-2. An example of a Type A event, from August 22, 2009 (UTC). Blue lines indicate the period of precipitation, while red lines indicate peak precipitation.

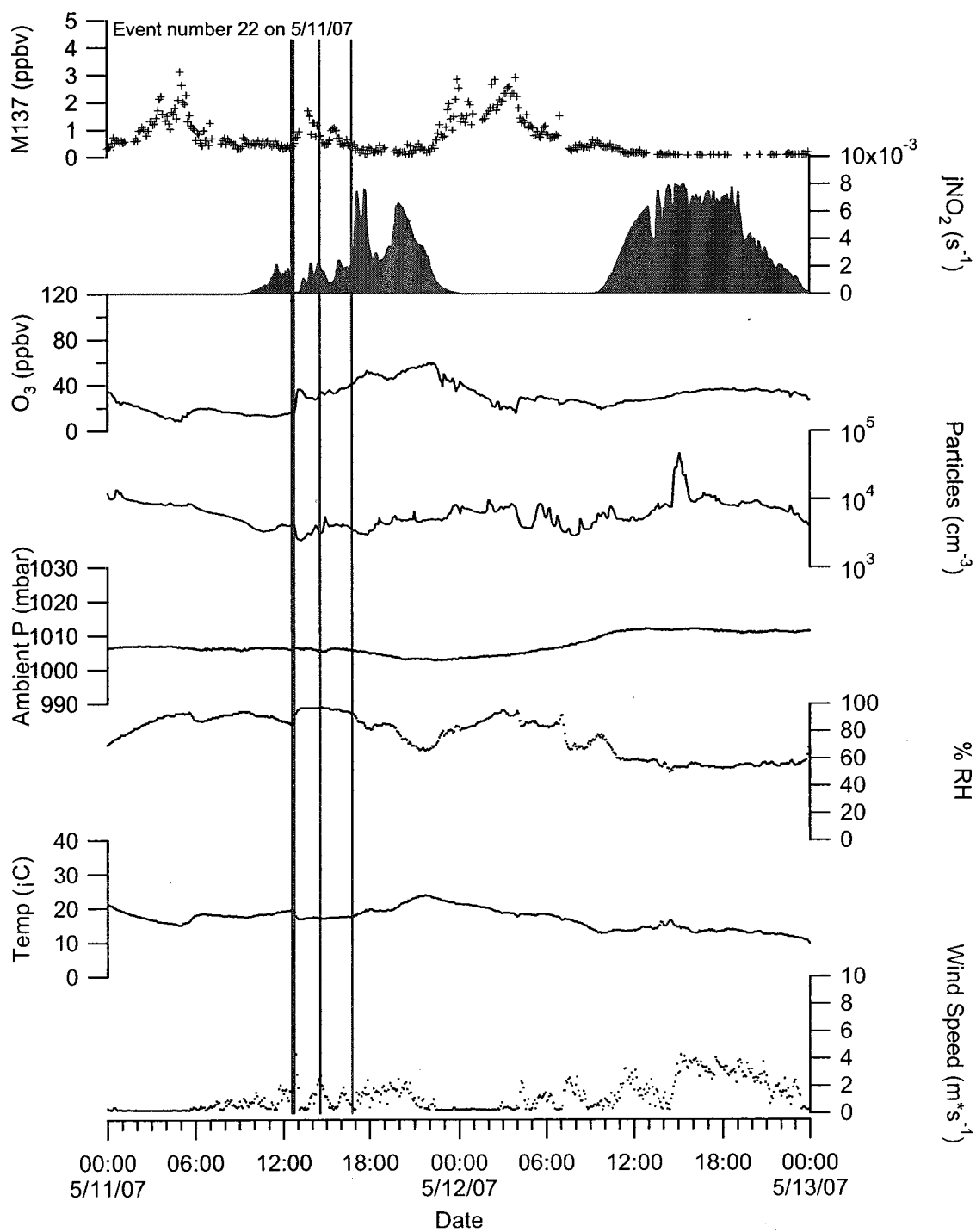


Figure 5-3. An example Type B event, where the mixing ratios of monoterpenes peak for a brief period of time, from May 11, 2007.

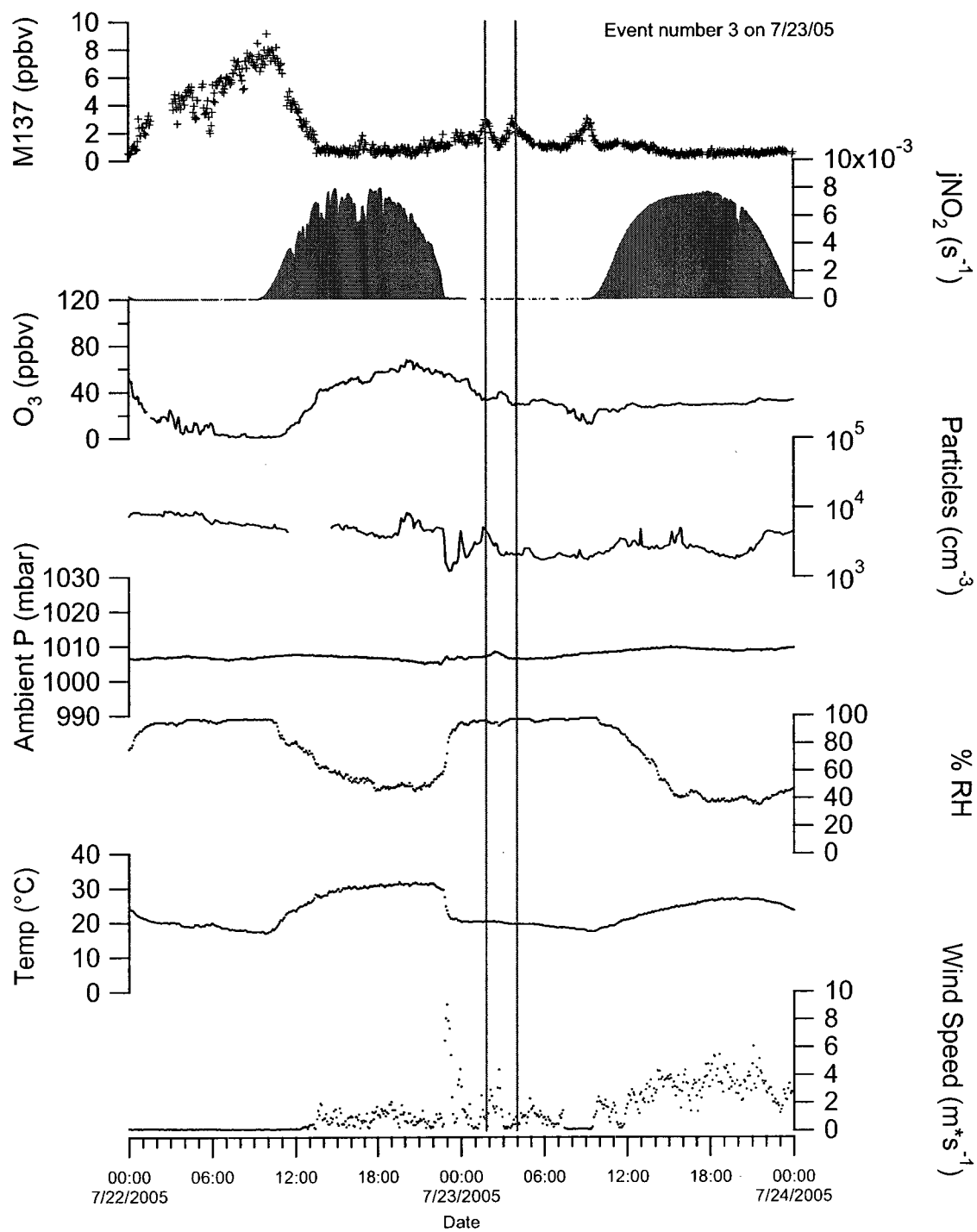


Figure 5-4. An example of a Type C event, where the storm passage coincides with a drop in monoterpene mixing ratios from July 23, 2005.

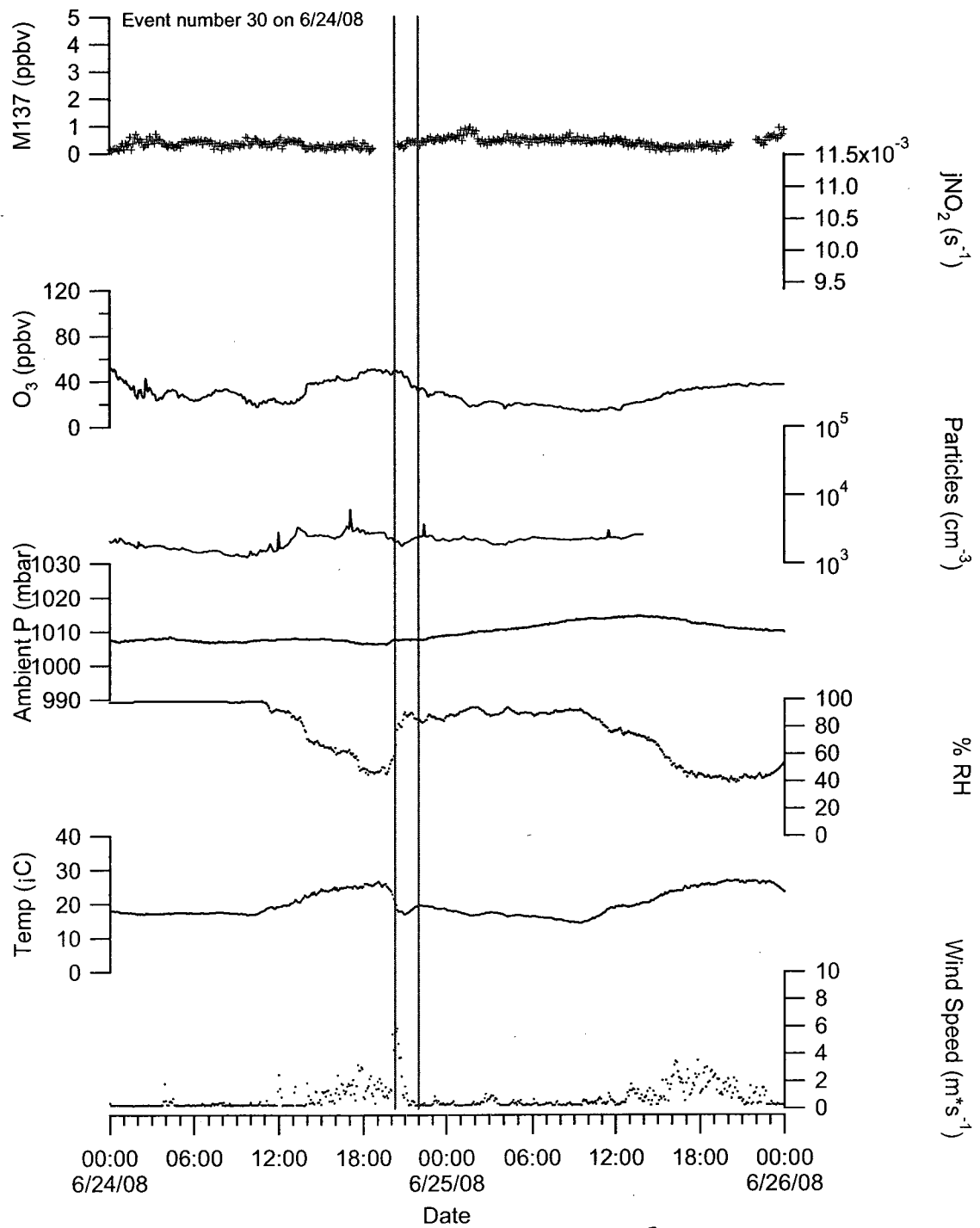


Figure 5-5. An example of a Type D event, where the storm passage had little impact on mixing ratios, from June 24, 2008.

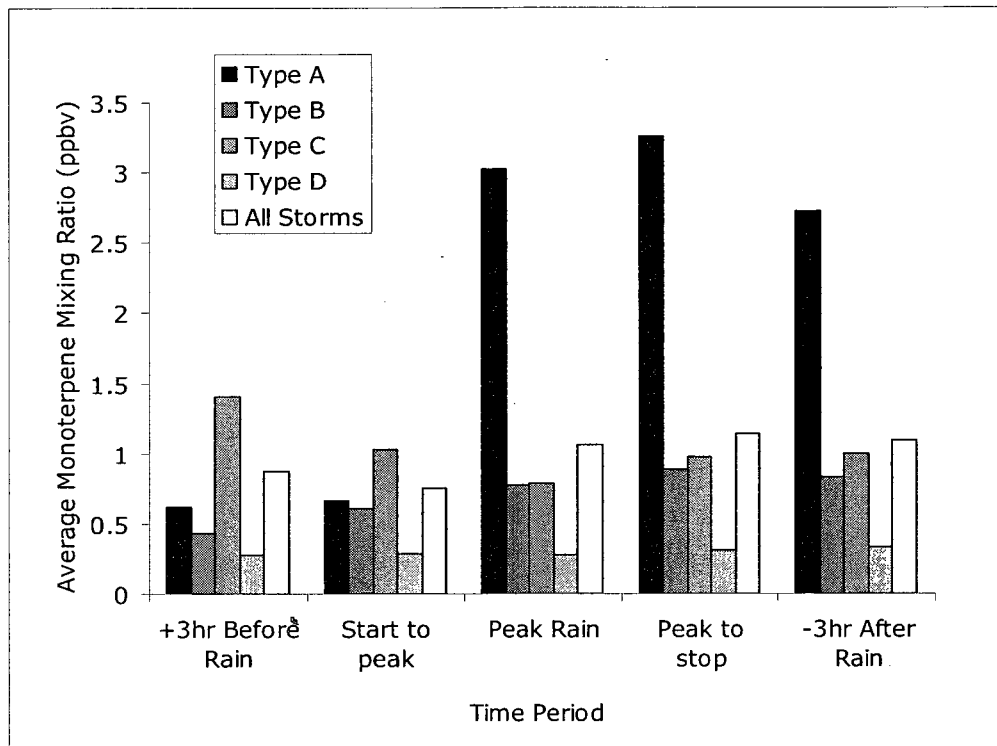


Figure 5-6. The average mixing ratio of monoterpenes as storm systems pass over Thompson Farm.

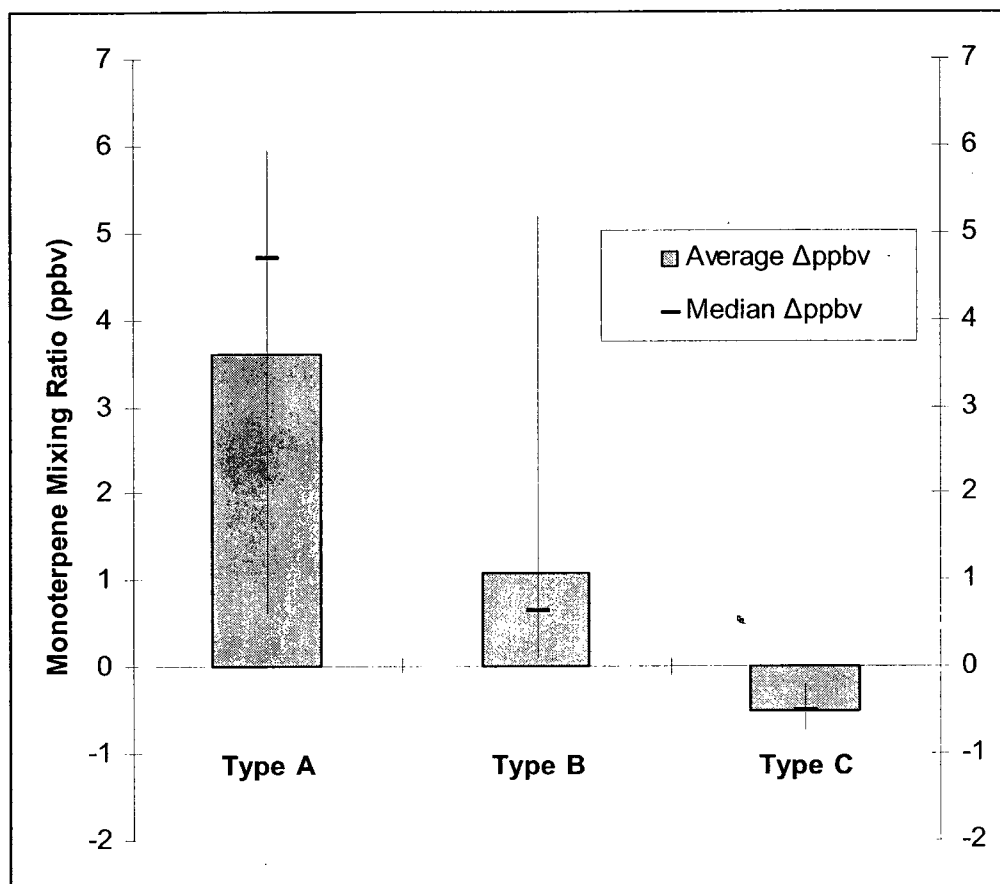


Figure 5-7. The average (grey bars), median (horizontal bars), minimum, and maximum (whiskers) change in monoterpene mixing ratios for each type of storm event.

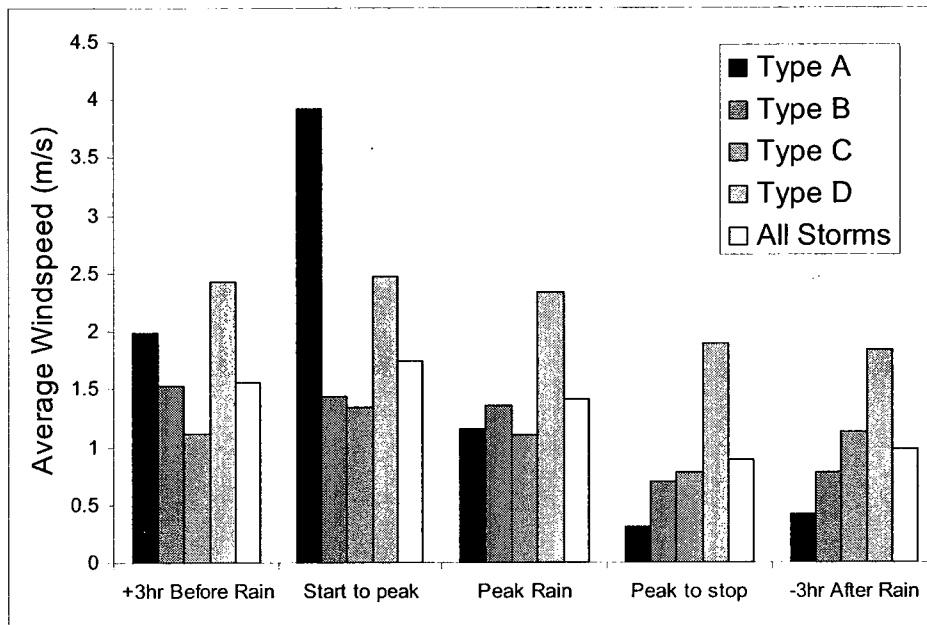


Figure 5-8. Average wind speed for each type of storm event.

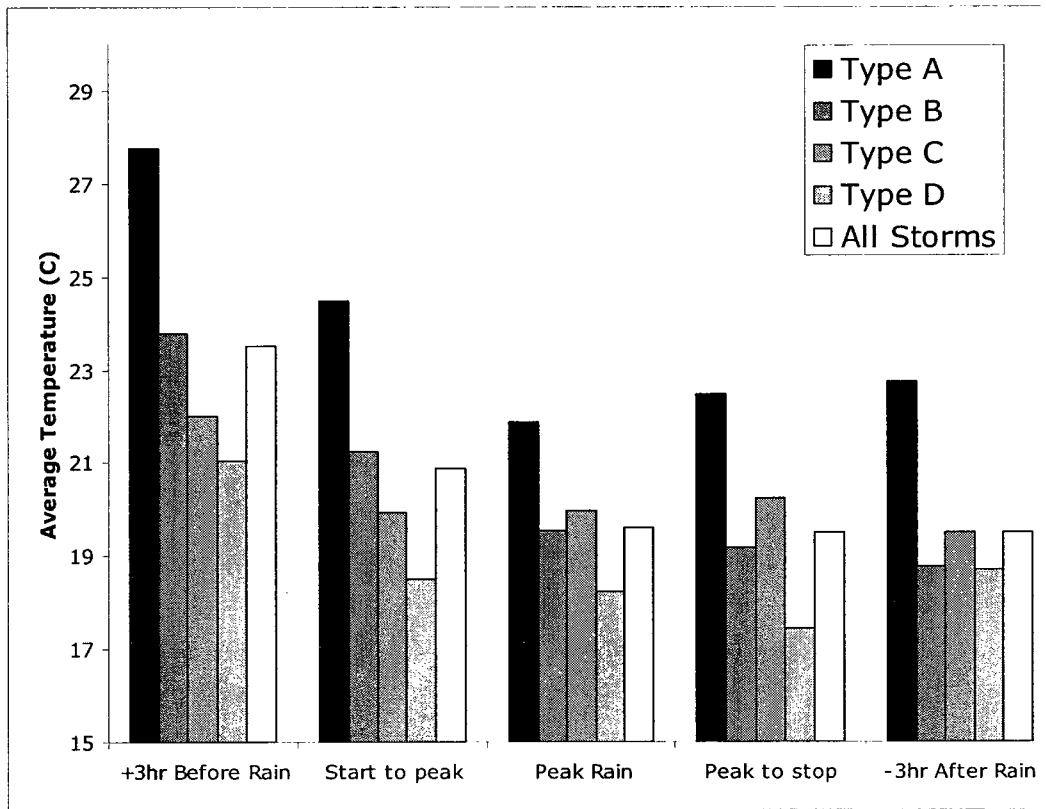


Figure 5-9. Average temperature (° C) for each storm type.

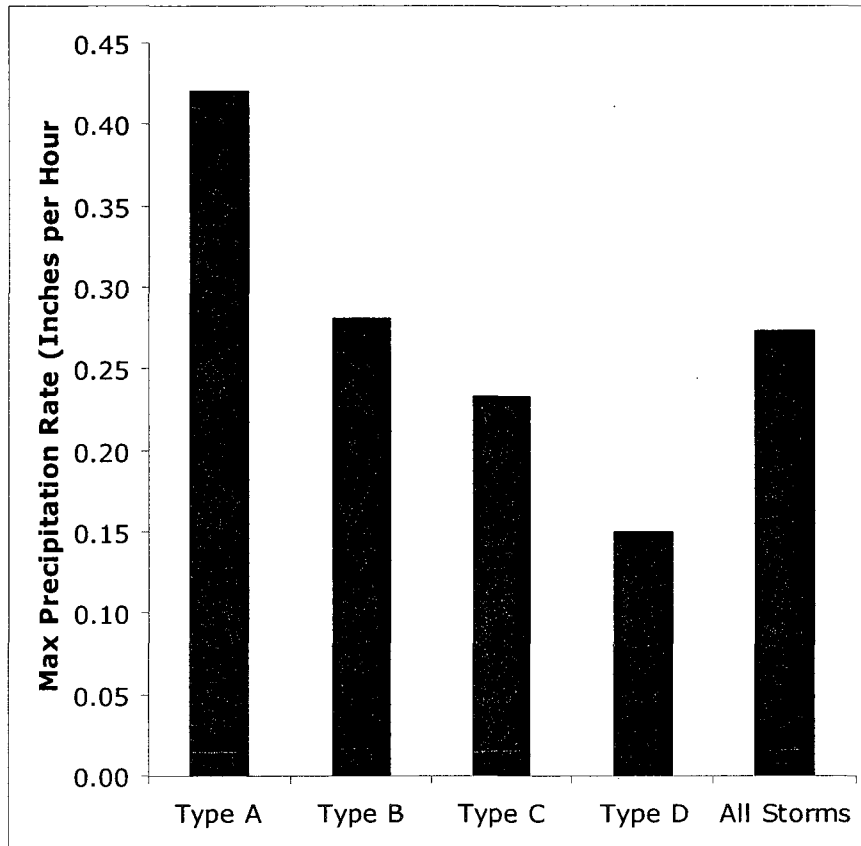


Figure 5-10. Average peak precipitation rate over Thompson Farm for each event type.

REFERENCES

1. Lindinger, W.; Hansel, A.; Jordan, A., On-line monitoring of volatile organic compounds at pptv levels by means of proton-transfer-reaction mass spectrometry (PTR-MS) medical applications, food control and environmental research. *Int. J. Mass Spectrom. Ion Processes* **1998**, 173, (3), 191.
2. de Gouw, J.; Warneke, C.; Karl, T.; Eerdekens, G.; van der Veen, C.; Fall, R., Sensitivity and specificity of atmospheric trace gas detection by proton-transfer-reaction mass spectrometry. *Int. J. Mass spectrom.* **2003**, 223-224, 365.
3. de Gouw, J.; Warneke, C., Measurements of Volatile Organic Compounds in the Earth's Atmosphere Using Proton-Transfer-Reaction Mass Spectrometry. *Mass Spectrom. Rev.* **2006**, (26), 223.
4. Blake, R. S.; Monks, P. S.; Ellis, A. M., Proton Transfer Reaction Mass Spectrometry. *Chem. Rev.* **2009**, 109, 861.
5. Hansel, A.; Jordan, A.; Holzinger, R.; Prazeller, P.; Vogel, W.; Lindinger, W., Proton transfer reaction mass spectrometry: online trace of gas analysis at the ppb level. *Int. J. Mass Spectrom. Ion Processes* **1995**, 149-150, 609.
6. Ferguson, E. E.; Fehsenfeld, F. C.; Albritton, D. L., Ion Chemistry of the earth's atmosphere. In *Gas Phase Ion Chemistry*, Bowers, M. T., Ed. Academic Press: New York, 1979; Vol. 1, pp 45.
7. Mark, T. D.; Lindinger, W.; Howorka, F.; Egger, F.; Varney, R. N.; Pahl, M., A Simple Bakeable Hollow Cathode Device for the Direct Study of Plasma Constituents. *Rev. Sci. Instrum.* **1972**, 43, (11), 1852.
8. Lindinger, W., Reaction Rate Constants in Steady-State Hollow-Cathode Discharges: Ar + H₂O Reactions. *Phys. Rev. A: At. Mol. Opt. Phys.* **1973**, 7, (1), 328.
9. Howorka, F.; Lindinger, W.; Varney, R. N., Reaction rate constants in steady-state hollow cathode discharges: N₂ + H₂O reactions. *J. Chem. Phys.* **1974**, 61, (3), 1180.

10. Kore Technology. <http://www.kore.co.uk/> (7/22/2010),
11. Hanson, D. R.; Greenberg, J.; Henry, B. E.; Kosciuch, E., Proton transfer reaction mass spectrometry at high drift tube pressure. *Int. J. Mass spectrom.* **2003**, 223-224, 507.
12. Prazeller, P.; Palmer, P. T.; Boscaini, E.; Jobson, T.; Alexander, M., Proton transfer reaction ion trap mass spectrometer. *Rapid Commun. Mass Spectrom.* **2003**, 17, (14), 1593.
13. Steeghs, M.; Bais, H. P.; de Gouw, J.; Goldan, P.; Kuster, W.; Northway, M.; Fall, R.; Vivanco, J. M., Proton-Transfer-Reaction Mass Spectrometry as a New Tool for Real Time Analysis of Root-Secreted Volatile Organic Compounds in Arabidopsis. *Plant Physiol.* **2004**, 135, (1), 47.
14. Ennis, C. J.; Reynolds, J. C.; Keely, B. J.; Carpenter, L. J., A hollow cathode proton transfer reaction time of flight mass spectrometer. *Int. J. Mass spectrom.* **2005**, 247, (1-3), 72.
15. Sellegri, K.; Umann, B.; Hanke, M.; Arnold, F., Deployment of a ground-based CIMS apparatus for the detection of organic gases in the boreal forest during the QUEST campaign. *Atmos. Chem. Phys.* **2005**, 5, 357.
16. Blake, R. S.; Whyte, C.; Hughes, C. O.; Ellis, A. M.; Monks, P. S., Demonstration of Proton-Transfer Reaction Time-of-Flight Mass Spectrometry for Real-Time Analysis of Trace Volatile Organic Compounds. *Anal. Chem.* **2004**, 76, (13), 3841.
17. Blake, R. S.; Wyche, K. P.; Ellis, A. M.; Monks, P. S., Chemical ionization reaction time-of-flight mass spectrometry: Multi-reagent analysis for determination of trace gas composition. *Int. J. Mass spectrom.* **2006**, 254, (1-2), 85.
18. Tanimoto, H.; Aoki, N.; Inomata, S.; Hirokawa, J.; Sadanaga, Y., Development of a PTR-TOFMS instrument for real-time measurements of volatile organic compounds in air. *Int. J. Mass spectrom.* **2007**, 263, (1), 1.
19. Hanson, D. R.; Koppes, M.; Stoffers, A.; Harsdorf, R.; Edelen, K., Proton transfer mass spectrometry at 11 hPa with a circular glow discharge: Sensitivities and applications. *Int. J. Mass spectrom.* **2009**, 282, (1-2), 28.
20. Williams, J.; Pöschl, U.; Crutzen, P. J.; Hansel, A.; Holzinger, R.; Warneke, C.; Lindinger, W.; Lelieveld, J., An Atmospheric Chemistry Interpretation of Mass Scans Obtained from a Proton Transfer Mass Spectrometer Flown over the Tropical Rainforest of Surinam. *J. Atmos. Chem.* **2001**, 38, (2), 133.

21. Lee, A.; Goldstein, A. H.; Keywood, M. D.; Gao, S.; Varutbangkul, V.; Bahreini, R.; Ng, N. L.; Flagan, R. C.; Seinfeld, J. H., Gas-phase products and secondary aerosol yields from the ozonolysis of ten different terpenes. *J. Geophys. Res.* **2006**, 111, (D7), D07302.
22. Lee, A.; Goldstein, A. H.; Kroll, J. H.; Ng, N. L.; Varutbangkul, V.; Flagan, R. C.; Seinfeld, J. H., Gas-phase products and secondary aerosol yields from the photooxidation of 16 different terpenes. *J. Geophys. Res.* **2006**, 111, (D17), D17305.
23. Karl, T.; Potosnak, M.; Guenther, A.; Clark, D.; Walker, J.; Herrick, J. D.; Geron, C., Exchange processes of volatile organic compounds above a tropical rain forest: Implications for modeling tropospheric chemistry above dense vegetation. *J. Geophys. Res.* **2004**, 109, (D18), D18306.
24. de Gouw, J. A.; Goldan, P. D.; Warneke, C.; Kuster, W. C.; Roberts, J. M.; Marchewka, M.; Bertman, S. B.; Pszenny, A. A. P.; Keene, W. C., Validation of proton transfer reaction-mass spectrometry (PTR-MS) measurements of gas-phase organic compounds in the atmosphere during the New England Air Quality Study (NEAQS) in 2002. *J. Geophys. Res.* **2003**, 108, (D21), 4682.
25. Rogers, T. M.; Grimsrud, E. P.; Herndon, S. C.; Jayne, J. T.; Kolb, C. E.; Allwine, E.; Westberg, H.; Lamb, B. K.; Zavala, M.; Molina, L. T.; Molina, M. J.; Knighton, W. B., On-road measurements of volatile organic compounds in the Mexico City metropolitan area using proton transfer reaction mass spectrometry. *Int. J. Mass spectrom.* **2006**, 252, (1), 26.
26. Jordan, C.; Fitz, E.; Hagan, T.; Sive, B.; Frinak, E.; Haase, K.; Cottrell, L.; Buckley, S.; Talbot, R., Long-term study of VOCs measured with PTR-MS at a rural site in New Hampshire with urban influences. *Atmos. Chem. Phys.* **2009**, 9, (14), 4677.
27. Schwarz, K.; Filipiak, W.; Amann, A., Determining concentration patterns of volatile compounds in exhaled breath by PTR-MS. *J. Breath Res.* **2009**, 3, (2), 027002.
28. Maleknia, S. D.; Bell, T. L.; Adams, M. A., PTR-MS analysis of reference and plant-emitted volatile organic compounds. *Int. J. Mass spectrom.* **2007**, 262, (3), 203.
29. Tani, A.; Hayward, S.; Hansel, A.; Hewitt, C. N., Effect of water vapour pressure on monoterpene measurements using proton transfer reaction-mass spectrometry (PTR-MS). *Int. J. Mass spectrom.* **2004**, 239, (2-3), 161.
30. Tani, A.; Hayward, S.; Hewitt, C. N., Measurement of monoterpenes and related compounds by proton transfer reaction-mass spectrometry (PTR-MS). *Int. J. Mass spectrom.* **2003**, 223-224, 561.

31. Lau, Y. K.; Ikuta, S.; Kebarle, P., Thermodynamics and Kinetics of Gas-Phase Reactions: $\text{H}_3\text{O}^+(\text{H}_2\text{O})_{n-1} + \text{H}_2\text{O} = \text{H}_3\text{O}^+(\text{H}_2\text{O})_n$. *J. Am. Chem. Soc.* **1982**, 104, 1462.
32. Warneke, C.; van der Veen, C.; Luxembourg, S.; de Gouw, J. A.; Kok, A., Measurements of benzene and toluene in ambient air using proton-transfer-reaction mass spectrometry: calibration, humidity dependence, and field intercomparison. *Int. J. Mass spectrom.* **2001**, 207, 167.
33. Meng, Z.; Seinfeld, J. H.; Saxena, P., Gas/Aerosol Distribution of Formic and Acetic Acids. *Aerosol Sci. Technol.* **1995**, 23, (4), 561.
34. Chebbi, A.; Carlier, P., Carboxylic acids in the troposphere, occurrence, sources, and sinks: A review. *Atmos. Environ.* **1996**, 30, (24), 4233.
35. Keene, W. C.; Talbot, R. W.; Andreae, M. O.; Beecher, K.; Berresheim, H.; Castro, M.; Farmer, J. C.; Galloway, J. N.; Hoffmann, M. R.; Li, S.-M.; Maben, J. R.; Munger, J. W.; Norton, R. B.; Pszenny, A. A. P.; Puxbaum, H.; Westberg, H.; Winiwarter, W., An Intercomparison of Measurement Systems for Vapor and Particulate Phase Concentrations of Formic and Acetic Acids. *J. Geophys. Res.* **1989**, 94, (D5), 6457.
36. Guenther, A., Corrigendum to "Estimates of global terrestrial isoprene emissions using MEGAN (Model of Emissions of Gases and Aerosols from Nature)" published in *Atmos. Chem. Phys.*, 6, 3181-3210, 2006. *Atmos. Chem. Phys.* **2007**, 7, (16), 4327.
37. Guenther, A.; Karl, T.; Harley, P.; Wiedinmyer, C.; Palmer, P. I.; Geron, C., Estimates of global terrestrial isoprene emissions using MEGAN (Model of Emissions of Gases and Aerosols from Nature). *Atmos. Chem. Phys.* **2006**, 6, (11), 3181.
38. Guenther, A.; Hewitt, C. N.; Erickson, D.; Fall, R.; Geron, C.; Graedel, T.; Harley, P.; Klinger, L.; Lerdau, M.; McKay, W. A.; Pierce, T.; Scholes, B.; Steinbrecher, R.; Tallamraju, R.; Taylor, J.; Zimmerman, P., A global model of natural volatile organic compound emissions. *J. Geophys. Res.* **1995**, 100, (D5), 8873.
39. Guenther, A. B.; Zimmerman, P. R.; Harley, P. C.; Monson, R. K.; Fall, R., Isoprene and Monoterpene Emission Rate Variability: Model Evaluations and Sensitivity Analyses. *J. Geophys. Res.* **1993**, 98, (D7), 12609.
40. Heald, C. L.; Jacob, D. J.; Park, R. J.; Russell, L. M.; Huebert, B. J.; Seinfeld, J. H.; Liao, H.; Weber, R. J., A large organic aerosol source in the free troposphere missing from current models. *Geophys. Res. Lett.* **2005**, 32, (18), L18809.

41. Goto, D.; Takemura, T.; Nakajima, T., Importance of global aerosol modeling including secondary organic aerosol formed from monoterpene. *J. Geophys. Res.* **2008**, 113, (D7), D07205.
42. Trapp, R. J.; Diffenbaugh, N. S.; Gluhovsky, A., Transient response of severe thunderstorm forcing to elevated greenhouse gas concentrations. *Geophys. Res. Lett.* **2009**, 36, (1), L01703.
43. Trapp, R. J.; Diffenbaugh, N. S.; Brooks, H. E.; Baldwin, M. E.; Robinson, E. D.; Pal, J. S., Changes in severe thunderstorm environment frequency during the 21st century caused by anthropogenically enhanced global radiative forcing. *PNAS* **2007**, 104, (50), 19719.
44. Knighton, W. B.; Fortner, E. C.; Herndon, S. C.; Wood, E. C.; Miake-Lye, R. C., Adaptation of a proton transfer reaction mass spectrometer instrument to employ NO^+ as reagent ion for the detection of 1,3-butadiene in the ambient atmosphere. *Rapid Commun. Mass Spectrom.* **2009**, 23, (20), 3301.
45. Hansel, A.; Singer, W.; Wisthaler, A.; Schwarzmann, M.; Lindinger, W., Energy dependencies of the proton transfer reactions $\text{H}_3\text{O}^+ + \text{CH}_2\text{O} \rightarrow \text{CH}_2\text{OH} + \text{H}_2\text{O}^*$. *Int. J. Mass Spectrom. Ion Processes* **1997**, 167/168, 697.
46. Wisthaler, A.; Apel, E. C.; Bossmeyer, J.; Hansel, A.; Junkermann, W.; Koppmann, R.; Meier, R.; Muller, K.; Solomon, S. J.; Steinbrecher, R.; Tillmann, R.; Brauers, T., Technical Note: Intercomparison of formaldehyde measurements at the atmosphere simulation chamber SAPHIR. *Atmos. Chem. Phys.* **2008**, 8, (8), 2189.
47. Inomata, S.; Tanimoto, H.; Kameyama, S.; Tsunogai, U.; Irie, H.; Kanaya, Y.; Wang, Z., Technical Note: Determination of formaldehyde mixing ratios in air with PTR-MS: laboratory experiments and field measurements. *Atmos. Chem. Phys.* **2008**, 8, (2), 273.
48. Schoon, N.; Amelynck, C.; Vereecken, L.; Arijs, E., A selected ion flow tube study of the reactions of H_3O^+ , NO^+ and O_2^+ with a series of monoterpenes. *Int. J. Mass spectrom.* **2003**, 229, (3), 231.
49. Kawai, Y.; Yamaguchi, S.; Okada, Y.; Takeuchi, K.; Yamauchi, Y.; Ozawa, S.; Nakai, H., Reactions of protonated water clusters $\text{H}^+(\text{H}_2\text{O})_n$ ($n=1-6$) with dimethylsulfoxide in a guided ion beam apparatus. *Chem. Phys. Lett.* **2003**, 377, (1-2), 69.

50. Roth, A., *Vacuum Technology*. 3rd ed.; Elsevier Science Publishers B.V.: Amsterdam, 1990.
51. TurboDrag Pump TMH 071 P. In Pfeiffer Vacuum: 2009; p 30.
52. *Atmospheric Chemistry and Global Change*. Oxford University Press: New York, 1999.
53. de Gouw, J. A.; Howard, C. J.; Custer, T. G.; Baker, B. M.; Fall, R., Proton-Transfer Chemical-Ionization Mass Spectrometry Allows Real-Time Analysis of Volatile Organic Compounds Released from Cutting and Drying of Crops. *Environ. Sci. Technol.* **2000**, 34, (12), 2640.
54. Sinha, V.; Custer, T. G.; Kluepfel, T.; Williams, J., The effect of relative humidity on the detection of pyrrole by PTR-MS for OH reactivity measurements. *Int. J. Mass spectrom.* **2008**.
55. Knighton, W. B.; Förtner, E. C.; Midey, A. J.; Viggiano, A. A.; Herndon, S. C.; Wood, E. C.; Kolb, C. E., HCN detection with a proton transfer reaction mass spectrometer. *Int. J. Mass spectrom.* **2009**, 283, (1-3), 112.
56. Brown, P.; Watts, P.; Märk, T. D.; Mayhew, C. A., Proton Transfer Reaction Mass Spectrometry investigations on the effects of reduced electric field and reagent ion internal energy on product ion branching ratios for a series of saturated alcohols. *Int. J. Mass spectrom.* **2010**, In Press, Accepted Manuscript.
57. McFarland, M.; Albritton, D. L.; Fehsenfeld, F. C.; Ferguson, E. E.; Schmeltekopf, A. L., Flow-drift technique for ion mobility and ion-molecule reaction rate constant measurements. II. Positive ion reactions of N^+ , O^+ , and H_2^+ with O_2 and O^+ with N_2 from thermal to (inverted lazy s)2 eV. *J. Chem. Phys.* **1973**, 59, (12), 6620.
58. Lindinger, W.; Hansel, A.; Jordan, A., Proton-transfer-reaction mass spectrometry (PTR-MS): on-line monitoring of volatile organic compounds at pptv levels. *Chem Soc Rev* **1998**, 27, (5), 346.
59. Solouki, T.; Szulejko, J. E., Bimolecular and Unimolecular Contributions to the Disparate Self-Chemical Ionizations of α -Pinene and Camphene Isomers. *J. Am. Soc. Mass. Spectrom.* **2007**, 18, (11), 2026.
60. Fernandez, M. T.; Williams, C.; Mason, R. S.; Costa Cabral, B. J., Experimental and theoretical proton affinity of limonene. *J. Chem. Soc., Faraday Trans.* **1998**, 94, (10), 1427.

61. Hunter, E. P. L.; Lias, S. G., Evaluated Gas Phase Basicities and Proton Affinities of Molecules: An Update. *J. Phys. Chem. Ref. Data* **1998**, 27, (3), 413.
62. Norman, M.; Hansel, A.; Wisthaler, A., O_2^+ as reagent ion in the PTR-MS instrument: Detection of gas-phase ammonia. *Int. J. Mass spectrom.* **2007**, 265, (2-3), 382.
63. Spanel, P.; Diskin, A. M.; Wang, T.; Smith, D., A SIFT study of the reactions of H_3O^+ , NO^+ and O_2^+ with hydrogen peroxide and peroxyacetic acid. *Int. J. Mass spectrom.* **2003**, 228, (2-3), 269.
64. Spanel, P.; Smith, D., Progress in SIFT-MS: Breath analysis and other applications. *Mass Spectrom. Rev.* **2010**, N/A.
65. de Gouw, J. A.; Krishnamurthy, M.; Bierbaum, V. M.; Leone, S. R., Measured and calculated mobilities of cluster ions drifting in helium and in nitrogen. *Int. J. Mass Spectrom. Ion Processes* **1997**, 167-168, 281.
66. Gazda, E., The mobility of $H^+(H_2O)_n$ ions in water vapour. *J. Phys. B: At. Mol. Phys.* **1986**, 19, (18), 2973.
67. Kebarle, P.; Searles, S. K.; Zolla, A.; Scarborough, J.; Arshadi, M., Solvation of the hydrogen ion by water molecules in the gas phase. Heats and entropies of solvation of individual reactions. $H^+(H_2O)_{n-1} + H_2O \rightarrow H^+(H_2O)_n$. *J. Am. Chem. Soc.* **1967**, 89, (25), 6393.
68. Cunningham, A. J.; Payzant, J. D.; Kebarle, P., Kinetic study of the proton hydrate $H^+(H_2O)_n$ equilibria in the gas phase. *J. Am. Chem. Soc.* **1972**, 94, (22), 7627.
69. Spanel, P.; Smith, D., Influence of water vapour on selected ion flow tube mass spectrometric analyses of trace gases in humid air and breath. *Rapid Commun. Mass Spectrom.* **2000**, 14, (20), 1898.
70. Dawson, P. H., The collision-induced dissociation of protonated water clusters studied using a triple quadrupole. *Int. J. Mass Spectrom. Ion Phys.* **1982**, 43, (2-3), 195.
71. Dalleska, N. F.; Honma, K.; Armentrout, P. B., Stepwise solvation enthalpies of protonated water clusters: collision-induced dissociation as an alternative to equilibrium studies. *J. Am. Chem. Soc.* **1993**, 115, (25), 12125.

72. Thomas, M. M.; Friedman, J. F.; Menéndez-Barreto, M.; Viggiano, A. A.; Morris, R. A.; Miller, A. E. S.; Paulson, J. F., Ion-molecule reactions at very high temperatures. *Phys. Scr.* **1994**, 1994, (T53), 84.
73. Spanel, P.; Smith, D., Selected ion flow tube studies of the reactions of H_3O^+ , NO^+ , and O_2^+ with several aromatic and aliphatic hydrocarbons. *Int. J. Mass spectrom.* **1998**, 181, (1-3), 1.
74. Spanel, P.; Smith, D., Reactions of Hydrated Hydronium Ions and Hydrated Hydroxide Ions with Some Hydrocarbons and Oxygen-Bearing Organic Molecules. *J. Phys. Chem.* **1995**, 99, (42), 15551.
75. Warneke, C.; de Gouw, J. A.; Kuster, W. C.; Goldan, P. D.; Fall, R., Validation of Atmospheric VOC Measurements by Proton-Transfer- Reaction Mass Spectrometry Using a Gas-Chromatographic Preseparation Method. *Environ. Sci. Technol.* **2003**, 37, (11), 2494.
76. Ambrose, J. L.; Haase, K.; Russo, R. S.; Zhou, Y.; White, M. L.; Frinak, E. K.; Jordan, C.; Mayne, H. R.; Talbot, R.; Sive, B. C., An intercomparison of GC-FID and PTR-MS toluene measurements in ambient air under conditions of enhanced monoterpene loading. *Atmos. Meas. Tech. Discuss.* **2010**, 3, (1), 1.
77. Fehsenfeld, F. C.; Ancellet, G.; Bates, T. S.; Goldstein, A. H.; Hardesty, R. M.; Honrath, R.; Law, K. S.; Lewis, A. C.; Leaitch, R.; McKeen, S.; Meagher, J.; Parrish, D. D.; Pszenny, A. A. P.; Russell, P. B.; Schlager, H.; Seinfeld, J.; Talbot, R.; Zbinden, R., International Consortium for Atmospheric Research on Transport and Transformation (ICARTT): North America to Europe; Overview of the 2004 summer field study. *J. Geophys. Res.* **2006**, 111, (D23), D23S01.
78. Kesselmeier, J., Exchange of Short-Chain Oxygenated Volatile Organic Compounds (VOCs) between Plants and the Atmosphere: A Compilation of Field and Laboratory Studies. *J. Atmos. Chem.* **2001**, 39, (3), 219.
79. Talbot, R. W.; Dibb, J. E.; Scheuer, E. M.; Blake, D. R.; Blake, N. J.; Gregory, G. L.; Sachse, G. W.; Bradshaw, J. D.; Sandholm, S. T.; Singh, H. B., Influence of biomass combustion emissions on the distribution of acidic trace gases over the southern Pacific basin during austral springtime. *J. Geophys. Res.* **1999**, 104, (D5), 5623.
80. Orzechowska, G. E.; Paulson, S. E., Photochemical Sources of Organic Acids. 1. Reaction of Ozone with Isoprene, Propene, and 2-Butenes under Dry and Humid Conditions Using SPME. *J. Phys. Chem. A* **2005**, 109, (24), 5358.

81. Yu, Y.; Ezell, M. J.; Zelenyuk, A.; Imre, D.; Alexander, L.; Ortega, J.; D'Anna, B.; Harmon, C. W.; Johnson, S. N.; Finlayson-Pitts, B. J., Photooxidation of α -pinene at high relative humidity in the presence of increasing concentrations of NO_x . *Atmos. Environ.* **2008**, *42*, (20), 5044.
82. Rosado-Reyes, C. M.; Francisco, J. S., Atmospheric Oxidation Pathways of Acetic Acid. *J. Phys. Chem. A* **2006**, *110*, (13), 4419.
83. Mackay, G. I.; Hopkinson, A. C.; Bohme, D. K., Acid catalysis in the gas phase: dissociative proton transfer to formic and acetic acid. *J. Am. Chem. Soc.* **1978**, *100*, (24), 7460.
84. Wyche, K. P.; Monks, P. S.; Ellis, A. M.; Cordell, R. L.; Parker, A. E.; Whyte, C.; Metzger, A.; Dommen, J.; Duplissy, J.; Prevot, A. S. H.; Baltensperger, U.; Rickard, A. R.; Wulfert, F., Gas phase precursors to anthropogenic secondary organic aerosol: detailed observations of 1,3,5-trimethylbenzene photooxidation. *Atmos. Chem. Phys.* **2009**, *9*, (2), 635.
85. Warneke, C.; Kuczynski, J.; Hansel, A.; Jordan, A.; Vogel, W.; Lindinger, W., Proton transfer reaction mass spectrometry (PTR-MS): propanol in human breath. *Int. J. Mass Spectrom. Ion Processes* **1996**, *154*, (1-2), 61.
86. M. Steinbacher, J. D., C. Ammann, C. Spirig, A. Neftel, A. S. H. Prevot, Performance characteristics of a proton-transfer-reaction mass spectrometer (PTR-MS) derived from laboratory and field measurements. *Int. J. Mass spectrom.* **2004**, *219*, 117.
87. Karl, T.; Harley, P.; Guenther, A.; Rasmussen, R.; Baker, B.; Jardine, K.; Nemitz, E., The bi-directional exchange of oxygenated VOCs between a loblolly pine (*Pinus taeda*) plantation and the atmosphere. *Atmos. Chem. Phys.* **2005**, *5*, (11), 3015.
88. Fortner, E. C.; Zheng, J.; Zhang, R.; Berk Knighton, W.; Volkamer, R. M.; Sheehy, P.; Molina, L.; André, M., Measurements of Volatile Organic Compounds Using Proton Transfer Reaction – Mass Spectrometry during the MILAGRO 2006 Campaign. *Atmos. Chem. Phys.* **2009**, *9*, (2), 467.
89. Kim, S.; Karl, T.; Guenther, A.; Tyndall, G.; Orlando, J.; Harley, P.; Rasmussen, R.; Apel, E., Emissions and ambient distributions of Biogenic Volatile Organic Compounds (BVOC) in a ponderosa pine ecosystem: interpretation of PTR-MS mass spectra. *Atmos. Chem. Phys.* **2010**, *10*, (4), 1759.
90. Holzinger, R.; Millet, D. B.; Williams, B.; Lee, A.; Kreisberg, N.; Hering, S. V.; Jimenez, J.; Allan, J. D.; Worsnop, D. R.; Goldstein, A. H., Emission, oxidation, and

secondary organic aerosol formation of volatile organic compounds as observed at Chebogue Point, Nova Scotia. *J. Geophys. Res.* **2007**, 112, (D10), D10S24.

91. Holzinger, R.; Sandoval-Soto, L.; Rottenberger, S.; Crutzen, P. J.; Kesselmeier, J., Emissions of volatile organic compounds from *Quercus ilex* L. measured by Proton Transfer Reaction Mass Spectrometry under different environmental conditions. *J. Geophys. Res.* **2000**, 105, (D16), 20573.

92. Warneke, C.; de Gouw, J. A.; Goldan, P. D.; Kuster, W. C.; Williams, E. J.; Lerner, B. M.; Jakoubek, R.; Brown, S. S.; Stark, H.; Aldener, M.; Ravishankara, A. R.; Roberts, J. M.; Marchewka, M.; Bertman, S.; Sueper, D. T.; McKeen, S. A.; Meagher, J. F.; Fehsenfeld, F. C., Comparison of daytime and nighttime oxidation of biogenic and anthropogenic VOCs along the New England coast in summer during New England Air Quality Study 2002. *J. Geophys. Res.* **2004**, 109, (D10), D10309.

93. B.T. Jobson, M. L. A., G.D. Paupin, G.G. Muntean, Online-analysis of organic compounds in diesel exhaust using a proton transfer reaction mass spectrometer (PTR-MS). *Int. J. Mass spectrom.* **2005**, 245.

94. de Gouw, J. A.; Warneke, C.; Stohl, A.; Wollny, A. G.; Brock, C. A.; Cooper, O. R.; Holloway, J. S.; Trainer, M.; Fehsenfeld, F. C.; Atlas, E. L.; Donnelly, S. G.; Stroud, V.; Lueb, A., Volatile organic compounds composition of merged and aged forest fire plumes from Alaska and western Canada. *J. Geophys. Res.* **2006**, 111, (D10), D10303.

95. Christian, T. J.; Kleiss, B.; Yokelson, R. J.; Holzinger, R.; Crutzen, P. J.; Hao, W. M.; Shirai, T.; Blake, D. R., Comprehensive laboratory measurements of biomass-burning emissions: 2. First intercomparison of open-path FTIR, PTR-MS, and GC-MS/FID/ECD. *J. Geophys. Res.* **2004**, 109, (D2), D02311.

96. Afeefy, H. Y.; Liebman, J. F.; Stein, S. E., Neutral Thermochemical Data. In *NIST Chemistry WebBook, NIST Standard Reference Database*, 69 ed.; Linstrom, P. J.; Mallard, W. G., Eds. National Institute of Standards and Technology: Gaithersburg MD, 2010.

97. Spänel, P.; Smith, D., SIFT studies of the reactions of H_3O^+ , NO^+ and O_2^+ with a series of volatile carboxylic acids and esters. *Int. J. Mass Spectrom. Ion Processes* **1998**, 172, (1-2), 137.

98. Hartungen, E. v.; Wisthaler, A.; Mikoviny, T.; Jaksch, D.; Boscaini, E.; Dunphy, P. J.; Märk, T. D., Proton-transfer-reaction mass spectrometry (PTR-MS) of carboxylic acids: Determination of Henry's law constants and axillary odour investigations. *Int. J. Mass spectrom.* **2004**, 239, (2-3), 243.

99. Ambrose, J. L.; Mao, H.; Mayne, H. R.; Stutz, J.; Talbot, R.; Sive, B. C., Nighttime nitrate radical chemistry at Appledore Island, Maine during the 2004 International Consortium for Atmospheric Research on Transport and Transformation. *J. Geophys. Res.* **2007**, *112*, (D21), D21302.
100. Hayward, S.; Hewitt, C. N.; Sartin, J. H.; Owen, S. M., Performance Characteristics and Applications of a Proton Transfer Reaction-Mass Spectrometer for Measuring Volatile Organic Compounds in Ambient Air. *Environ. Sci. Technol.* **2002**, *36*, (7), 1554.
101. Keene, W. C.; Pszenny, A. A. P.; Maben, J. R.; Stevenson, E.; Wall, A., Closure evaluation of size-resolved aerosol pH in the New England coastal atmosphere during summer. *J. Geophys. Res.* **2004**, *109*, (D23), D23307.
102. Keene, W. C.; Pszenny, A. A. P.; Maben, J. R.; Sander, R., Variation of marine aerosol acidity with particle size. *Geophys. Res. Lett.* **2002**, *29*, (7), 1101.
103. Anderson, C. H.; Dibb, J. E.; Griffin, R. J.; Hagler, G. S. W.; Bergin, M. H., Atmospheric water-soluble organic carbon measurements at Summit, Greenland. *Atmos. Environ.* **2008**, *42*, (22), 5612.
104. Pszenny, A. A. P.; Moldanová, J.; Keene, W. C.; Sander, R.; Maben, J. R.; Martinez, M.; Crutzen, P. J.; Perner, D.; Prinn, R. G., Halogen cycling and aerosol pH in the Hawaiian marine boundary layer. *Atmos. Chem. Phys.* **2004**, *4*, (1), 147.
105. Mao, H.; Talbot, R.; Nielsen, C.; Sive, B., Controls on methanol and acetone in marine and continental atmospheres. *Geophys. Res. Lett.* **2006**, *33*, (2), L02803.
106. Liss, P.; Merlivat, L., Air-Sea Gas Exchange Rates: Introduction and Synthesis. In *The Role of Air-Sea Exchange in Geochemical Cycling*, Baut-Ménard, P., Ed. D. Riedel: Norwell, Mass., 1986; pp 113.
107. Wanninkhof, R., Relationship Between Wind Speed and Gas Exchange Over the Ocean. *J. Geophys. Res.* **1992**, *97*, (C5), 7373.
108. Asher, W.; Wanninkhof, R., Transient tracers and air-sea gas transfer. *J. Geophys. Res.* **1998**, *103*, (C8), 15939.
109. Zhou, Y.; Mao, H.; Russo, R. S.; Blake, D. R.; Wingenter, O. W.; Haase, K. B.; Ambrose, J.; Varner, R. K.; Talbot, R.; Sive, B. C., Bromoform and dibromomethane

measurements in the seacoast region of New Hampshire, 2002-2004. *J. Geophys. Res.* **2008**, 113, (D8), D08305.

110. White, A. B.; Darby, L. S.; Senff, C. J.; King, C. W.; Banta, R. M.; Koermer, J.; Wilczak, J. M.; Neiman, P. J.; Angevine, W. M.; Talbot, R., Comparing the impact of meteorological variability on surface ozone during the NEAQS (2002) and ICARTT (2004) field campaigns. *J. Geophys. Res.* **2007**, 112, (D10), D10S14.

111. Mao, H.; Talbot, R., O₃ and CO in New England: Temporal variations and relationships. *J. Geophys. Res.* **2004**, 109, (D21), D21304.

112. Mao, H.; Talbot, R., Role of meteorological processes in two New England ozone episodes during summer 2001. *J. Geophys. Res.* **2004**, 109, (D20), D20305.

113. Angevine, W. M.; Senff, C. J.; White, A. B.; Williams, E. J.; Koermer, J.; Miller, S. T. K.; Talbot, R.; Johnston, P. E.; McKeen, S. A.; Downs, T., Coastal Boundary Layer Influence on Pollutant Transport in New England. *J. Appl. Meteorol.* **2004**, 43, (10), 1425.

114. Fischer, E.; Pszenny, A.; Keene, W.; Maben, J.; Smith, A.; Stohl, A.; Talbot, R., Nitric acid phase partitioning and cycling in the New England coastal atmosphere. *J. Geophys. Res.* **2006**, 111, (D23), D23S09.

115. Darby, L. S.; McKeen, S. A.; Senff, C. J.; White, A. B.; Banta, R. M.; Post, M. J.; Brewer, W. A.; Marchbanks, R.; Alvarez, R. J., II; Peckham, S. E.; Mao, H.; Talbot, R., Ozone differences between near-coastal and offshore sites in New England: Role of meteorology. *J. Geophys. Res.* **2007**, 112, (D16), D16S91.

116. Chen, M.; Talbot, R.; Mao, H.; Sive, B.; Chen, J.; Griffin, R. J., Air mass classification in coastal New England and its relationship to meteorological conditions. *J. Geophys. Res.* **2007**, 112, (D10), D10S05.

117. Parrish, D. D.; Trainer, M.; Buhr, M. P.; Watkins, B. A.; Fehsenfeld, F. C., Carbon Monoxide Concentrations and their Relation to Concentrations of Total Reactive Oxidized Nitrogen at Two Rural U.S. Sites. *J. Geophys. Res.* **1991**, 96, (D5), 9309.

118. Kopacz, M.; Jacob, D. J.; Fisher, J. A.; Logan, J. A.; Zhang, L.; Megretskaia, I. A.; Yantosca, R. M.; Singh, K.; Henze, D. K.; Burrows, J. P.; Buchwitz, M.; Khlystova, I.; McMillan, W. W.; Gille, J. C.; Edwards, D. P.; Eldering, A.; Thouret, V.; Nedelec, P., Global estimates of CO sources with high resolution by adjoint inversion of multiple satellite datasets (MOPITT, AIRS, SCIAMACHY, TES). *Atmos. Chem. Phys.* **2010**, 10, (3), 855.

119. Grosjean, E.; Grosjean, D., The Reaction of Unsaturated Aliphatic Oxygenates with Ozone. *J. Atmos. Chem.* **1999**, 32, (2), 205.
120. Räisänen, T.; Ryyppö, A.; Kellomäki, S., Impact of timber felling on the ambient monoterpene concentration of a Scots pine (*Pinus sylvestris* L.) forest. *Atmos. Environ.* **2008**, 42, (28), 6759.
121. Niinemets, Ü., Mild versus severe stress and BVOCs: thresholds, priming and consequences. *Trends Plant Sci.* **2010**, 15, (3), 145.
122. Holopainen, J. K.; Gershenzon, J., Multiple stress factors and the emission of plant VOCs. *Trends Plant Sci.* **2010**, 15, (3), 176.
123. Kesselmeier, J.; Staudt, M., Biogenic Volatile Organic Compounds (VOC): An Overview on Emission, Physiology and Ecology. *J. Atmos. Chem.* **1999**, 33, (1), 23.
124. Martínez, E.; Cabañas, B.; Aranda, A.; Martín, P., Kinetics of the Reactions of NO₃ Radical with Selected Monoterpenes: A Temperature Dependence Study. *Environ. Sci. Technol.* **1998**, 32, (23), 3730.
125. Martínez, E.; Cabañas, B.; Aranda, A.; Martín, P.; Salgado, S., Absolute Rate Coefficients for the Gas-Phase Reactions of NO₃ Radical with a Series of Monoterpenes at T = 298 to 433 K. *J. Atmos. Chem.* **1999**, 33, (3), 265.
126. Cai, X.; Griffin, R. J., Secondary aerosol formation from the oxidation of biogenic hydrocarbons by chlorine atoms. *J. Geophys. Res.* **2006**, 111, (D14), D14206.
127. Griffin, R. J.; Cocker, D. R., III; Flagan, R. C.; Seinfeld, J. H., Organic aerosol formation from the oxidation of biogenic hydrocarbons. *J. Geophys. Res.* **1999**, 104, (D3), 3555.
128. Ng, N. L.; Chhabra, P. S.; Chan, A. W. H.; Surratt, J. D.; Kroll, J. H.; Kwan, A. J.; McCabe, D. C.; Wennberg, P. O.; Sorooshian, A.; Murphy, S. M.; Dalleska, N. F.; Flagan, R. C.; Seinfeld, J. H., Effect of NO_x level on secondary organic aerosol (SOA) formation from the photooxidation of terpenes. *Atmos. Chem. Phys.* **2007**, 7, (19), 5159.
129. Heald, C. L.; Henze, D. K.; Horowitz, L. W.; Feddema, J.; Lamarque, J. F.; Guenther, A.; Hess, P. G.; Vitt, F.; Seinfeld, J. H.; Goldstein, A. H.; Fung, I., Predicted change in global secondary organic aerosol concentrations in response to future climate, emissions, and land use change. *J. Geophys. Res.* **2008**, 113, (D5), D05211.

130. Kroll, J. H.; Seinfeld, J. H., Chemistry of secondary organic aerosol: Formation and evolution of low-volatility organics in the atmosphere. *Atmos. Environ.* **2008**, 42, (16), 3593.
131. Arneth, A.; Niinemets, Ü., Induced BVOCs: how to bug our models? *Trends Plant Sci.* **2010**, 15, (3), 118.
132. Karl, T.; Guenther, A.; Turnipseed, A.; Patton, E. G.; Jardine, K., Chemical sensing of plant stress at the ecosystem scale. *J. Geophys. Res. Biogeosci.* **2008**, 5, (5), 1287.
133. Schade, G. W.; Goldstein, A. H.; Lamanna, M. S., Are monoterpene emissions influenced by humidity? *Geophys. Res. Lett.* **1999**, 26, (14), 2187.
134. Bouvier-Brown, N. C.; Goldstein, A. H.; Gilman, J. B.; Kuster, W. C.; de Gouw, J. A., In-situ ambient quantification of monoterpenes, sesquiterpenes, and related oxygenated compounds during BEARPEX 2007: implications for gas- and particle-phase chemistry. *Atmos. Chem. Phys.* **2009**, 9, (15), 5505.
135. Holzinger, R.; Lee, A.; McKay, M.; Goldstein, A. H., Seasonal variability of monoterpene emission factors for a ponderosa pine plantation in California. *Atmos. Chem. Phys.* **2006**, 6, (5), 1267.
136. Schade, G. W.; Goldstein, A. H., Increase of monoterpene emissions from a pine plantation as a result of mechanical disturbances. *Geophys. Res. Lett.* **2003**, 30, (7), 1380.
137. Janson, R., Monoterpene concentrations in and above a forest of scots pine. *J. Atmos. Chem.* **1992**, 14, (1), 385.
138. Talbot, R.; Mao, H.; Sive, B., Diurnal characteristics of surface level O₃ and other important trace gases in New England. *J. Geophys. Res.* **2005**, 110, (D9), D09307.
139. Niinemets, Ü.; Reichstein, M., Controls on the emission of plant volatiles through stomata: Differential sensitivity of emission rates to stomatal closure explained. *J. Geophys. Res.* **2003**, 108, (D7), 4208.
140. Seinfeld, J. H.; Pandis, S. N., Atmospheric Composition, Global Cycles, and Lifetimes. In *Atmos. Chem. Phys.*, 1st ed.; John Wiley and Sons, Inc: New York, 1998; pp 49.
141. Seinfeld, J. H.; Pandis, S. N., Atmospheric Composition, Global Cycles, and Lifetimes. In *Atmos. Chem. Phys.*, 1st ed.; John Wiley and Sons, Inc: New York, 1998; pp 409.

142: Sakulyanontvittaya, T.; Duhl, T.; Wiedinmyer, C.; Helmig, D.; Matsunaga, S.; Potosnak, M.; Milford, J.; Guenther, A., Monoterpene and Sesquiterpene Emission Estimates for the United States. *Environ. Sci. Technol.* **2008**, 42, (5), 1623.